Review of nanophotonics approaches using nanostructures and nanofabrication for III-nitrides ultraviolet-photonic devices

Mohd Sharizal Alias
Malleswararao Tangi
Jorge A. Holguin-Lerma
Edgars Stegenburgs
Abdullah A. Alatawi
Islam Ashry
Ram Chandra Subedi
Davide Priante
Mohammad Khaled Shakfa
Tien Khee Ng
Boon S. Ooi

Review of nanophotonics approaches using nanostructures and nanofabrication for III-nitrides ultraviolet-photonic devices

Mohd Sharizal Alias,* **Malleswararao Tangi,**
Jorge A. Holguin-Lerma, Edgars Stegenburgs, Abdullah A. Alatawi,
Islam Ashry, Ram Chandra Subedi, Davide Priante,
Mohammad Khaled Shakfa, Tien Khee Ng, and Boon S. Ooi*
King Abdullah University of Science and Technology (KAUST), Photonics Laboratory,
Thuwal, Saudi Arabia

Abstract. Group III-nitride semiconductor materials especially AlGaN are key-emerging candidates for the advancement of ultraviolet (UV) photonic devices. Numerous nanophotonics approaches using nanostructures (e.g., nanowires, nanorods, and quantum dots/disks) and nanofabrication (e.g., substrate patterning, photonic crystals, nanogratings, and surface-plasmons) have been demonstrated to address the material growth challenges and to enhance the device efficiencies of photonic devices operating at UV wavelengths. Here, we review the progress of nanophotonics implementations using nanostructured interfaces and nanofabrication approaches for the group III-nitride semiconductors to realize efficient UV-based photonic devices. The existing challenges of nanophotonics applications are presented. This review aims to provide analysis of state-of-the-art nanophotonic approaches in advancing the UV-photonic devices based on group III-nitride semiconductors. © *The Authors. Published by SPIE under a Creative Commons Attribution 3.0 Unported License. Distribution or reproduction of this work in whole or in part requires full attribution of the original publication, including its DOI.* [DOI: 10.1117/1.JNP.12 .043508]

1 Introduction

The ultraviolet (UV) wavelength regime is typically divided into four wavelength ranges, i.e., UV-A (320 to 400 nm), UV-B (280 to 320 nm), UV-C (200 to 280 nm), and vacuum-UV (10 to 200 nm). Across these ranges, there are huge needs to realize UV-based photonic and electronic devices, e.g., laser diodes (LDs), light-emitting diodes (LEDs), photodetectors (PDs), high-electron-mobility transistors (HEMTs), metal-oxide-semiconductor field effect transistors, and radio-frequency switches. For instance, the market forecast for UV-LEDs is increasing from $90 million in the year 2014 to $800 million by the year 2020 due to the increasing demands in epoxy curing, water purification, food or medical sterilization, and new emerging applications.[1] The new applications include light sources, lithography, gas or chemical or bio-agent sensing, free-space nonline-of-sight communication, phototherapy, forgery detection, medical diagnostic, consumer electronics, and horticulture.[2]

To realize UV-based photonic and electronic devices, several wide energy bandgap materials have been utilized, e.g., group III-nitride semiconductors, diamond, SiC, β-Ga_2O_3, and ZnO.[3,4] The group III-nitride semiconductors have been considered the key UV-material because of their advantages, e.g., wide direct bandgap, material alloying capability for heterostructure and bandgap engineering, high electron mobility, high thermal stability, high breakdown field,

*Address all correspondence to: Mohd Sharizal Alias, E-mail: drsharizal@gmail.com; Boon S. Ooi, E-mail: boon.ooi@kaust.edu.sa
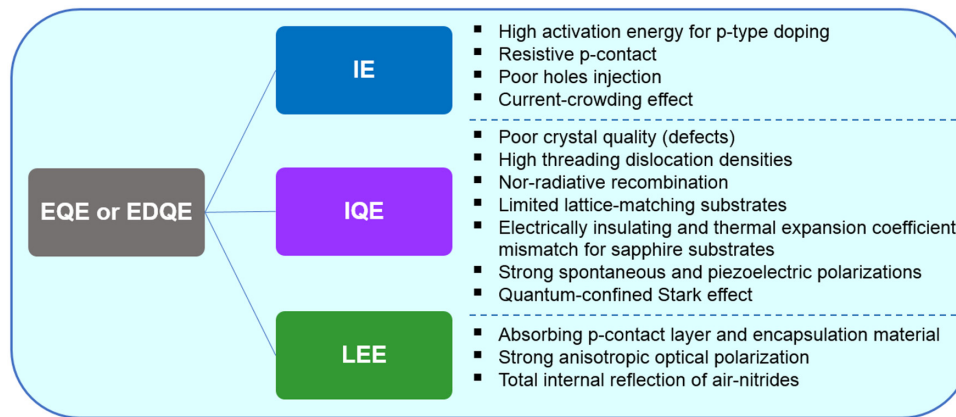
and high saturation velocity.[5] Furthermore, the material can sustain harsh temperature or radiation, and the material is toxic-free. Due to the alloying capability of the group III-nitride semiconductors, various material systems including AlGaN, InGaN, and InAlGaN have been used as the active region material for UV-based LEDs, LDs, PDs, and HEMTs.[6–9] Moreover, new boron-containing III-nitride semiconductors, e.g., BN and BAlN, have emerged recently for UV-photonic and electronic devices.[9–13] Nevertheless, AlGaN has been the mostly used material for UV-photonic devices because it has a large and tunable energy bandgap from 3.4 to 6.1 eV that can cover UV-A, B, and C spectral ranges. Furthermore, AlGaN has the nearest material compatibility with the InGaN material system. This is important to capitalize on the commercial-ready platform and technology maturity stage of InGaN-based photonic and electronic devices. However, to obtain an efficient photonic device (e.g., high external quantum efficiency, EQE), the AlGaN material system encounters several key challenges regarding material growth and device fabrication. Obtaining a high-quality (crack- and defects-free) AlGaN crystal growth is challenging as the crystalline quality degrades with increasing Al composition and the existence of economic lattice-matched substrate is limited.[3,6,7,14,15] Also, the realization of high doping efficiency for the p-doped AlGaN layer is challenging because of the required high activation energy (E_A) in such a layer (e.g., Mg-dopant case).[3,6,15,16] Moreover, in the case of AlGaN-based light emitters, the light-extraction efficiency (LEE) for AlGaN-based devices is low (<10%) due to the anisotropic optical polarization property for Al-rich AlGaN layers and due to the high absorption of the contact layers and encapsulation materials.[14,16] To address these key challenges especially for AlGaN-based photonic devices, numerous nanophotonics schemes related to the material growth and device stucture involving nanostructured interfaces [e.g., nanowires (NWs), nanorods (NRs), and quantum disks (QDisks)] and nanofabrication approaches [e.g., substrate patterning, surface roughening, photonic crystals (PhCs), and surface-plasmon (SP)] have been proposed.[2,14,15,17]

Here, we review the progress of nanophotonics implementations using nanostructured interfaces and nanofabrication approaches for the group III-nitride semiconductors (with the main focus on AlGaN material) to realize efficient UV-based photonic devices. We first discuss the AlGaN-related material and device challenges, and their effects on the device efficiency briefly. We then review the progress on using various nanophotonics schemes involving nanostructured interfaces and nanofabrication approaches adopted in the group III-nitride semiconductors for UV-based photonic devices. We will provide an overview of each approach and analysis of the device improvements (e.g., EQE and LEE). Finally, we provide an overall summary and point out the future directions of related research. This review aims to provide a framework of existing nanophotonic approaches and their further development in advancing the UV-photonic devices based on the group III-nitride semiconductors.

2 Nanophotonics Approaches for Enhancing Device Efficiencies

Focusing on light-emitting devices, e.g., LEDs and LDs, the device performance can be typically characterized by EQE for the LEDs case and by external differential quantum efficiency (EDQE) for the LDs case. The EQE is directly proportional to the internal quantum efficiency (IQE) and LEE. The IQE is a product of the injection efficiency (IE) and radiative recombination efficiency (RRE) of a material or a device.[7] As for the EDQE, it depends on IE, IQE, and mirror losses (which is indirectly associated with the LEE).[18] Thus, in both the LEDs and LDs cases, IE, IQE, and LEE play significant roles in enhancing the device performance. As stated earlier, several challenges limit the efficiency of the UV-photonic devices based on AlGaN material system, e.g., difficulty in crystal growth, p-doping, and LEE. Figure 1 shows the relationship of the above and several other challenges toward the IE, IQE, and LEE of LEDs and LDs.

Most of the challenges shown in Fig. 1 will be discussed further in the following section. Briefly here, the IE limitation is mainly due to the difficulty in obtaining high conductivity of doping (especially for p-type) to realize efficient $p - n$ junction devices, e.g., LEDs or LDs. For example, a high E_A (i.e., 310 meV for $Al_{0.27}Ga_{0.73}N$) is required to dope a Mg-dopants and will increase further for higher Al composition.[18] The low p-doping efficiency reduces the IE, which

| IE | High activation energy for p-type doping Resistive p-contact Poor holes injection Current-crowding effect |

| IQE | Poor crystal quality (defects) High threading dislocation densities Nor-radiative recombination Limited lattice-matching substrates Electrically insulating and thermal expansion coefficient mismatch for sapphire substrates Strong spontaneous and piezoelectric polarizations Quantum-confined Stark effect |

| LEE | Absorbing p-contact layer and encapsulation material Strong anisotropic optical polarization Total internal reflection of air-nitrides |

Fig. 1 A summary of most prominent challenges that limit the efficiency parameters for LEDs and LDs.

results in a high resistance *p*-contact and poor holes injection across the device. As for IQE, in general, increasing the Al composition to obtain shorter UV wavelengths in the AlGaN material causes a poor crystal quality due to increased density of defects in the form of cracks, dislocations, or impurities. Such defects can generate nonradiative center trap carriers and hence decrease the radiative recombination rate. This will reduce the IQE of the device. Due to the lack of native substrates, AlGaN has been grown on foreign substrates, e.g., sapphire, which is transparent to UV. However, to grow a high-quality AlGaN epitaxial structure on sapphire substrates is challenging due to large lattice mismatch and thermal expansion coefficient mismatch between the AlGaN/sapphire interface. Cracks easily formed with thicker AlGaN epilayer due to the accumulation of strong tensile strain. Compared with the InGaN epilayer on sapphire, AlGaN produced higher threading-dislocation densities (TDDs), i.e., $\sim 10^{10}$ to 10^{11} cm^{-2} due to the lattice mismatch, together with the large sticking coefficient and low surface mobility of Al adatoms during the crystal growth (in comparison, the TDDs for InGaN is $\sim 10^{8}$ cm^{-2}).[16,19] A recent approach of using bulk AlN substrates to grow AlGaN has been promising to reduce TDDs. However, the cost of AlN substrates is still expensive, and similar to sapphire, it is electrically insulating. To overcome this issue, *p*- and *n*-contacts of the AlGaN-based devices need to be fabricated on the same side of the wafer (lateral injection). This results in nonuniform current injection across the device (current crowding) and localized heating. Furthermore, in Al-rich AlGaN epilayer, O$_2$ can be easily incorporated into the lattice, hence increasing the impurities.[20] The spontaneous and piezoelectric polarizations are dominant in group III-nitride semiconductors, and these polarizations are even stronger with higher Al composition (strain from the tensile stress).[19] Both polarizations can reduce the RRE due to the quantum-confined Stark effect (QCSE), i.e., electron-hole recombination decreased from the band bending effect.[19] Also, the LEE of AlGaN light-emitters suffers from a strong anisotropic optical polarization, i.e., the transverse magnetic (TM) polarization becomes dominant with increasing Al composition. Moreover, the p-contact layer (mostly p-GaN is used because of high conductivity and easy to form ohmic contact) and encapsulation materials are absorbing at most of the UV spectral range.

To overcome the above-mentioned challenges to enhance IE, IQE, and LEE for AlGaN-based UV photonic devices, different approaches using nanophotonic schemes have been developed. Figure 2 listed the nanophotonic schemes that can be applied to enhance the efficiency of UV-photonic devices. We categorized these schemes into two main parts, i.e., nanostructured interfaces and nanofabrication approaches. Using a generic UV-LD device structure as an example (as shown in Fig. 3), we list some of the nanophotonic schemes that can be used to improve the device efficiency. For example, the use of nanostructured interfaces (e.g., NWs, NRs, and QDisks) and nanofabrication approaches (e.g., substrate patterning, PhCs, and naogratings) can enhance the IQE and LEE of the device. The detail of the nanophotonic schemes and related device performances will be reviewed next.
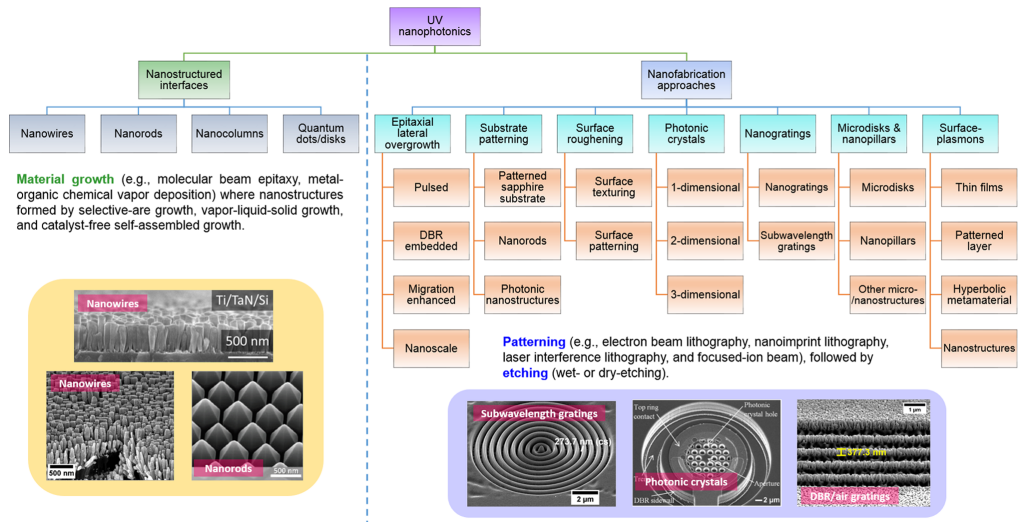
Fig. 2 Classification of nanophotonic schemes into nanostructured interfaces and nanofabrication approaches. The insets show microscopy images from several schemes of the nanophotonic.
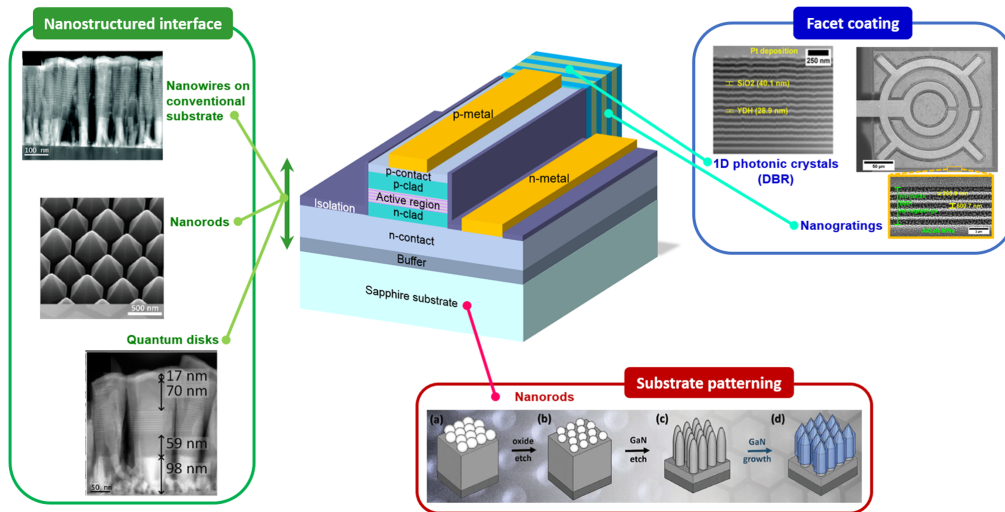
Fig. 3 Examples of nanophotonic schemes that can be applied on UV-LD to improve IQE and LEE.

3 Nanophotonics Schemes Using Nanostructured Interfaces

Several of the nanophotonic schemes, e.g., NWs, NRs, NCs, and monolayer are based on a bottom-up approach, i.e., material growth. Due to the high crystallinity requirement for the group III-nitride semiconductors including AlGaN, their epitaxial structures have been grown mostly using molecular beam epitaxy (MBE) and metal-organic chemical vapor deposition (MOCVD).

### 3.1 *Nanostructures: Nanowires, Nanorods, and Nanocolumns*

The NWs technology has recently pursued as NWs exhibit unique characteristics, e.g., high crystalline quality with low defect density and large surface-to-volume ratio. There are three significant ways to grow such high-quality NWs: the so-called lithography-based selective area growth (SAG), vapor liquid solid (VLS) growth, and the catalyst-free self-assisted growth schemes. Although the researchers have been succeeded to grow GaN NWs using VLS process, unavoidable contamination due to the metal usage in the growth process remained challenging.

To overcome such a problem, many efforts have been explored for NWs growth in the absence of metal particles.[21] In view of this, researchers have used selective-area metal–organic vapor phase epitaxy to grow ordered arrays of III-nitride NWs.[22] On the other hand, the SAG and VLS growth schemes are time-consuming, complicated, lack of control over doping densities, and limited crystalline quality.[23,24] An alternative growth scheme has been utilized to accomplish high-density self-assembled defect-free group-III nitride NWs at N-rich conditions.[25–30]

3.1.1 Selective area growth

Several efforts have been made to grow high-quality GaN NWs, NRs, and NCs on patterned substrates using MOCVD and hydride vapor phase epitaxy. MBE can also be utilized to achieve SAG under enhanced nucleation of III-nitride nanocrystals that were formed through the surface nitridation of an array of group-III metal nanodisks (NDs) on Si.[24] At low nucleation process of MBE, the III-metal sources readily adhere to an SAG mask of SiO_2, which results in a formation of a large number of self-assembled GaN NCs on counterparts of the patterned area.[31] For instance, Gotschke et al. have shown MBE growth of regular arrays of uniform-size GaN NWs on patterned Si/AlN/Si(111) substrates. The Si top layer has been patterned with e-beam lithography (EBL), resulting in uniform arrays of holes with different diameters and periods.[32] Choi et al.[33] reported the SAG of Ga-polar thin GaN NWs on patterned GaN/sapphire (0001) substrates using MOCVD with a continuous gas supply. GaN NRs formation on Ga-polar GaN by continuous mode MOCVD SAG was demonstrated under a relatively Ga-rich conditions. The growth rates of the semipolar planes, usually slowest growing planes, were controlled by varying the V/III ratio, which later allowed to grow GaN NRs along c-direction with nonpolar sidewalls.

First, the authors used a $GaN/c-Al_2O_3$ wafer that was patterned with a hexagonal array of circular holes using EBL and amorphous SiN_x formed by plasma-enhanced chemical vapor deposition (PECVD) as a masking material.[34] Later, GaN nanostructures were grown at a fixed temperature (1125°C) and TMG flow rate (24 sccm), whereas the NH_3 flow rate was varied from 150 to 5 sccm. Figures 4(a)–4(d) show scanning electron microscope (SEM) images for the evolution of the GaN nanostructure morphology as a function of NH_3 flow rate of 150, 25, 10, and 5 sccm, respectively. This revealed that the nanopyramids (NPs) structure
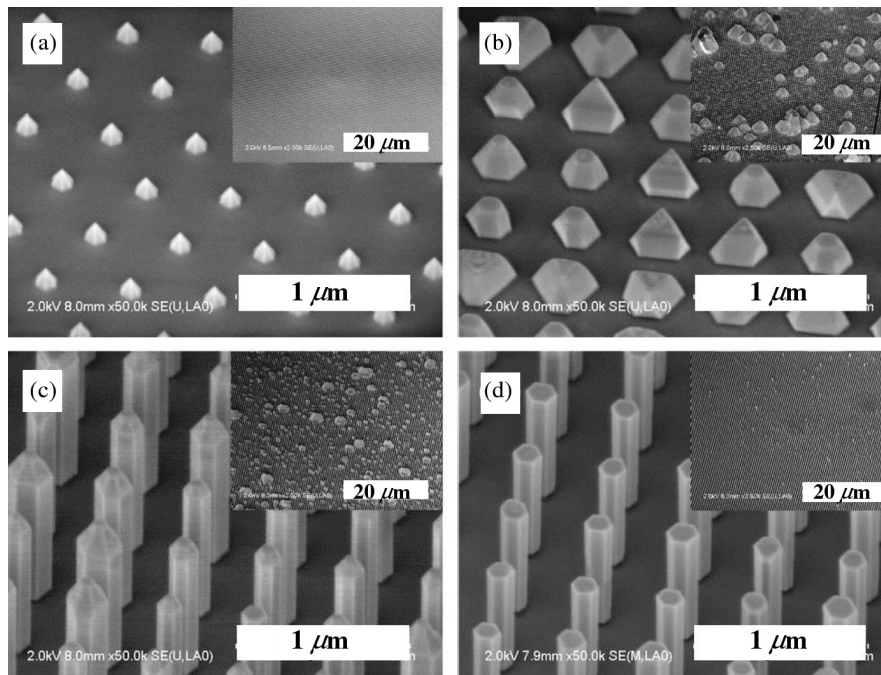
Fig. 4 GaN nanostructures evolution with respect to NH_3 flow rate show in (a) 150, (b) 25, (c) 10, and (d) 5 sccm. The insets show lower magnification SEM images. Reproduced with permission from Ref. 35.
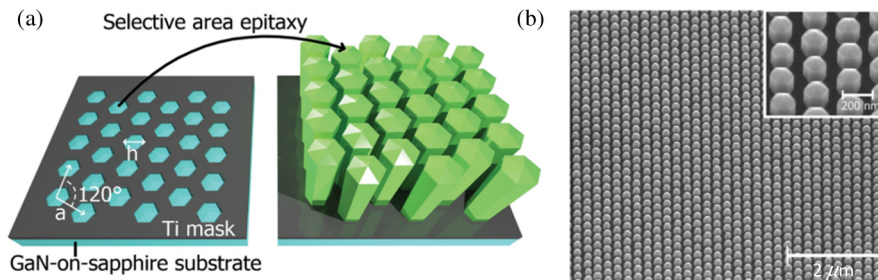
Fig. 5 (a) Left: arrays of nanoscale opening apertures defined by EBL process on a Ti mask on planar GaN template on the c-plane sapphire substrate. Right: schematic of the SAG of GaN NWs arrays on the nanopatterned substrate. (b) A tilted view SEM image showing GaN NWs arrays selectively grown in the opening apertures. The inset shows a high-magnification SEM image of GaN NWs arrays. Reproduced with permission from Ref. 36.

defined by {1–101} semipolar planes need to be formed under the higher pressure of NH_3. As the size of the NPs is observed to be comparable with the original opening diameter, the growth rate of semipolar m-plane {1–101} is extremely low, which determines the formation of nanostructures as NPs.

The SAG of GaN NWs was further utilized as a template to grow AlGaN NWs-based photonic devices. For example, Le et al.[36] have used arrays of nanoscale opening apertures defined by EBL process on a Ti mask on planar GaN template on the c-plane sapphire substrate to grow GaN NWs. Later, this approach has been used as a template to grow defect-free coalesced AlGaN NWs-based UV-LED device structures.

Figure 5(a) shows the schematic representation of selective area epitaxy of GaN/AlGaN NWs arrays on a GaN template/c-sapphire substrate by employing a thin (≈10 nm) Ti layer as the growth mask. Hexagonal openings situated as a triangular lattice were created on the Ti mask having a lattice spacing, a and a lateral size, h for each opening. These nanohole arrays were then created on the Ti mask using EBL and reactive ion etching. Later, GaN NWs arrays were selectively grown in the opening apertures by MBE. Figure 5(b) shows the SEM image of GaN NWs, exhibiting a high degree of size uniformity and are vertically aligned along the c-axis with well-defined hexagonal pyramid morphology comprised of six semipolar top facets.

3.1.2 Vapor–liquid–solid growth

The growth of III–V nanostructures has also been achieved using catalyst-assisted routes, e.g., catalytic metal-induced VLS mechanism, where metal droplets enable the material to solidify below the frozen liquid–solid interface.[37,38] The nanostructures can be then formed via the vapor−liquid−solid mechanism with, e.g., Au, Fe, or Ni as growth initiators.[39] Recently, Sivadasan et al.[40] reported on the optical properties of AlGaN NWs grown using the CVD method. They investigated the influence of the distribution of Au catalyst nanoparticles on the size and shape of AlGaN NWs. However, due to the deleterious effects of metal impurities on the structural, optical, and electrical properties of the semiconducting nanostructures grown using the VLS process,[23] researchers seldom used this method for the AlGaN NWs growth.

3.1.3 Catalyst-free self-assembled nanowires on conventional substrates

Another method to grow NWs is self-assembled growth, which does not require any catalyst and prepatterned substrates. Several researcher works have been reported on the growth of such spontaneously formed NWs on Si substrates using the MBE and MOCVD.[28,30,41] As compared with the ELOG, VLS, and SAG growth schemes, employing MBE or MOCVD for NWs growth is less time consuming and more scalable. Under certain conditions, e.g., N-rich and low metal conditions (V/III ratio ≫ 1) the growth of self-assisted dislocation free NWs on sapphire and Si substrates can be realized.

In this context, Janjua et al.[42] reported AlGaN NWs LEDs using the pendeo-epitaxy technique. Highly dense and spontaneously coalesced NWs emitting at 303-nm wavelength were
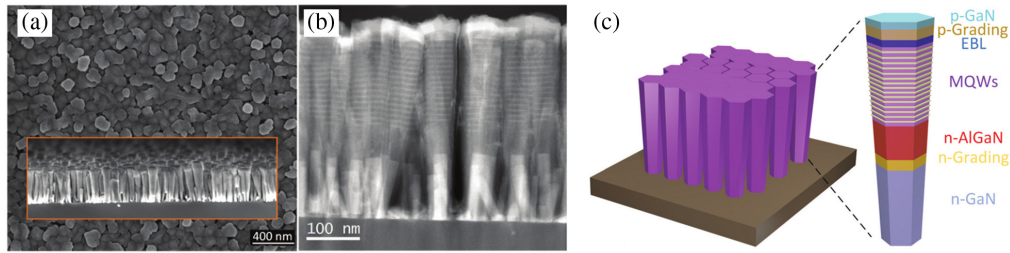
Fig. 6 (a) Top-view SEM image of the AlGaN NWs-based device structure. The inset shows cross-sectional SEM of these NWs. (b) STEM image of the coalesced AlGaN NWs. (c) A schematic of the device. Reproduced with permission from Ref. 42.

grown on Si substrates. Figure 6(a) shows a top-view SEM image of the AlGaN NWs, whereas the inset shows a cross-sectional SEM of these NWs. The coalescence of the top p-GaN (in the inset) improves the current spreading and injection and reduces carrier leakage without the needs for planarization. Figure 6(b) shows a cross-sectional scanning tunneling electron microscope (STEM) image of an array of AlGaN NWs with device schematic shown in Fig. 6(c). To further optimize the AlGaN NWs LEDs, the self-assembled NWs were grown with varying QDisks thickness to study the carrier separation in the active-region and implemented a graded p-contact-layer to increase the output power.[43] They observed an improvement by 100 times in the direct recombination rate for samples with thicker QDisks thickness of ~5 monolayers (MLs) compared with the sample with ~2 MLs-thick QDisks. Moreover, the sample with graded top Mg-doped AlGaN layer shows 10 times improvement in the output power.

In addition to LEDs, NWs-based LD has been recently demonstrated. Li et al.[44] reported a highly stable and electrically pumped lasing emission in the UV-A at low temperature using the defect-free disordered AlGaN core–shell NWs arrays grown on Si substrate. Figure 7(a) shows
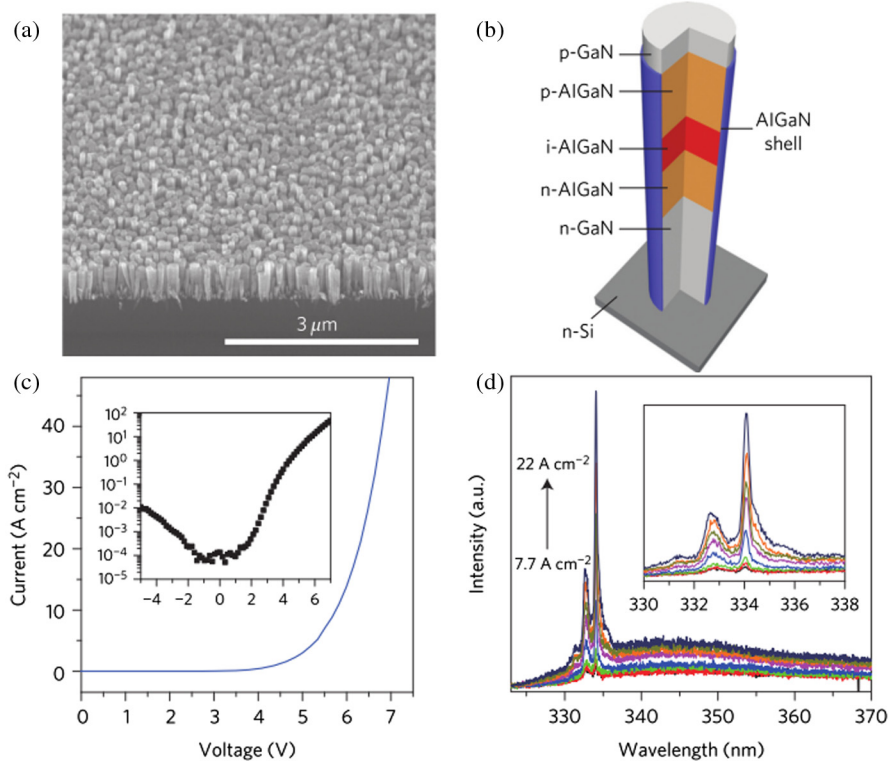
Fig. 7 (a) SEM image of NWs grown on a Si substrate, (b) schematic of the device, (c) I–V characteristics of the device; the inset shows the I–V curve on a semilog scale, and (d) emission spectra measured at 6 K under different current densities with the inset shows zoom-in of the lasing spectra. Reproduced with permission from Ref. 44.
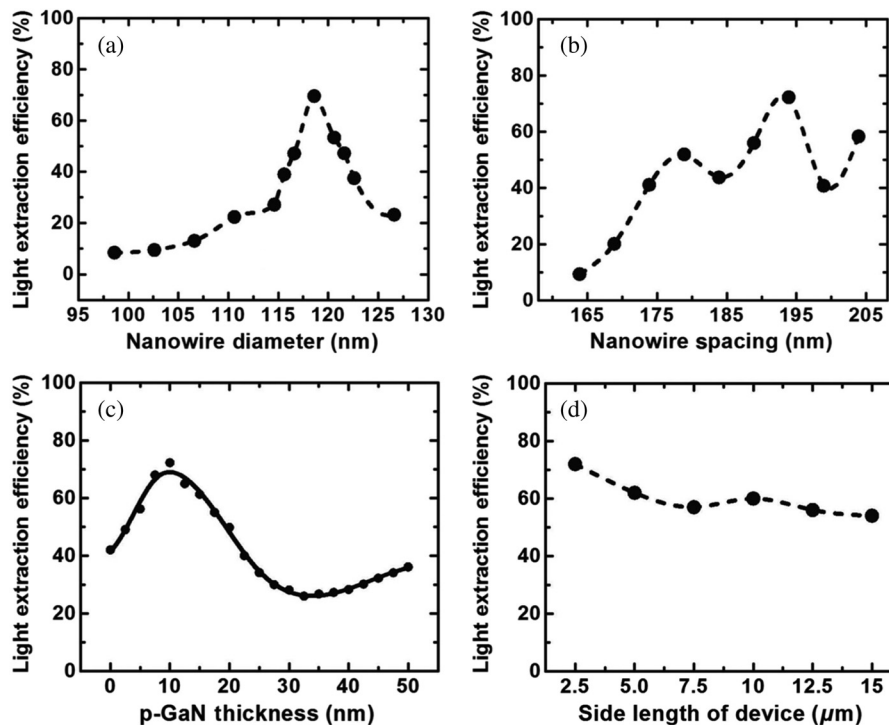
Fig. 8 (a) LEE versus diameter of NWs, (b) LEE versus spacing of NWs, (c) LEE versus thickness of the p-GaN layer, and (d) simulated LEE for devices with side length variations. Reproduced with permission from Ref. 45.

the SEM image of NWs grown on a Si substrate with the device schematic shown in Fig. 7(b). Figure 7(c) shows the I–V curve with the inset indicating a low leakage current under reverse bias. The lasing characteristics of AlGaN NWs were investigated by electrical injection under a continuous-wave operation at various temperatures. Figure 7(d) shows the EL spectra measured at 6 K. Two discrete peaks centered at 332.7 and 334.1 nm were observed. The spectral linewidth is as narrow as 0.2 nm above the lasing threshold of ∼12 A cm^{-2}.

Using NWs, an enhancement in the LEE for a UV-LED can be achieved. Djavid and Mi[45] studied the lateral side emission properties of NWs UV-LEDs using a simulation approach. Enhanced LEE of ∼72% was accomplished by optimizing the NWs size and density, as well as optimizing the thickness of the p-GaN layer. Figure 8(a) shows the dependence of LEE on the diameter of NWs. Hence, it is evident that there is an optimum diameter at which the light could be efficiently coupled through the NWs for efficient lateral side emission. Figure 8(b) shows the LEE that was further calculated as a function of the spacing between NWs from 163 to 203 nm. The corresponding LEE varied from 9% to 72%. TM polarized light can propagate horizontally through the NWs arrays resulting in significantly enhanced LEE. Figure 8(c) shows the LEE having an overall decreasing trend with increasing p-GaN thickness. Also, the authors have performed a simulation with device sizes in the ranges of 2.5 × 2.5 to 15 × 15 μm^2. As shown in Fig. 8(d), the LEE decreases from 72% to 54% as device size increases. In addition to the diameter and spacing of NWs, the tapering angle of the grown AlGaN NWs can also enhance the LEE for a UV-LED.[46]

3.2 Quantum Disks and Quantum Dots

Here, we discuss the research progress on the use of quantum dots (QDs) and QDisks for UV photonics. First, we focus more on the material properties and then we will discuss the advancement of the device based on QDs and QDisks.

In addition to the ability to tune the energy bandgap of the group III-nitride semiconductors by material composition variation, this tuning can also be achieved through quantum
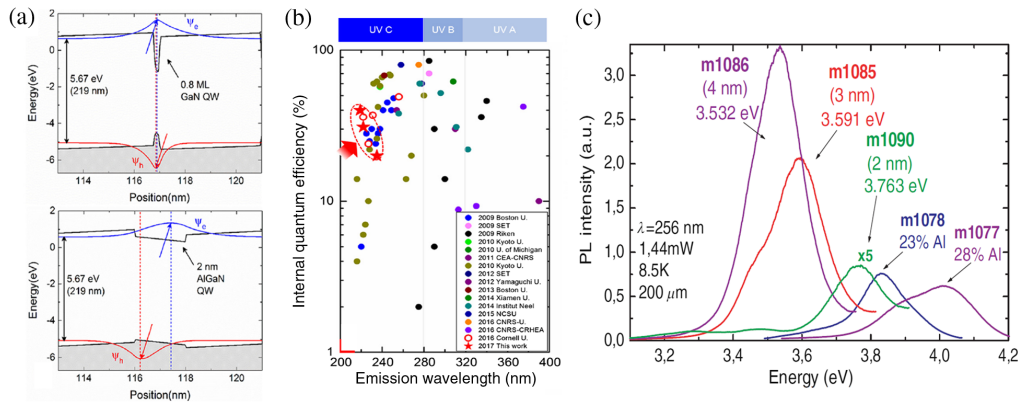
Fig. 9 (a) Enhancement of IQE using GaN QWs due to the reduced QCSE. Reproduced with permission from Ref. 47. (b) Comparison of measured IQE of GaN- and AlGaN-based heterostructures. Reproduced with permission from Ref. 47. (c) PL spectra of GaN QDisks with thickness variation. Reproduced with permission from Ref. 48.

confinement using a thin active layer in the form of QDs and QDisks structures. Islam et al.[47] have shown that by changing the thickness of GaN QDisks, a PL emission as short as 219-nm wavelength can be obtained as shown in Fig. 9(a). Recent works reveal that a higher IQE can be achieved in the GaN-based QDs[49,50] and QDisks[47,48,51,52] compared with the AlGaN-based quantum wells structure in the similar wavelength range. Figure 9(b) shows a comparison between GaN and AlGaN heterostructures in terms of IQE.[47]

Tanaka et al.[53] grew GaN QDs on AlGaN-layered surfaces with MOCVD and observed a strong PL peak at ∼3.55 eV. In the same year, Seifert et al.[54] demonstrated the growth of III–V and III–nitrides-based QDs by means of the Stranski–Krastanov method using the MOCVD platform. This is followed by the successful growth of GaN QDs using the MBE platform.[55] Next, Ristić et al.[56] reported defect-free and fully relaxed AlGaN NCs on Si (111) substrate grown by MBE. In contrast, GaN QDisks (also grown for a comparison study) are fully strained as indicated by the Raman measurement.[56] A comprehensive study on optical, electrical, and morphological properties of GaN QDisks was later followed by Ristić et al.[48,57] It was found that PL emission red-shifted (due to the QCSE) when the Al composition in the GaN/AlGaN QDisks is increased from 20% to 28%. However, blue-shift in PL emission was observed [as shown in Fig. 9(c)] when the thickness of QDisks is decreased from 4 to 2 nm (using the set of NCs with 28% of Al composition with different QDisks thickness).[48,57]

Recently, several UV-photonic devices were demonstrated based on the GaN QDs and QDisks.[42,49,50,51,58–63] One of the challenges to achieving efficient UV emitting devices is to overcome the poor current injection. In this context, Verma et al.[49,50] demonstrated UV-LED based on
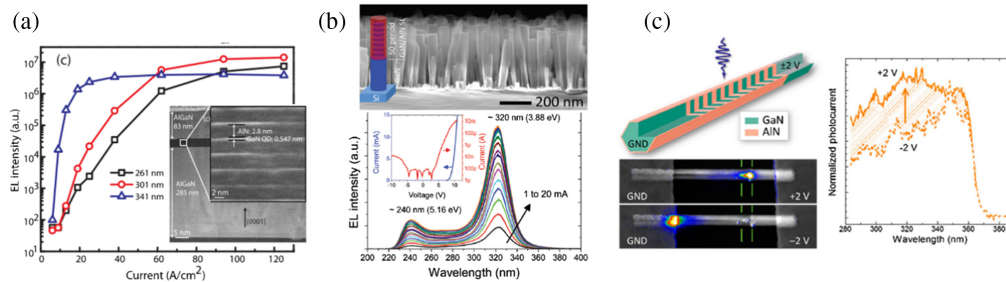
Fig. 10 (a) EL characteristic and cross-sectional STEM (inset) for GaN QDs UV-LED. Reproduced with permission from Ref. 49. (b) Cross-sectional SEM and EL characteristic (I–V curve inset) for GaN QDisks UV-LED. Reproduced with permission from Ref. 51. (c) A schematic of the GaN QDisks-based UV-PD, heat maps (under biased) overlaid with the SEM images and spectral response under several voltage biases. Reproduced with permission from Ref. 63.

Table 1 A summary of research for material and devices based on GaN QDs and QDisks.

Device	Active region	Peak emission wavelength (nm)	Remarks	Ref.
PL structure	GaN QDisks	219	IQE $\sim 40\%$	47
	GaN QDisks	222 to 231	IQE $\sim 35\%$	52
	GaN QDs	295 to 326	—	64
	GaN QDisks	358 to 306	—	48 and 57
	GaN QDs	350	—	53
LED	GaN QDisks	242	EQE $\sim 0.012\%$	65
	GaN QDisks	240	—	51
	AlGaN QDisks	325	—	62
	AlGaN QDisks	337	—	42
PD	GaN QDisks	280 to 360	—	63
	GaN QDisks	300	Response $\sim 2 \times 10^3$ A/W	61

GaN QDs as an active layer and utilized tunnel junction (TJ) scheme. Figure 10(a) shows the cross-sectional STEM of the device with the EL characteristic. In Fig. 10(b), Sarwar et al.[51] demonstrated GaN-based LED utilizing QDisks at $\sim$1-ML-thick embedded in AlN NW on a Si substrate with EL emission at sub-250-nm wavelength. In addition to UV-LEDs, several PDs based on GaN QDisks have been reported recently.[61,63] For example, Spies et al.[63] presented a study in GaN/AlN QDisks embedded in a single GaN NW as shown in Fig. 10(c). With such a structure, they claimed to enhance the response under positive/negative bias in the UV-A and UV-B regimes [Fig. 10(c)].

To summarize, the ongoing research on GaN-based QDs and QDisks is paving a promising path to develop highly efficient UV-photonic devices. Table 1 summarizes the findings of research performed so far for both the material optimization and devices development.

4 Nanophotonics Schemes Using Nanofabrication Approaches

Various nanophotonic approaches to enhance the material properties (IQE) and device performance (e.g., IE, LEE, and EQE) of UV-photonic devices are discussed in this section. The nanophotonic approaches can be realized using advanced nanofabrication techniques including (1) lithographic patterning, e.g., EBL, nanoimprint lithography (NIL), and laser interference lithography (LIL), followed by wet- or dry-etching, or (2) direct patterning/etching using focused-ion-beam (FIB).

4.1 Epitaxial Lateral Overgrowth

Most common obstacles in the growth of group-III nitride semiconductors are the lattice/thermal mismatch between the grown epilayers and foreign substrates (due to the lack of native substrates that results in high TDDs (10^7 to 10^9 cm^{-2}). Thus, a key factor to improve the performance of UV-devices is to reduce the TDDs and to solve the cracking issue of AlN and AlGaN films that typically originate from tensile strain beyond the critical layer thickness. Considering the cost and large area limitations of the native substrates (e.g., AlN or GaN), the devices that are grown on the native substrates are difficult to be commercialized. Therefore, to enhance the material quality of epilayers grown on nonnative substrates, different approaches, e.g., epitaxial lateral overgrowth (ELOG), pulsed-ELOG (PLOG), migration-enhanced ELOG (MEELOG), patterned dielectric distributed Bragg reflector (DBR) embedded ELOG, and nanoscale-ELOG schemes,

have been suggested and successfully employed. In the ELOG growth scheme, a masked substrate is used in such a way that the material selectively grows on the unmasked region and thereby lateral coalescence takes place at the growth fronts.

For instance, Balakrishnan et al.[66] have demonstrated an air bridge-assisted high-temperature ELOG approach to deposit 12-μm-thick, high-quality AlN layers over a patterned 6H-SiC substrate as templates for the UV-LED. The overall dislocation density of the layer was estimated to be in the range of 10^6 cm^{-2} or less with major portions of the layer formed over the voids are dislocation free. Chen et al.[67] reported on pulsed-ELOG (PLOG) of AlN films on basal plane sapphire substrates. This approach, at temperatures higher than 1150°C, enhanced the adatom migration, thereby significantly increasing the lateral growth rates. This enabled a full coalescence in wing regions as wide as 4 to 10 μm resulting in a reduction of the TDDs from 10^{10} to 10^7 cm^{-2}. Moreover, Adivarahan et al.[68] reported the growth of LED structures with AlGaN multiple quantum well (MQW) on a 17-μm-thick, high-quality PLOG AlN layers/sapphire [Figs. 11(a) and 11(b)] and obtained UV emission at 290 nm [Fig. 11(c)].

Figure 11(d) shows comparison between the output power of standard and PLOG grew UV-LEDs; the output powers of PLOG AlN-based LED devices do not saturate for DC pump currents, whereas the standard LED output powers start to saturate. The superior performance of the reported UV-LEDs was ascribed to the reduced thermal impedance and the decrease of overall defect density in the laterally overgrown AlN. Additionally, Jain et al.[69] reported the coalescence of growth fronts using a technique in which the migration-enhanced MOCVD was successfully combined with the ELOG method to grow AlN with less defect density.

Cheng et al.[70] have demonstrated an enhancement of the output power of UV-LED by realizing ELOG on a patterned DBR substrate. The UV-LED samples were grown on c-plane sapphire substrates by a low-pressure MOCVD system. Figure 12(a) shows the schematic diagram of the fabricated UV-LED with embedded HfO$_2$/SiO$_2$ DBR. Figures 12(b) and 12(c) show the
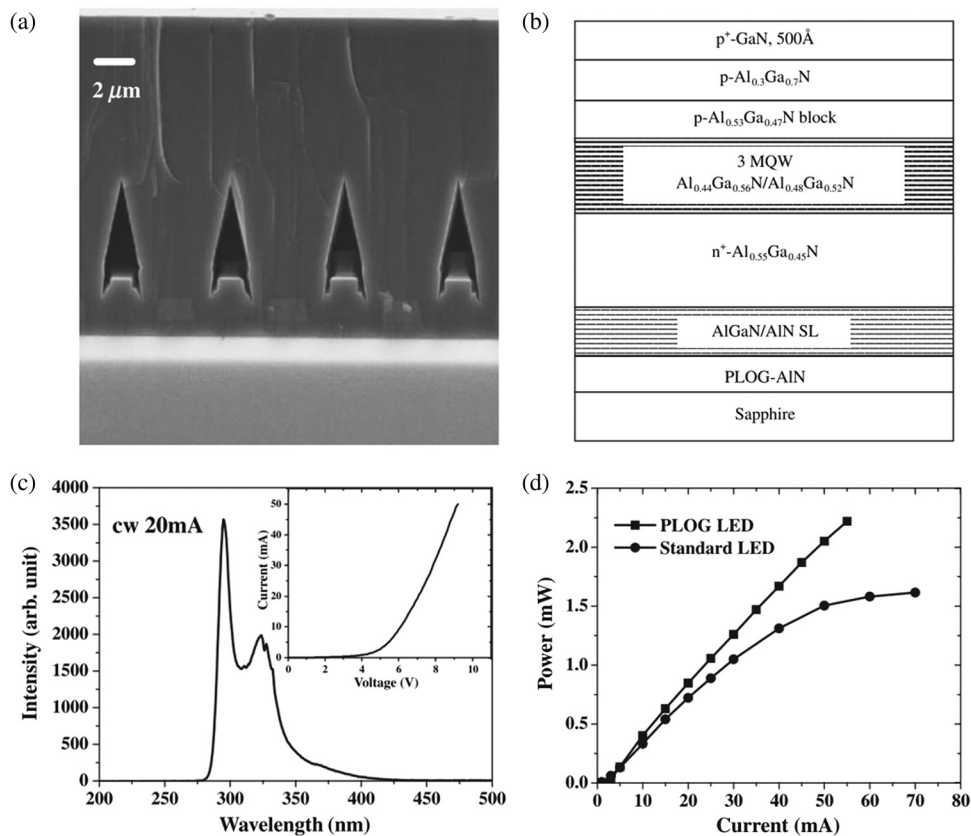
Fig. 11 (a) Cross-sectional SEM of PLOG of AlN, (b) schematic diagram of the UV-LED structure, (c) EL spectrum of the device with I–V curve (in the inset), and (d) a comparison between standard and PLOG grew LEDs. Reproduced with permission from Ref. 68.
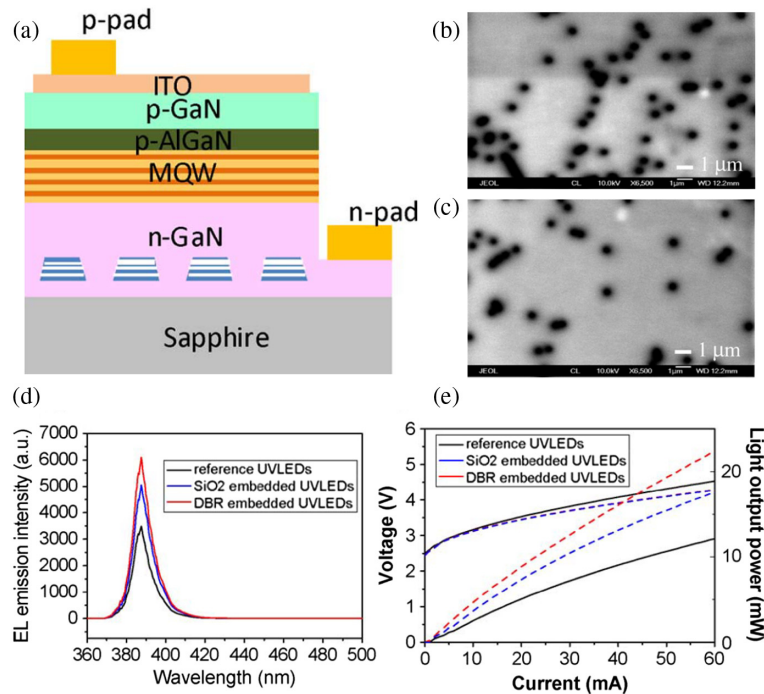
Fig. 12 (a) Schematic of ELOG using patterned DBR, (b) CL image of the reference sample, (c) CL image of the surface of DBR embedded UV-LED after MOCVD growth, (d) EL spectrum, and (e) L–I–V characteristics of all samples. Reproduced with permission from Ref. 70.

cathodoluminescent (CL) images acquired for a reference sample (without DBR) and with DBR, respectively. The dark spots denote strong nonradiative recombination centers showing low CL intensity result from the TDDs terminated at the surface. The defect density of DBR embedded UV-LED is 36% lower compared with the reference UV-LED. Figure 12(d) shows the EL spectrum, whereas Fig. 12(e) shows the light–current–voltage (L–I–V) characteristic for all samples. The optical power of SiO$_2$- and DBR-embedded UV-LEDs have significant 45% and 75% improvement as compared with the reference device. This enhancement was attributed to the improvement in the material quality from ELOG and in the light output coupling from the embedded DBR. Similarly, Huang et al.[71] reported the InGaN/GaN MQW UV-LED with embedded Ta$_2$O$_5$/SiO$_2$ micromirror array (MMA) in the ELOG of GaN for the LEE enhancement. They achieved a 75.2% LEE enhancement for the patterned SiO$_2$ LED, and a 102.6% LEE enhancement for the MMA-LED, both were compared with the control sample.

The nanoscale ELOG scheme shows a more TDDs reduction in the overgrown group III-nitride semiconductors as compared with the microscale ELOG.[72–74] For example, Conroy et al.[73] reported an inexpensive nanoscale patterning process for ELOG on AlN layers grown by MOCVD. The uniform 1-μm-length NRs structure, formed by dry-etching of mono-layer silica spheres, was used as a template for nanoscale ELOG epitaxy. A schematic drawing and an SEM image of the structure are shown in Figs. 13(a) and 13(b), respectively. A massive reduction in TDDs in the overgrown AlN layer is observed when the sample was annealed at 1100°C. This is formed at a much lower temperature compared with that typically required for microscale ELOG.[75] Figure 13(c) shows the FIB section of AlN overgrowth at 1100°C tilted to $g = (0002)$ showing a-type dislocations. Figures 12(e) and 12(f) show the dislocations at higher magnifications, whereas Fig. 13(d) shows the FIB cross sections of typical high-quality three step AlN templates in the $g = (0002)$ without ELOG. Without NRs patterning, the observed density of the edge and mixed dislocations was found to be ~4.4 × 10^9 cm^{-2}. In comparison, AlN films produced using the NRs ELOG process had TDDs of <10^8 cm^{-2}.

Recently, Lee et al.[74] have demonstrated AlGaN-based UV-LED with periodic air-voids-incorporated nanoscale patterns enabled by nanosphere lithography and ELOG on a sapphire substrate. Figure 14(a) shows their fabrication process of AlN/sapphire nanopatterned substrate
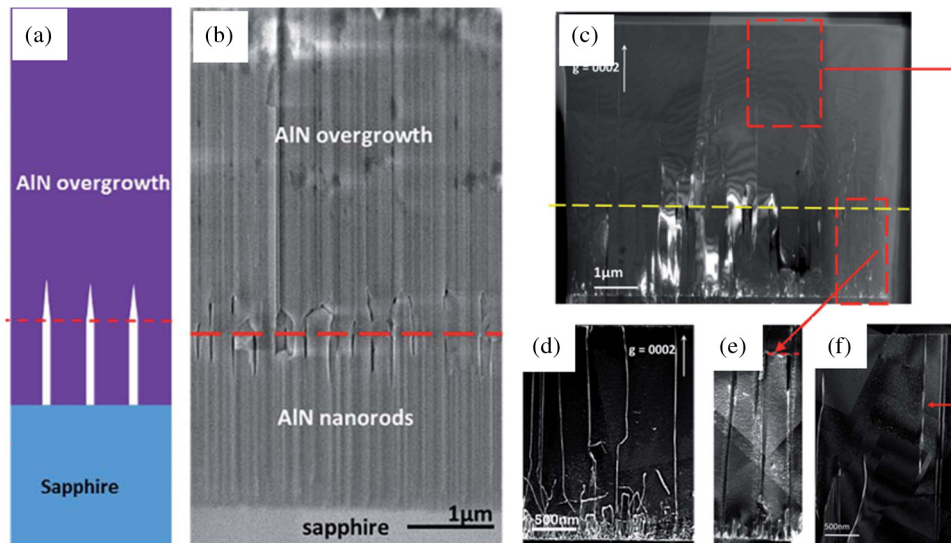
Fig. 13 (a) Schematic of the nanoscale-ELOG of AlN overgrowth on the NRs, (b) cross-sectional SEM image of the interface of AlN NRs and the overgrown layer with air gaps, (c) FIB section of AlN overgrowth at 1100 deg showing a-type dislocations, (d) cross-sectional FIB, (e) and (f) dislocations showed at higher magnifications. Reproduced with permission from Ref. 73.

(NPS). After initial growth, the self-assembled Si nanospheres as etch masks were coated on the AlN layer/c-sapphire. Then, dry-etch was accomplished to transfer the nanospheres pattern to the underlying AlN layer. Figures 14(b) and 14(c) are plan-view, and tilted view SEM images of the fabricated NPS, whereas the cross-section is shown in Fig. 14(d). Figure 13(e) shows the I–V characteristics for all devices. Figure 14(f) shows the average light output power (LOP) as a
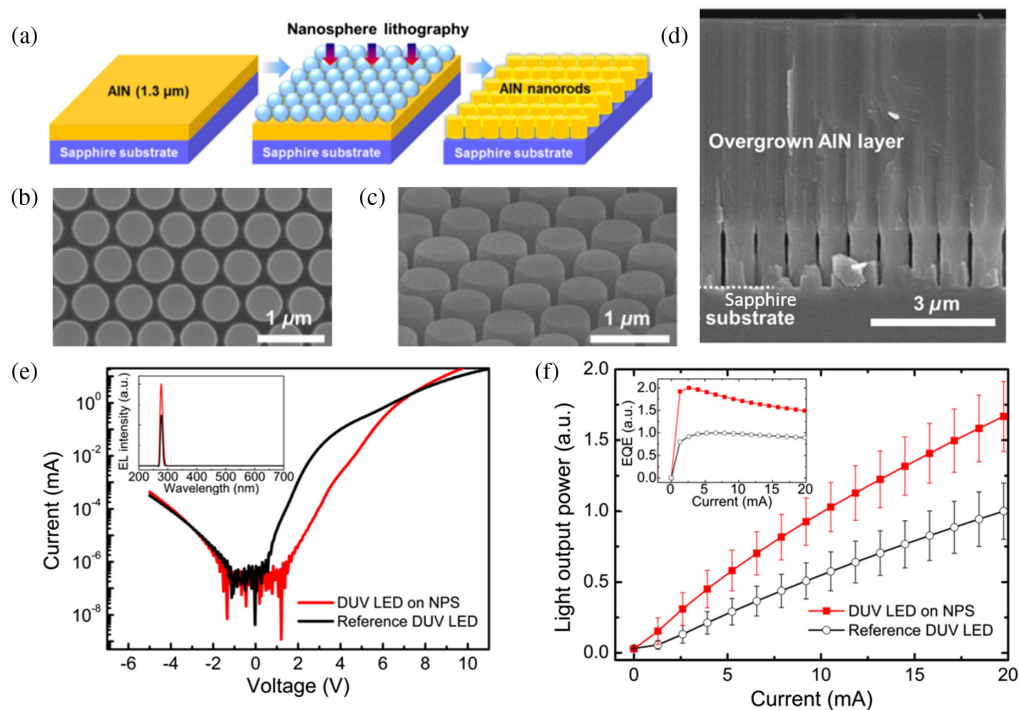
Fig. 14 (a) Schematic of silica nanosphere lithography, (b) top- and (c) tilted-view SEM images of the fabricated NPS. (d) Cross-section SEM image of the overgrown AlN layer on the NPS. (e) I–V characteristics of all devices. The inset shows EL spectra. (f) Average LOP with error bars as a function of injection current. The inset shows relative EQE. Reproduced with permission from Ref. 74.

Table 2 A summary of research using ELOG scheme to improve the UV device performance.

Substrate	ELOG type	TDD without ELOG (cm^{-2})	TDD with ELOG (cm^{-2})	Enhancement	Ref.
Sapphire	Pulsed	10^{10}	10^{7}	PL intensity (10 times)	67
Sapphire	Pulsed	—	10^{7}	(40%) relative power	68
6H-SiC	HT	—	10^{6}	—	66
Sapphire	DBR embedded	2.5×10^{6}	1.6×10^{6}	75% (EL intensity)	70
Sapphire	Hetero facet controlled	—	3.9×10^{8}	8.2% (EDQE)	76
Sapphire	Nanoscale	1.5×10^{9}	3×10^{8}	14.5% (Reflectance)	73
Sapphire	Nanoscale	6.0×10^{9}	4.4×10^{9}	67% (LOP)	74
Sapphire	—	—	6×10^{7}	PL narrowed (1.6 meV)	77
Sapphire	Migration enhanced	3.5×10^{9}	2.6×10^{8}	Device life time (5000 h)	69

function of the injection current measured from 50 LEDs at room temperature. The LOP of the UV-LEDs/NPS exhibited higher LOP by 67% than that of the reference device.

To summarize the ongoing research activities on the ELOG growth scheme, it is an outstanding approach to achieve efficient UV-photonic devices by means of reducing the defects at the growth fronts. These growth fronts were later utilized as templates for the overgrowth of the device structures. Table 2 consolidates the reduction of TDDs in the device structures using the ELOG scheme. Recently, research efforts have been demonstrated to address the problem of large lattice and thermal expansion mismatch by growing GaN on layered transition metal dichalcogenides (TMDs), e.g., MoS^{2} and WeS^{2}, with the sapphire substrates beneath.[78–81] The similar route can be used in growing AlGaN for the UV wavelengths in addition to the ELOG scheme.

4.2 Substrate Patterning

Various substrate patterning approaches have been suggested to enhance the performance of III-nitrides-based devices grown on sapphire substrates. Among them, the patterned sapphire substrate (PSS), i.e., sapphire substrate surface patterning with nanometer-to-micrometer-sized artificial structures, has been proven to be very promising to enhance the device's performance regarding the IQE and LEE. While the IQE is improved due to the reduction of TDDs by selective-area growth, the LEE is improved due to the photon scattering at the uneven sapphire surface.

A typical patterning process of the sapphire substrate surface involves several steps, as shown in the upper part of Fig. 15. After substrate cleaning, the surface is coated with a resist layer. Then, the desired spatial resolution and shape of the pattern are determined by a designed mask using a relevant lithography method. The patterning process ends with the resist development. During this step, the resist is selectively removed. The second part of the PSS fabrication is to transfer the resist structure, i.e., pattern, to the sapphire substrate. Here, two different ways can be applied as shown in the lower part of Fig. 14; either by an additive technique by depositing a thin film on the substrate surface or using a subtractive technique by etching the substrate surface. Ultimately, the PSS process ends with the resist removal. In the literature, different shapes of PSS have been suggested and fabricated. Figure 16 shows SEM images for some examples of PSS.

Here, we review the use of PSS to enhance the performance of the UV-photonic devices by taking into account the approach used to fabricate the PSS (additive or subtractive techniques). The utilization of PSS for Flip-Chip UV-LED is also discussed. Thereafter, the advantage of using substrate sidewall roughening for UV-LEDs is presented. Ultimately, a few examples of patterning non-sapphire substrates, i.e., Si substrates for UV applications, are discussed.
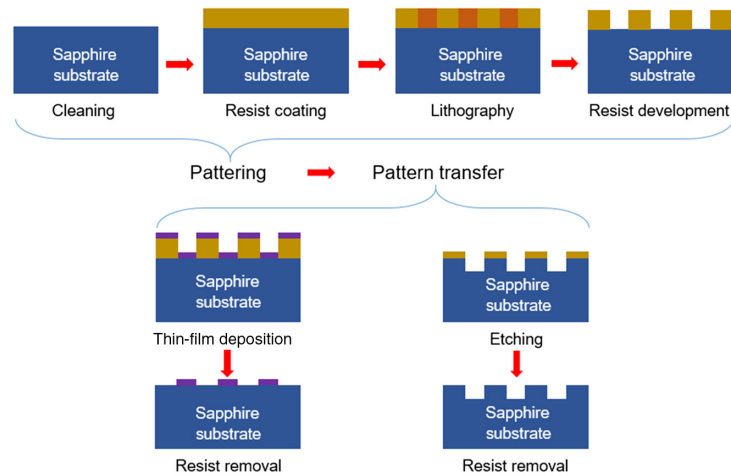
Fig. 15 Typical patterning and pattern transfer process to fabricate a PSS.
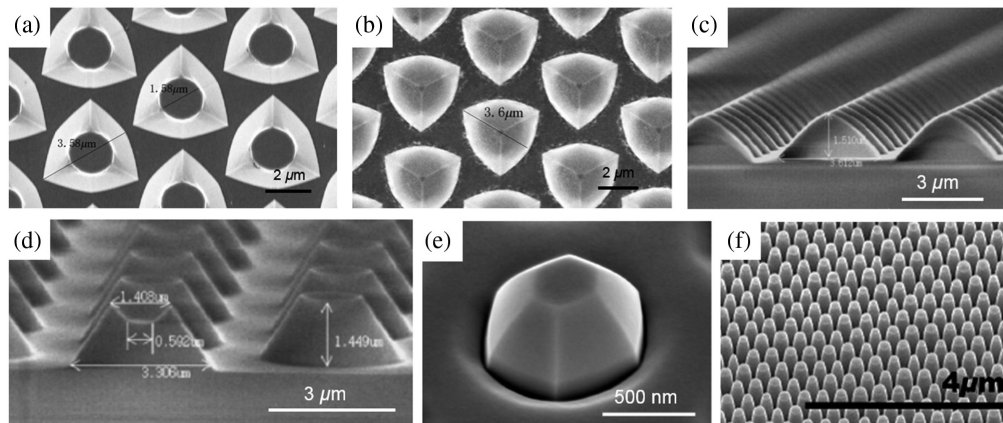
Fig. 16 SEM images show PSS shapes fabricated by subtractive techniques: (a) triangle platform, reproduced with permission from Ref. 82 (b) triangle cone, reproduced with permission from Ref. 82 (c) hemispheric, reproduced with permission from Ref. 83 (d) volcano, reproduced with permission from Ref. 83. SEM images show patterns fabricated on sapphire substrates by additive technique: (e) GaN hexagonal cones, reproduced with permission from Ref. 84 and (f) self-assembled patterned AlN NRs, reproduced with permission from Ref. 73.

Table 3 summarizes the reported achievements acquired from the use of PSSs for UV-photonic devices.

4.2.1 *PSS fabrication for UV applications: additive techniques*

NIL was used to pattern a nanoholes array on a planar AlN/sapphire template. AlGaN/AlN MQW grown on such templates showed a lasing emission at 271.9 nm with a threshold power density lower by 68% than that of the same MQW grown on planar AlN/sapphire templates.[89] This reduction in the threshold power density is attributed to the improvement in the structure quality reflected by the TDDs in the structure grown on nanopatterned AlN/sapphire templates.

Nanoscale patterning in an AlN layer, resulting in self-assembled NRs on a sapphire substrate as shown in Fig. 16(f), was prepared by an inductively coupled plasma (ICP) etching using a self-assembled monolayer of silica spheres on the AlN layer as a lithographic mask.[73] Growing an AlN layer above these NRs, a reduction in the edge-type dislocation density by approximately two orders of magnitude is demonstrated. Crack-free UV-LEDs emitting at 280-nm wavelength

Table 3 Summary of achievements acquired from the use of PSSs for UV-photonic devices.

| PSS shape	Lithography method	Device/structure	Wavelength (nm)	Enhancement/achievement	Ref.
Stripe	Photo-	InGaN/GaN LEDs	400 (UVA)	127% (output power)	85
Volcano	Photo-	InGaN/GaN LEDs	380 (UVA)	2.8 larger LEE	83
Nano-	Nanosphere	AlGaN-based LEDs	282 (UVB)	98% (output power) with 3.45% EQE	86
Microlenses	Photo-	Flip-chip AlGaN-based LEDs	280 (UVB)	55% (output power)	87
Nanorods	Nanosphere	AlGaN-based LEDs	280 (UVB)	67% (output power)	74
Groove	Photo-	AlGaN-based LEDs	278 (UVC)	8.4 mW output power with 3.4% EQE	88
Nanoholes	Nanoimprint	AlGaN/AlN MQW with lasing emission	271.9 (UVC)	68% reduction in the threshold power density	89
Groove	Photo-	AlGaN-based LEDs	266 (UVC)	5.3 mW output power with 1.9% EQE	88
Hybrid photonic nanostructure	Nanoimprint	Flip-chip AlGaN-based LEDs	265 (UVC)	About 20 times (output power)	90
Hybrid photonic nanostructure	Electron-beam	Flip-chip AlGaN-based LEDs	265 (UVC)	196% (output power)	91
Nanorods	Lithography-free	Core-shell-type AlGaN/AlN MQW	260 (UVC)	40-times (PL intensity)	92

have been successfully grown on a 4-in. AlN-NRs/sapphire substrates.[74] The latter was fabricated by utilizing nanosphere lithography [Fig. 14(a)] and ELOG. The output power of these LEDs is enhanced by 67%. This enhancement is attributed to the formation of embedded periodic air-voids-incorporated nanoscale patterns [Fig. 14(b)], which cause an improvement in the crystal quality of epitaxial layers. Simultaneously, the LEE of this device is enhanced by breaking the predominant in-plane-guided propagation of the photons.

Recently, AlN NRs were prepared on a sapphire substrate by a catalyst/lithography-free method, which is polarity-selective epitaxy and etching.[92] Core–shell-type AlGaN/AlN MQW emitting at 260-nm wavelength and grown on these AlN NRs show an improvement by 40 times in the PL intensity compared with the same structure grown on planer AlN template.

4.2.2 PSS fabrication for UV applications: subtractive techniques

Stripe PSSs have been suggested to improve the light-output efficiency of near-UV-LEDs emitting at around 409-nm wavelength.[93] These substrates were fabricated by a standard photolithography method and etched by the ICP etching. The LEDs grown on such a stripe PSS showed an enhancement in the LOP ~20% over the same LEDs grown on the nonpattern sapphire substrate. In addition to the reduction in TDDs, this enhancement is attributed to the geometric effect of the stripe PSS adding the escape probability of the guided light. Furthermore, Pan et al. studied the effects of both the stripe depth and the stripe orientation on the performance of GaN-dased LEDs emitting at 400-nm wavelength.[85] They employed a set of PSSs with periodic stripe patterns prepared by photolithography and wet chemical etching. The output power of LEDs is enhanced by 87% when they were grown on a 0.9-μm-deep PSS with stripes along <11-20> direction. Further an improvement of 40% in the output power was achieved when the LEDs were grown on a 0.9-μm-deep PSS with stripes along the <1-100> direction.

Hemispherical- and volcano-shaped PSSs, shown in Figs. 16(c) and 16(d), respectively, were also suggested to enhance the LEE of GaN-based LEDs.[83] The LEE of LEDs emitting at 380 nm
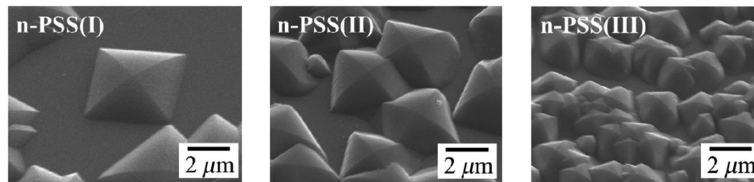
Fig. 17 Pyramidal-shaped PSS substrates prepared without lithography. Reproduced with permission from Ref. 97.

and grown on the optimized volcano-shaped PSS is higher by about 2.8 times than that of the LED grown on the planar sapphire substrate and is enhanced by about 1.6 times in comparison with that of the LED grown on the hemispherical PSS. Zhou et al.[94] studied the effects of the of PSS size on the performance of UV-LEDs emitting at 375 nm. In this study, they used cone-shaped PSS with different sizes that were fabricated by a combination of the thermal-reflow photoresist technique and an ICP etching process. They found that with increasing both the pattern size and PSS fill factor, the TDDs in UV-LEDs decrease. This is due to a reduced GaN island density that causes fewer grain boundaries and also due to an increased lateral overgrowth area of GaN. Consequently, an improvement in the IQE and LOP of the LED is observed; the output power of the UV-LED grown on a large PSS with a fill-factor (FF) of 0.71 was 131.8% higher than that of the same LED grown on a small PSS with a FF of 0.4.

In 2013, Dong et al.[86] fabricated nano-PSSs by nanosphere lithography and have demonstrated the advantage of using these PSSs to enhance the performance of AlGaN-based deep UV-LEDs. In particular, the output power of the UV-LED emitting at 282-nm wavelength of about 3 mW with 3.45% EQE is enhanced by ~98% compared with that of the UV-LED grown on the nonpatterned substrate. LIL combined with dry-etching and MOCVD has been used to fabricate highly periodic AlN lateral polar structures on a sapphire substrate with submicron domain widths.[95] Such structures can be used for quasiphase matching to exploit frequency doubling via second harmonic generation in UV-C.

Using a double-sided PSS for GaN-based LEDs, an improvement in the device performance is numerically predicted for different pattern shapes.[96] Experimentally, nanoscale patterns on a double-sided sapphire substrate were fabricated using NIL and ICP etching. The output power of the LED grown on the double-sided PSS was 52% greater than the control sample. Furthermore, the use of a double-sided patterned substrate results in an increase in the heat dissipation efficiency and hence a decrease in the LED thermal resistance. Pyramidal-shaped PSS substrates were prepared by a wet-etching without lithography and dry-etching processes.[97] Figure 17 shows the pattern morphology of three substrates used for this study. LEDs grown on these substrates showed an enhancement in the output power by ~46.4 to 51.5% compared with that of the same LEDs grown on flat sapphire substrates. Furthermore, LEDs are grown on the n-PSS(III) substrate (Fig. 17) with 73% pattern coverage has the highest output power.

4.2.3 *PSS for flip-chip UV-LEDs*

Flip-chip designs have been used for AlGaN-based UV-LEDs because conventional LED contact layer material is absorbing in the UV spectral range. To enhance the LEE of flip-chip UV-LEDs, an approach to integrate monolithic arrays of the microlens to sapphire substrates was suggested.[87] In particular, UV-LEDs were bonded on high thermal conductive AlN ceramic submounts to improve the thermal dissipation, whereas the emitted UV light was extracted through sapphire substrates with microlenses. The latter were fabricated by photoresist reflow and dry-etching. An enhancement by 55% in the output power at 20 mA is reported for a UV-LED emitting at 280-nm wavelength with microlenses compared with the same structure fabricated without microlenses.[87] This enhancement is attributed to the reduced internal reflections of the light caused by the microlens surface profile.

Groove-shaped PSSs were fabricated using photolithography and dry-etching. A high-quality lateral epitaxy overgrowth-AlN templates grown on these PSSs have enabled to realize flip-chip AlGaN-based UV-LEDs that are emitting at 266- and 278-nm wavelengths with an output
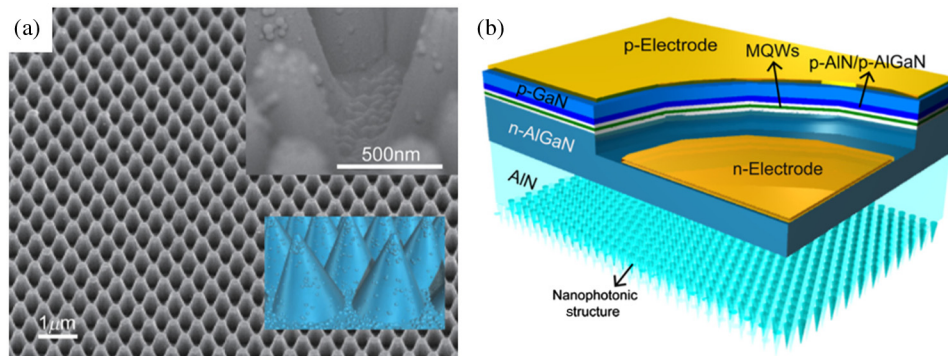
Fig. 18 (a) SEM image of fabricated light extraction structures: a triangular lattice of circular AlN cones with subwavelength nanostructures. The insets show an enlarged SEM image and a schematic. (b) Schematic of UV-LED grown on an AlN substrate with nanophotonic light extraction structures. Reproduced with permission from Ref. 91.

power of 5.3 mW with 1.9% EQE and 8.4 mW with 3.4% EQE, respectively.[88] Flip-chip UV-LEDs on AlN substrates show a relatively low light extraction and low output power. This is due to the total internal reflection (Fresnel reflection) at the interface between the AlN surface and the ambient medium and to the internal optical absorption by the p-GaN contact layer and the bulk AlN substrate. To overcome the problem of the Fresnel reflection, the AlN bottom-side surface was constructed to have a configuration composed of a hybrid structure of PhCs and subwavelength nanostructures. This hybrid structure is shown in Fig. 18(a) and was realized using EBL and subsequent ICP etching.[91] Growing a UV-LED emitting at 265 nm on the resulting AlN substrate consequently led to an enhancement in the LED output power by 196% (the output power of 90 mW at 350 mA). Figure 18(b) shows a schematic drawing of the UV-LED used for this study.

Despite the advantage of this relatively high output power achieved in the aforementioned study,[91] the employed fabrication method, i.e., EBL, is time-consuming, and hence this limits the patterned device size. To overcome this issue, a large-area AlN nanophotonic light-extraction structure fabricated by NIL is used to realize UV-LEDs emitting at 265 nm.[90] Furthermore, an improved design of a multiple-strip p-electrode geometry for these LEDs results in a uniform current density distribution. Consequently, an output power higher than 150 mW has been recorded with low-efficiency droop. Also, an increase by ∼20 times in the output power over that of a conventional flat-surface LED was achieved.

4.2.4 Substrate sidewall roughening

Substrate sidewall roughening is an approach suggested to enhance the LEE of AlGaN-based UV-LEDs.[98] This approach has revealed that a roughening region for effective light extraction enhancement exists on the substrate's sidewall. Roughening outside the effective roughening region will degenerate the sidewall light extraction due to inward photon scattering and absorption. Picosecond laser dicing was used to form roughening layers on the substrate's sidewalls without introducing thermal damage. A UV-LEDs emitting at 275-nm wavelength with three roughening layers shows 13.2% higher output power than the same LEDs with two roughening layers.[98]

4.2.5 Patterning non-sapphire substrate for UV applications

A UV-LED emitting at 359-nm wavelength was fabricated on a stripe-patterned Si substrate.[99] To achieve this, a fully coalesced ELOG AlN layer with a 7-μm thickness was used as a template for the UV-LED growth. This LED was fabricated in back-emission configuration, and the Si substrate was removed after the flip-chip bonding. An enhancement in the output light extraction by 50% is observed for the back-emission LED compared with the top emission one. Likewise, a high crystal quality AlN template was used to grow an AlGaN-based UV-LED on a microcircle-

patterned Si substrate.[100] The latter was achieved using standard lithography and ICP etching. The fabricated UV-LED emits at 325 nm with an EQE of about 0.03%.

Cantilever epitaxy method was used to grow AlN layers on 200-nm-nanopatterned Si substrate.[101] This substrate was patterned into nanostripes with nominally 150-nm wide ridges and 50-nm wide trenches Si, with an etching depth of 100 nm using EBL and dry-etching. The resultant AlN/Si structures were used as templates to grow UV-LEDs emitting at 344-nm wavelength with a peak pulse power of about 0.7 mW.

4.3 Surface Roughening

Surface roughening has been proven to be an effective approach to enhance the LEE of UV-LEDs. Next, we grouped the surface roughening into surface texturing and surface patterning.

4.3.1 Surface texturing

Surface texturing architectures help to improve the surface emission area and increase the probability of photons to escape out of the surface by the angular randomization.[102] Lee et al.[102] fabricated a UV-LED device emitting at 365 nm and obtained a total enhancement by a factor of 7.8 compared with the conventional UV-LED. This is attributed to the surface structuring, which exhibits random scattering effects. Figure 19(a) shows the schematic of the devices showing the roughening surface with root-mean-square (rms) roughness of ∼398 nm by immersing the sample in 45 wt. % KOH at 110°C for 180 s.[102] Figure 19(b) shows the L–I–V characteristics of three samples emphasizing the enhancement in the overall performance toward surface-roughened LED. Furthermore, Chiang et al.[103] achieved an enhancement in the output power by 525% and in the EQE by 6.5 times for a UVLED emitting at 365 nm, compared with a conventional LED, by a combination of the noninsulation current blocking layer, wafer bonding, laser lift-off, and surface treatment processes. Figures 19(d) and 19(e) show a schematic drawing of the fabrication steps and SEM images for the roughened surface, respectively. A high improvement in the L–I–V characterization was realized as shown in Fig. 19(e).

Inoue et al.[90] reported a high output power of 150 mW of a UV-LED operating at 265 nm. The UV-LED structure was fabricated on AlN substrate to minimize the lattice and thermal expansion mismatches between the substrate and the epitaxial layers. However, the high refractive index (RI) of the AlN substrate results in a small light escape cone angle. Imprinted polymer patterns by NIL were performed to create a large-area AlN nanophotonic structure, which was capable of reaching an improved EQE by ∼4 times compared with a flat LED, as shown in Figs. 19(f)–19(h). Chiang et al.[104] have suggested an abraded surface structuring method for a thin-GaN (NTG) UV-LED as shown in Fig. 19(i). As a result, the LED emitting at 365 nm shows an output power enhancement of ∼18.3% to 27.4% and EQEs of 20% to 27.2% at an injected current of 700 and 1500 mA, respectively. The enhancements in the output power and the EQE were attributed to the elimination of the electrode effect due to a micrometer-range abraded surface modification after an etching process using KOH solution. Additionally, a 2.5-times light extraction gain has been reported by Zhou et al.[105] by utilizing a roughening process using photoelectrochemical etching. As a result, an enhancement output power of ∼4.6 and ∼2.5 times was achieved for 280- and 325-nm emitting LEDs, respectively.

Khizar et al.[87] have reported an enhancement by 55% in the output power of the UV-LED emitting at 280 nm by integrating monolithic microlens arrays. This is due to curvature surface profile of the microlenses, which helps in increasing light reflections, in which more light can be extracted and as a result, LEE is enhanced. In a subsequent report, Kim et al.[106] demonstrated an enhanced LEE by 23% for UV-LED emitting at by utilizing SiO_2 nanosphere arrays. The nanosphere arrays act like nanolenses with a hexagonal-like pattern when immersed into a BCB resin and undergo a heat treatment. The hemispherical pattern leads to the random direction of the light rays with the LEE increased by multiscattering effects. Recently, Liu at al.[107] characterized a UV-LED that operates at 214 nm via nanowalls structures and calculated an IQE of 60%. Alternative nanostructures features have been detailed by others, e.g., large-scale nanostructure nanosphere,[108] silica glass with tailored nanostructures,[109] and truncated cones.[110]
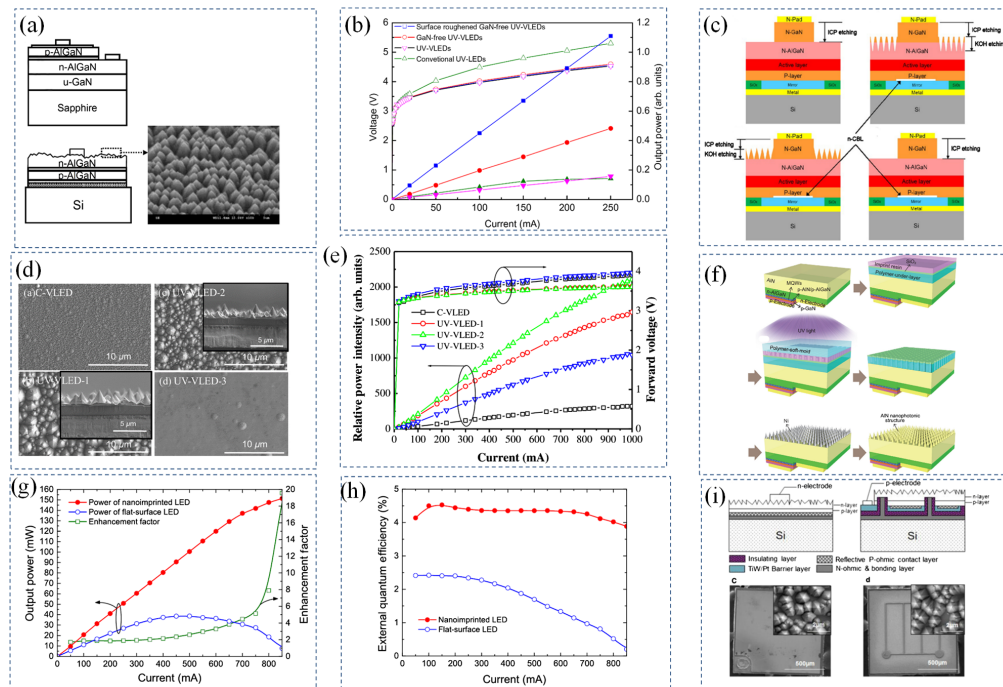
Fig. 19 (a) Schematic of the conventional LED (top) and the roughened LED (bottom) with SEM image (inset). Reproduced with permission from Ref. 102. (b) L–I–V characteristics of the samples. Reproduced with permission from Ref. 102. (c) Schematic of the fabrication steps for the UV-LED. Reproduced with permission from Ref. 103. (d) SEM images under different etching conditions. Reproduced with permission from Ref. 103. (e) L–I–V characteristics of UV-LEDs. Reproduced with permission from Ref. 103. (f) Schematic of the fabrication steps for the nanophotonic light-extraction structure. Reproduced with permission from Ref. 90. (g) Output power and enhancement factor. Reproduced with permission from Ref. 90. (h) EQE as a function of the current. Reproduced with permission from Ref. 90. (i) Schematic and SEM images of devices with the micro abraded surface (insets). Reproduced with permission from Ref. 104.

4.3.2 Surface patterning

Recently, a light-extraction mechanism based on an Rh mirror electrode and a transparent p-type AlGaN:Mg contact layer has been investigated by Takano et al.[111] They successfully achieved a 20% enhancement in EQE at an emission wavelength of 275 nm. In this work [Fig. 20(a)], a conventional AlGaN LED is modified into a UV-LED structure by utilizing the following features: (1) crack-free AlN on the patterned sapphire substrate, (2) AlGaN:Mg p-type contact layer, (3) mirror electrode, and (4) Si encapsulation resin. The encapsulation resin helped to reduce the optical loss and reached 89% transmission. Implementing Rh mirrors into the LED structure results in an improvement in output power from 3.9 to 18.3 mW at 20 mA and in the EQE from 4.3% to 20.3% in comparison with the conventional LEDs. Increased multireflection of the light in the chip and absorption reduction helps to improve the device performance. Figure 20(b) shows the device characteristics (output power and EQE). The encapsulated LED in hemispherical resin on a Si submount is shown in Fig. 20(c). Encapsulation using other UV-transparent material, e.g., AlN-doped fluoropolymer and BVE polymer with –CF₃ ends, has been demonstrated recently.[113,114] Additionally, several research groups demonstrated pixel-LEDs (by meshing the p-contact metals) to enhance the output power and EQE characteristics.[115,116] However, the pixels were fabricated at the microscale and introduced complexity into the LED fabrication.

A 70% improvement in output power at peak emission of 276 nm has been reported by Fayisa et al. by employing an inclined sidewall at the p-GaN with MgF₂/Al omnidirectional reflectors.[112] Figure 20(d) shows the schematic fabrication process of AlGaN-based UV-LEDs with a 5 × 5 array of the microring active mesa. The microring array consists of a truncated
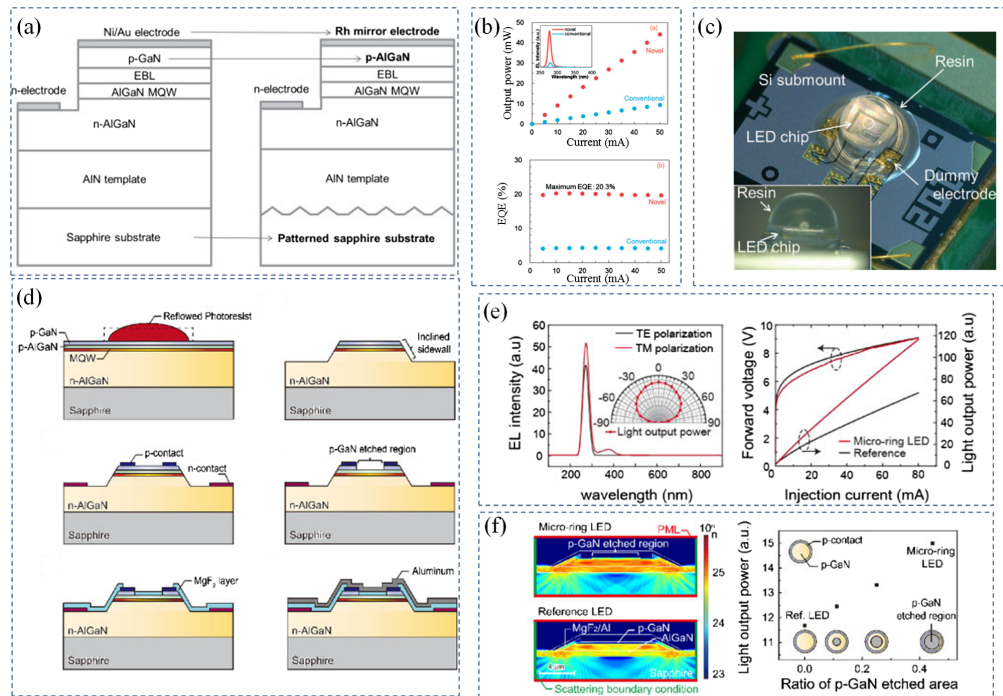
Fig. 20 (a) Schematics of conventional (left) and UV-LEDs (right). Reproduced with permission from Ref. 111. (b) Output power (top) and EQE (bottom) characteristics. Reproduced with permission from Ref. 111. (c) Encapsulated UV-LED in hemispherical resin. Reproduced with permission from Ref. 111. (d) Schematic of fabrication steps for UV-LED with micro-ring active mesa. Reproduced with permission from Ref. 112. (e) EL spectra of TE and TM polarized light with the angle-dependent output power profile (inset) and L–I–V curve of the devices. Reproduced with permission from Ref. 112. (f) Electrical field distribution of the devices (left) and the calculated output power of the devices as a function of the etched area to mesa ratio (right). Reproduced with permission from Ref. 112.

cone-shaped active mesa, which is covered by the inclined MgF_2 sidewall of Ti/Al/Ni/Au ohmic contacts. The p-GaN-layer etching was performed by ICP etching to reflect photons down to the substrate without being absorbed. Decreasing the light absorption and directing strong sidewall-heading TM polarized light via the MgF_2/Al reflectors leads to significant enhancement in the LEE and output power as shown in Figs. 20(e) and 20(f), respectively.

Table 4 summarizes the recent applications of surface roughening to enhance the performance of UV-LEDs. In this table, the device characteristics are described regarding initial emission wavelength (λ_o), initial threshold current (I_o), and initial output power (P_o).

4.4 Photonic Crystals

PhCs are inhomogeneous dielectric structures with periodic modulation of the RI, which allows the control and manipulation of the light propagation. PhCs can form a photonic bandgap where the light cannot propagate through the structure within a range of frequencies. Concerning the geometry of the structure, PhCs can be divided into one-, two-, and three-dimensional (1-D, 2-D, and 3-D) PhCs. In 1-D PhCs, the periodic modulation of RI occurs in one direction only, whereas RI stays uniform in the other two directions. 1-D PhCs have been widely used for several photonic devices, e.g., LDs, LEDs, and PDs in the form of a distributed Bragg reflector (DBR) as a highly reflective mirror. The most important aspect of the 2-D/3-D PhCs design is the lattice pattern choice. Most widely studied two-dimensional (2-D) PhCs either are with a hexagonal (triangular) or square lattices. In general, 1-D PhCs can be formed using thin-films deposition at various growth temperatures to suit the material or process requirements.[117–123] As for the 2-D/3-D PhCs, it can be fabricated using EBL, photolithography, NIL, or direct laser writing, followed by various etching techniques to form the air holes or pillars of a layer.[124–128]

Table 4 Recent progress of using surface roughening approach for UV-LEDs improvements.

Technique	Device	Device characteristic			Enhancement	Ref.
		λ_o (nm)	I_o (mA)	P_o (mW)		
Surface structuring	UVC-LED	265	850	150	20-fold (P_o)	90
	UVC-LED	280	NA	NA	2.5× (LEE)	105
	UVA-LED	365	350	858	6.5× EQE and 525% in P_o	103
	UVA-LED	365	250	NA	7.8× (P_o)	102
	UVA-LED	365	1500	700	20% in EQE and 18.3% (P_o)	104
Nanostructures features	UVC-LED	214	170	NA	60% (EQE)	107
	UVC-LED	250	50	7.89	8.6% in light emission	109
	UVC-LED	275	20	11.6	20% (EQE)	111
	UVC-LED	280	200	472	70% (P_o)	112
	UVC-LED	280	20	0.2-0.3	55% (P_o)	87
	UVC-LED	280	100	NA	37% in light emission	110
	UVA-LED	375 to 400	NA	NA	23% (PL)	106
	UVA-LED	370	Na	NA	2.5 fold in band edge luminescence	108
Encapsulates	UVC-LED	280	200	472	1.5× (LEE)	114
	UVC-LED	280	120	NA	16.4% (P_o)	113

4.4.1 *1-D Photonic crystals: distributed Bragg reflector*

A DBR is formed by multiple stacking of two alternate high and low RI layers with the thickness of each layer equivalent to the quarter-wave of the designated wavelength. DBRs have been used as high reflective mirrors in many UV-based photonic devices (summarized in Table 5), e.g., vertical-cavity surface-emitting laser (VCSEL),[129–131] edge-emitting laser (EEL),[139] microdisk LD,[137] resonant-cavity LED (RCLED),[132] resonant-cavity PD (RCPD),[133] and LEDs.[70,134–136,138] These DBRs were formed using oxides named as UV-dielectric DBR and group III-nitride semiconductors, named as UV-nitride DBR. Most of the aforementioned UV-based photonic devices require DBR(s) with high reflectivity, $R > 99\%$. To achieve such a high R, the contrast in RI must be high to have a smaller period and broad stopband, the chosen materials exhibit a high transparency at the device operating wavelength, the material interfaces must be abrupt with smooth surface to reduce the optical loss, and the chosen materials are compatible with lattice-matching to subsequent material deposition/growth.

Compared with UV-nitride DBRs, UV-dielectric DBRs offer more extensive material choices (no lattice-matching limitation) and flexibility in the material growth or deposition technique, e.g., sputtering, PECVD, and electron beam evaporation. Importantly, highly reflective DBR ($R > 99\%$) and broad stopband (>30 nm) can be easily obtained within a small number of repetitions (typically 10 to 15 periods) due to the high RI contrast among oxide materials. Table 6 lists some examples of oxides-based DBRs that have been demonstrated in the UV spectral range, e.g., ZrO_2/SiO_2,[140] Ta_2O_5/SiO_2,[129] TiO_2/SiO_2,[130] and Si_3N_4/SiO_2[141] for UV-A; Al_2O_3/SiO_2[142] for UV-B; HfO_2/SiO_2[143] and YDH/SiO_2[144] for UV-C, respectively.

SiO_2 is commonly used as the low RI layer in UV-dielectric DBRs as it offers the lowest RI among the dielectrics and has wider energy bandgap. However, most of the materials used for high RI layer in the UV-A DBRs are not transparent at the UV-B and UV-C spectral ranges. Although Al_2O_3 is transparent for extensive range till vacuum-UV,[142] a high number of period

Table 5 UV-dielectric DBRs and nitride DBRs employed in various photonic devices operating in the UV regime.

Technique	Device	Device structure (top-down)	Device characteristic	Enhancement	Ref.
Top and bottom DBRs	UV-LD (VCSEL)	13.5× Ta_2O_5/SiO_2 InGaN/GaN MQW 13.5× Ta_2O_5/SiO_2	Lasing at 397 nm (optical pumping) and 65% polarization	PL narrowed (0.13 nm)	129
	UV-LD (VCSEL)	6× TiO_2/SiO_2 InGaN/GaN MQW 35× $GaN/Al_{0.34}Ga_{0.66}N$	Lasing at 381 nm (optical pumping)	PL narrowed (8 to <0.1 nm)	130
	UV-LD (VCSEL)	7× HfO_2/SiO_2 InGaN/AlGaN MQW 40.5× $GaN/Al_{0.12}Ga_{0.88}N$	Lasing at 374.9 nm (optical pumping)	PL narrowed (0.66 nm)	131
	UV-LED (RCLED)	2.5× ZrO_2/SiO_2 InGaN/GaN MQW 20× $GaN/Al_{0.27}Ga_{0.73}N$	EL at 390 nm and EQE of 1.2%	—	132
	UV-PD (RCPD)	3× $Al_{0.3}Ga_{0.7}N/AlN$ p-GaN/i-GaN/n-$Al_{0.3}Ga_{0.7}N$ 20.5× $Al_{0.3}Ga_{0.7}N/AlN$	Response at 330 nm and EQE of 48%	—	133
Bottom DBR	UV-LED	InGaN/GaN MQW 9.5× HfO_2/SiO_2	EL at 390 nm	36% (TDDs) 75% (output power)	70
	UV-LED	AlInGaN/AlGaN MQW 16× Ta_2O_5/SiO_2	EL at 365 nm	25% (output power, EQE, and LEE)	134
	UV-LED	GaN/AlGaN MQW 12× $Al_{0.085}Ga_{0.915}N/air$	PL at 359.7 nm with linewidth of 11.43 nm (optical pumping)	PL at 365.2 nm with linewidth narrowed (1.18 nm)	135
	UV-LED	AlInGaN/AlInGaN MQW 25× $Al_{0.16}Ga_{0.84}N/Al_{0.49}Ga_{0.51}N$	EL at 350 nm	2.3× (EL and output power)	136
Top DBR	UV-LD (microdisk)	25× $Al_{0.2}Ga_{0.8}N/AlN$ GaN microdisk	Lasing at 377 to 379 nm (optical pumping)	—	137
	UV-LED (flip-chip)	14× Ta_2O_5/SiO_2 AlGaN/AlGaN MQW	EL at 353 nm	25% (output power)	138
Side DBR	UV-LD (EEL)	5× and 6× HfO_2/SiO_2 AlGaN/AlGaN MQW	Lasing at 249 nm (optical pumping)	28% (threshold pumping power)	139

is required (>40 periods) and the DBR stopband is not so broad due to insufficient RI contrast. Replacing Al_2O_3 by HfO_2 as the high RI layer for the DBR is interesting because of high RI contrast. However, HfO_2 is absorbing for wavelengths below 250 nm. Recently, a highly reflective UV-C dielectric DBR has been demonstrated using a YDH/SiO_2 material system.[144] Figure 21(a) shows that YDH thin films are less absorbing compared with HfO_2 thin films across the UV wavelengths. In Fig. 21(b), the YDH thin films exhibit wider energy bandgap of ~6.21 eV compared with the HfO_2 thin films as measured using a phase-modulated spectroscopic ellipsometry.[145] This increase in energy bandgap indicates the transparency of the YDH material in the UV-C wavelengths especially below 250 nm. Figure 21(c) shows the reflectivity spectrum of 15 periods YDH/SiO_2 DBR and the transmission spectrum of single-layer YDH thin films as a function of the wavelength. The reflectivity peak of $R \sim 99.9\%$ of the DBR is obtained before the absorption from YDH becomes dominant. The achieved stopband of ~50 nm is quite extensive within the UV-C regime. The inset of Fig. 21(c) shows the cross-sectional SEM micrograph of the DBR structure indicating a uniform period thickness distribution with minor roughness introduced.

Table 6 Examples of UV-dielectric DBRs demonstrated in UV wavelengths.

Material system	Number of period	Reflectivity (%)	Center wavelength (nm)	Stopband (nm)	Remark	Ref.
ZrO_2/SiO_2	15	99.5	399 (UVA)	—	Top mirror InGaN VCSEL	140
Ta_2O_5/SiO_2	13.5	99.2	396 (UVA)	—	Top and bottom mirrors InGaN VCSEL	129
TiO_2/SiO_2	6	97.0	381 (UVA)	—	Top mirror InGaN VCSEL	130
Si_3N_4/SiO_2	9	95.0	355 (UVA)	80	Top mirror GaN microcavity	141
Al_2O_3/SiO_2	42.5	99.0	296 (UVB)	26 to 39	Mirror only	142
HfO_2/SiO_2	11.5	250	250 (UVC)	45	Mirror only	143
YDH/SiO_2	15	99.9	240 (UVC)	50	Mirror only	144
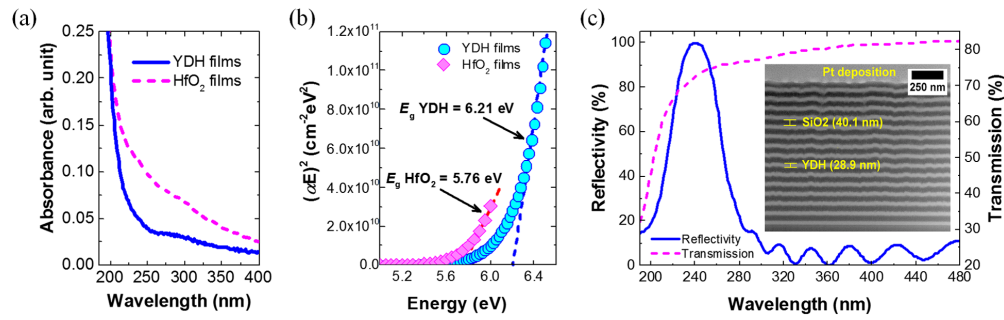
Fig. 21 The YDH/SiO_2 DBR characteristics showing (a) absorbance spectra comparison for YDH and HfO_2 single-layer films in the UV regime, (b) Tauc plot indicates the energy bandgap for YDH and HfO_2 single-layer films, and (c) reflectivity spectrum for 15 periods DBR and the transmission spectrum for a single-layer YDH films with the inset shows the cross-sectional SEM of the DBR structure. Reproduced with permission from Ref. 144.

Despite the advantages of the UV-dielectric DBRs, e.g., extensive material choices, fabrication flexibility, highly reflective, high RI contrast, and the wide stopband, the major drawback is that they are not electrically conductive and the thermal conductivity is mostly low. A complex current injection device scheme, e.g., intracavity[132,134] or flip-chip,[138] is required to pump a LEDs with dielectric DBRs electrically. Moreover, the poor thermal conductivity of dielectric DBRs deters the dissipation of heat generated during lasing operation. To overcome limitations, epitaxially grown UV-nitride DBRs have been developed using lattice-mismatched material [(Al)GaN/Al(Ga)N-based, e.g., GaN/AlN,[146] GaN/AlGaN,[147–150] AlGaN/AlGaN,[151] AlGaN/AlN,[152–154] and boron-containing nitride, i.e., BAlN/AlN[155]], lattice-matched material (AlInN/AlGaN),[156–159] and nitride-porous (AlGaN/air) material.[135] The advantage of the UV-nitride DBRs is that they can be monolithically grown and doped (either p- or n-doped for electrical pumping), and they are furthermore thermally conductive. However, obtaining crack-free DBRs is challenging due to the limitation in crystal growth (substrate compatibility, i.e., lattice- and thermal expansion-mismatch, and accumulation of tensile stress) and inadequate RI contrast, i.e., higher periods are required which is challenging for crystal growth in addition to the narrow DBR stopband. It is becoming more critical when the wavelength is shorter (at UV-C), where AlGaN/AlGaN DBR needs to be used to avoid absorption issue, but at the same time facing more difficulty in growing high-quality crystal (penalty of higher Al composition) and reduction in RI contrast. Recently, several strain-management techniques (as summarized in Table 7 and shown in Fig. 22) have been demonstrated for growing lattice-mismatched UV-nitride DBRs to suppress the cracks formation and to reduce the mismatch-induced tensile stress.

Table 7 Strain management techniques demonstrated for lattice-mismatched UV-nitride DBRs.

Technique	Material system	Number of period	Reflectivity (%)	Center wavelength (nm)	Stopband (nm)	Remark	Ref.
GaN/AlN SLs	GaN/AlN on GaN template	20	97.0	399 (UVA)	14	Mirror only	146
AlN/AlGaN double buffer	GaN/$Al_{0.2}Ga_{0.8}$N on 6H-SiC substrate	30	92.0	395 (UVA)	14	Mirror only	147
Thin GaN single buffer	GaN/$Al_{0.34}Ga_{0.66}$N on GaN template	35	96.0	390 (UVA)	14	Mirror only	148
AlN/GaN/AlN multilayer	GaN/$Al_{0.27}Ga_{0.73}$N on GaN template	20	90.0	384 (UVA)	18	Mirror only	149
AlN interlayer	GaN/$Al_{0.2}Ga_{0.8}$N on GaN template	60	99.1	378 (UVA)	—	Mirror only	150
GaN interlayer	$Al_{0.04}Ga_{0.96}$N/$Al_{0.3}Ga_{0.7}$N on AlN template	45	95.4	368 (UVA)	15	Mirror only	151
Thick AlN single buffer	$Al_{0.43}Ga_{0.57}$N/AlN on sapphire substrate	29.5	99.0	356 (UVA)	20	Mirror only	152
Wider energy bandgap	BAlN/AlN on AlN template	18	82	311 (UVB)	20	Mirror only	155
		24	60	282 (UVB)	16	Mirror only	155
Trilayer period	$Al_{0.5}Ga_{0.5}$N/$Al_{0.96}In_{0.04}$N/$Al_xIn_{0.02}Ga_{0.98-x}$N on AlGaN template	20	86	274 (UVC)	16	Mirror only	160
Balanced strains	$Al_{0.65}Ga_{0.35}$N/AlN on AlN template	25.5	97.7	273 (UVC)	9	Mirror only	153
AlN LT renucleation	$Al_{0.65}Ga_{0.35}$N/AlN on AlN template	15.5	97.7	272 (UVC)	9	Mirror only	154

In Fig. 22(a), a crack-free 20 periods of GaN/AlGaN DBR is realized by inserting three sets of Ga/AlGaN superlattices (SLs) at several positions during the DBR growth.[146] The reflectivity at 399 nm wavelength is ∼97%. A similar technique was demonstrated by Moudakir et al.,[149] where a multilayer (can be considered as SLs) of AlN/GaN/AlN was inserted at the midpoint of a GaN/AlGaN DBR to suppress the crack generation. For the crack suppression using the buffering technique, Someya and Arakawa[148] [Fig. 22(b)] found that a highly reflective and crack-free GaN/AlGaN DBR can be grown as long as the thickness of the GaN buffer layer is <400 nm. Using a thick AlN buffer layer (∼1 μm), a highly reflective and crack-free DBR based on AlGaN/AlN with 29.5 periods was obtained at 356-nm operating wavelength [see Fig. 22(c)].[152] The use of a thick AlN buffer layer keeps the AlGaN layers in compressive stress, whereas the AlN layers were strain-free. A double-layer buffer (using AlN/AlGaN) was also proposed to grow a crack-free and highly reflective GaN/AlGaN DBR on a SiC substrate.[147]

Additionally, an interlayer of GaN or AlN at any point of the UV-nitride DBR structure can be utilized to suppress the crack existence in UV-nitride DBR. Using a thin interlayer, the existence of tensile strain can be compensated.[150] Figure 22(d) shows that a crack-free AlGaN/AlGaN DBR can be realized after a GaN interlayer is grown after the initial growth of the AlN template on a sapphire substrate.[151] A highly reflective DBR is obtained using 45 periods. The crack suppression is still well managed for a thicker GaN/AlGaN DBR (with 60 periods) using few AlN interlayers at several midpoints during the DBR growth.[150] In Fig. 22(e), Abid et al.[155] reported a boron-containing nitride DBR using wider energy bandgap material in the form of BAlN/AlN DBR. This material system has higher RI contrast, which resulted in
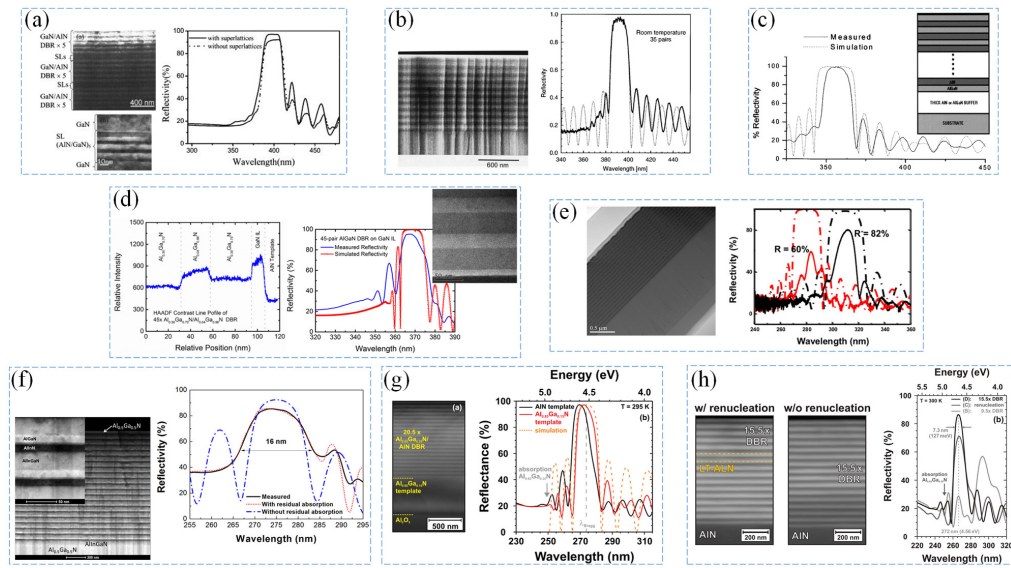
Fig. 22 Various strain-management techniques demonstrated for lattice-mismatched nitride-DBRs resulted in high reflectivity mirror at UV wavelengths and crack-free DBR structure as indicated by the cross-sectional SEM micrographs. (a) GaN/AlN SLs. Reproduced with permission from Ref. 146. (b) Thin GaN single buffer. Reproduced with permission from Ref. 148. (c) AlN single buffer. Reproduced with permission from Ref. 152. (d) GaN interlayer. Reproduced with permission from Ref. 151. (e) Wider energy bandgap. Reproduced with permission from Ref. 155. (f) Trilayer period. Reproduced with permission from Ref. 160. (g) Balanced strains. Reproduced with permission from Ref. 153. (h) AlN-LT nucleation. Reproduced with permission from Ref. 154.

a wider stopband (16 to 20 nm) and exhibits less optical absorption than the AlGaN-based DBRs. However, obtaining a high-quality BAlN layer is challenging, which explains the low reflectivity characteristic of the grown DBRs. Recently, several UV-nitride DBRs were demonstrated for UV-C spectral range using advanced techniques, e.g., trilayer period,[160] balanced strains,[153] and AlN low-temperature (LT) renucleation.[154] In the technique of trilayer period [Fig. 22(f)], a period of the DBR consists of three layers, i.e., AlGaN, AlInN, and AlInGaN was used to accommodate the lattice mismatch instead of simply using bilayer, which is typical for a DBR. As for the balanced strains technique [Fig. 22(g)], a crack-free AlGaN/AlN DBR is obtained by counterbalancing the tensile and compressive stress build-up (using a certain Al composition). As for the AlN low-temperature (LT) renucleation [Fig. 22(h)], an Al layer (grown at LT) was inserted at the midpoint of an AlGaN/AlN DBR structure. All of these advanced UV-nitride DBRs were highly reflective at sub-280-nm wavelength. However, the stopbands were considered narrow ranging from 9 to 16 nm.

To overcome the lattice-mismatch and strain limitations in the UV-nitride DBRs, nearly lattice-matched DBRs using AlInN/AlGaN material system have been demonstrated (summarized in Table 8) as an alternative approach. Figures 23(a) and 23(b) exhibit a UV-A and UV-B lattice-matched nitride DBRs with a peak reflectivity at 361- and 246-nm wavelength, respectively. A wider DBR stopband (18 to 20 nm) was obtained for AlInN/AlGaN DBR compared with GaN/AlGaN DBR due to higher RI contrast. Although crack-free DBRs can be realized using a lattice-matched material system, the AlInN/AlGaN-based DBRs faced complexity during the growth due to the needs of numerous temperature ramping processes (thus resulting in long growth time) and inhomogeneity of In atoms distribution at such growth temperature.[155] Furthermore, all of the AlInN/AlGaN-based UV-DBRs can only be grown on AlGaN or AlN templates due to the large built-up strain in the case of GaN templates.

Recently, a technique using nitride-porous, i.e., a combination of epitaxial growth and chemically wet-etching resulting in AlGaN/air, was reported for UV-nitride DBRs. In Fig. 24(a), the cross-sectional SEM image shows the alternating AlGaN epilayer (high RI layer) and porous structure (low RI layer) formed after the etching process. The reflectivity of the AlGaN/porous

Table 8 Examples of UV-nitride DBRs utilizing lattice-matched material combination.

Material system	Number of period	Reflectivity (%)	Center wavelength (nm)	Stopband (nm)	Remark	Ref.
$Al_{0.85}In_{0.15}N/Al_{0.2}Ga_{0.8}N$ on AlGaN template	45	99.0	368 (UVA)	18	Mirror only	156
$Al_{0.85}In_{0.15}N/Al_{0.2}Ga_{0.8}N$ on AlGaN template	35	99.0	361 (UVA)	18	Mirror only	157
$Al_{0.85}In_{0.15}N/Al_{0.2}Ga_{0.8}N$ on AlGaN template	35	99.5	343 (UVA)	20	Mirror only	158
$Al_{0.98}In_{0.02}N/Al_{0.77}Ga_{0.23}N$ on AlN template	13.5	83.9	246 (UVC)	18	Mirror only	159
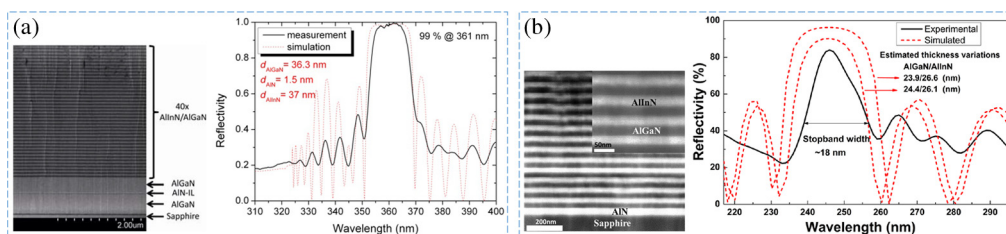
Fig. 23 Examples of lattice-matched UV-nitride DBRs using AlInN/AlGaN material system showing (a) peak reflectivity at 361-nm wavelength, reproduced with permission from Ref. 157, and (b) peak reflectivity at 246-nm wavelength, reproduced with permission from Ref. 159.
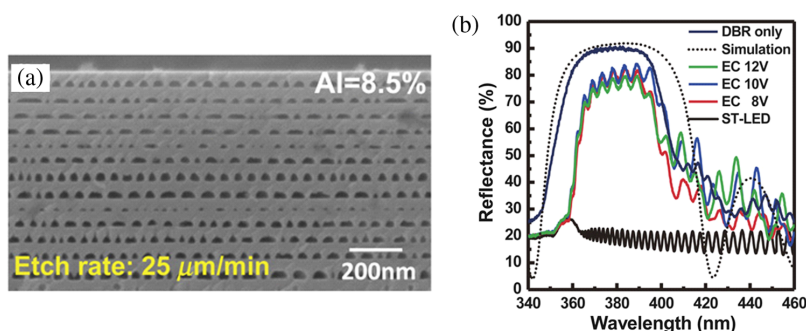
Fig. 24 Demonstration of nitride/porous UV-DBR showing (a) alternating AlGaN epilayer and the porous structure and (b) reflectance spectra of the DBR. Reproduced with permission from Ref. 135.

DBR was measure to be as high as 90% with a peak wavelength of 379 nm as shown in Fig. 24(b). A wide DBR stopband of ~37.2 nm is achieved because of the higher RI contrast of nitride and air. The high RI contrast also resulted in a highly reflective DBR by only using 12 periods of AlGaN/air. Nevertheless, there are still limitations for nitride-porous DBRs, e.g., maintaining mechanical support for the porous layer, process scalability, time-consuming etching, and realizing current injection.

4.4.2 *2-D Photonic crystals: in-plane pattern lattices*

Kashima et al.[161] reported an AlGaN-based UVC-LED emitting at 283-nm wavelength with an EQE as high as 10% using PhCs etched into the top *p*-contact as shown schematically in Fig. 25(a). The cross-sectional STEM for the PhC structure is shown in Fig. 25(b).
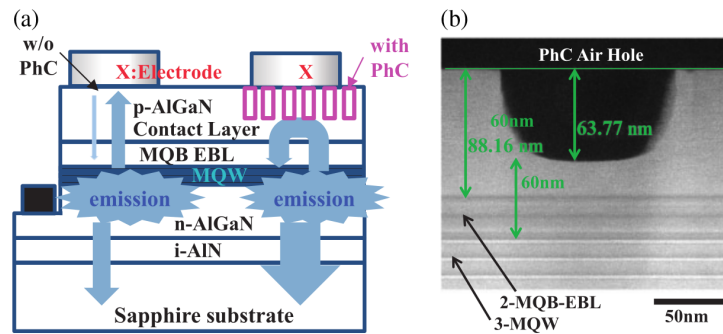
Fig. 25 (a) AlGaN UV-LED structure with and without a PhC. (b) Cross-sectional STEM image of the PhC. Reproduced with permission from Ref. 161.

Furthermore, the advantage of using PhCs to improve the device performance has been reported for AlInGaN/AlInGaN-based LEDs emitting at 333-[162] and 340-nm[163] wavelengths. An enhancement in the output power by a factor of 2.5 is found for the LED (emitting at 333 nm) with a PhC compared with the control LED without a PhC. For the UV-LED emitting

Fig. 26 (a) Top-view SEM image of the AlN PhCs waveguide cavity. (b) PL spectrum of an AlN width modulated waveguide cavity and the magnetic field amplitude profiles of the fundamental even and odd cavity modes. (c) PL of a 5-μm-diameter microdisc with AlN QDs. The insets show SEM i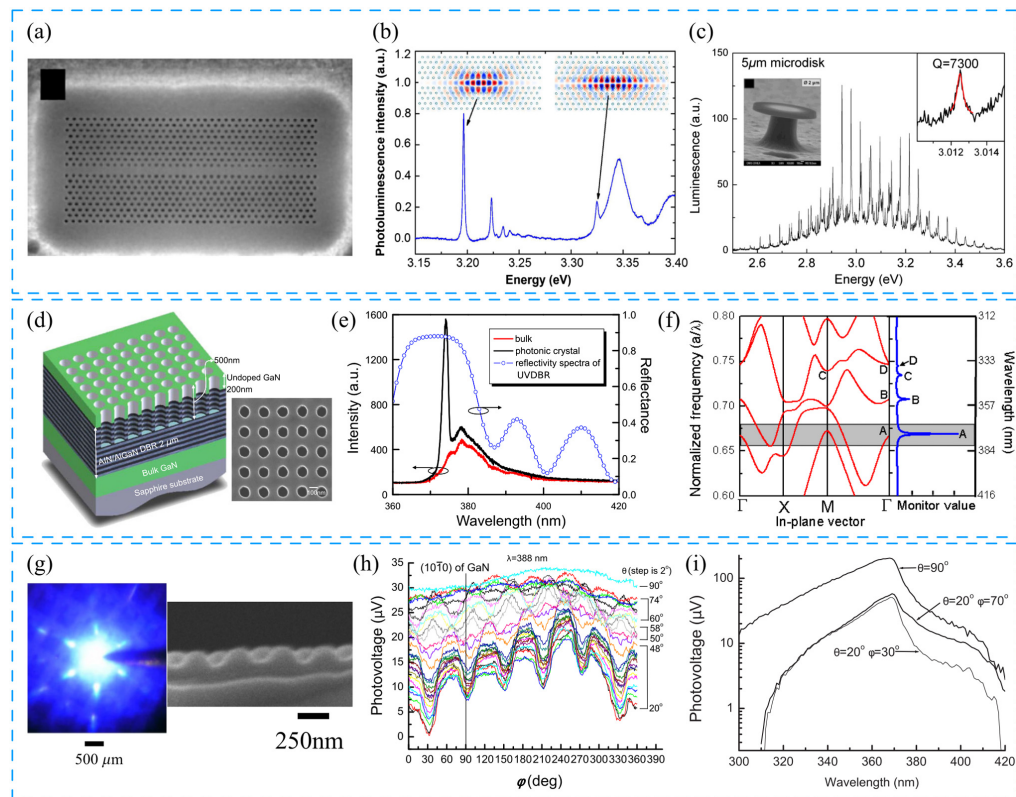mage of a 2-μm microdisc on a Si post; and a zoomed part of PL at one resonance. Reproduced with permission from Ref. 165. (d) Structure of the square PhCs lattice etched into DBR (left) and the top view SEM image (right). (e) Measured reflectivity spectrum of the AlN/AlGaN DBR structure and PL spectra of bulk GaN and patterned UV-DBR structure. Reproduced with permission from Ref. 166. (f) The corresponding band diagram and luminescence spectra (simulation). Reproduced with permission from Ref. 167. (g) Photo of LED with GaN nanostructure pattern emission (left) and SEM cross section (right). (h) Photovoltage scan at the wavelength of 388-nm versus the incidence angle θ and azimuth angle φ values. (i) Photovoltage versus wavelength at different (θ, φ) values. Reproduced with permission from Ref. 168.

at 340 nm, by integrating the PhCs into the device structure, the forward voltage decreased by ~1.6 V and the power enhanced by 95% at 20 mA.[163]

Other PhC works base their research on improving the PhC optical properties, e.g., in the case of exploring the effect of PhCs on time-resolved 333 nm UV-LED EL spectra[164] and microresonators.[165] Specifically, an in-plane PhC waveguide with a line defect is made [Fig. 26(a)]. Additionally, central holes are displaced by a maximum of 12 nm laterally, and the lattice periodicity is 170 nm. The experimental PL data are shown in Fig. 26(b) together with the mode profiles obtained by 3D-FDTD simulation, manifesting one sharp high funda-mental mode resonance in near UV and lower one in UV-A regime. Such studies and the PhCs concept can be successfully applied, for example, in AlN microdisks with embedded QDs exhib-iting a tunable resonance spectrum consisting of numerous modes, highlighting the high-quality Q factors [Fig. 26(c)]. PhCs also have been successfully implemented in devices for the use as PDs.[168] Figure 26(g) shows a PD/LED emission with hexagonal beam pattern due to the hex-agonal lattice pattern PhC on top of the device. It is capable of sensing the absolute photovoltage (PV), and it is revealed that PV strongly depends on the device orientation with respect to the detected beam's direction, i.e., on the incidence angle θ and azimuth angle φ, as seen in Fig. 26(h). There we can see the sixfold periodic pattern as φ rotates a full circle, as is suspected due to the hexagonal type symmetry of the PhC that couples the light into PD layers. Last, the responsivity curves versus wavelength at different angles are shown in Fig. 26(i), showcasing the capability of PV difference sense. Thus, one of the possible applications of this PD includes orientation/direction-aware and localization (as in positioning) solutions.

4.4.3 *3-D Photonic crystals: hybrid structures*

Figure 26(d) shows an example of 3-D PhC on the GaN-based sample for UV regime.[166,167] Although this may not be considered a true general 3-D case, it is a hybrid structure consisting of a PhC partially etched through an AlN/AlGaN DBR. It establishes complex light-structure interaction that depends at a minimum on three orthogonal spatial degrees of freedom, thus 3-D. As can be seen from the results [Fig. 26(e)], the PL signal is greatly enhanced. The PL enhancement is 5 times compared with DBR without the PhC. The peak wavelength of this structure is 374 nm—inside the stopband of DBR. The UV-DBR helps to eliminate resonant modes outside the DBR high reflection region, which in turn decreases energy waste. The simulated luminescence spectrum [Fig. 26(f)] confirms the experimental resonant peak with high accuracy. Table 9 summarizes the reported UV devices utilizing 2-D or 3-D PhCs. The table compares typical device structure, working wavelength, and a general enhancement factor.

4.5 *Nanogratings*

Nanogratings (NGs), when properly implemented on a surface of a light-emitting device, is a way to improve the LEE. Alias et al.[172] demonstrated NGs for UV-LED as NWs gratings around the device lateral configuration as shown in Fig. 27(a). The NWs gratings were patterned using gas-assisted FIB (GAFIB) etching with I_2 halide gaseous precursor. The GAFIB etching can enhance etching, reduce surface damage, and decrease the redeposition effect.[173,174] Figure 27(b) shows a substantial increase in the LOP detected from the top. Figure 27(c) shows the calculated intensity pattern of the devices with and without DBR NGs.

4.5.1 *Subwavelength gratings*

Subwavelength gratings (SWGs) are not only applied to enhance the light output, but also to control the polarizing properties. Although SWGs support only zeroth-order diffraction, they still exhibit polarization dependence. When an SWG is designed as a polarizer, one often targets to achieve high polarization selectivity: ideally, one polarization component is completely cut-off, and the other one is diffracted with 100% efficiency. The Ge SWG polarizer that is shown in Fig. 28(a) is fabricated with extinction ratio (ER) of 15 to 17.4 dB in UV-A range with a low aspect ratio (AR).[175]

Table 9 Summary of UV-photonic devices with 2-D/3-D PhCs approaches.

| Technique	Device	Device structure (top-down)	Device characteristic	Enhancement	Ref.
2-D PhCs	UV-C LED (MOVPE)	PhCs p-AlGaN 90 nm ($a \sim 250$ nm $r/a = 0.2$ $h = 64$ nm) MQW 3× AlGaN: 1.5/7 nm	Emitting at 283 nm (electrical pumping) IQE $\sim 50\%$ to 60%	~23% to 25% (EQE)	161
	NUV-LED (MOCVD)	SiO_2 PhCs ~900 nm ($d = 600$ nm $r/a = 0.35$ $h = 100$ nm) MQW 10× InGaN/GaN	Emitting at ~398 nm (electrical pumping)	27.7% (EL) at 20 mA	169
	UV-A LED (MOCVD)	PhCs p-GaN 150 nm ($a = 600$ nm $r/a \approx 0.17$ $h \sim 185$ nm) MQW 2× AlInGaN: 2.5/2.5 nm	Emitting at 333 nm (electrical pumping)	2.5× (EL) at 20 mA	162, 170
	UV-A LED (MOCVD)	PhCs p-GaN 200 nm ($a = 700$ nm $r/a \approx 0.21$ $h \sim 200$ nm) QW AlInGaN: 2/3 nm	Emitting at 340 nm (electrical pumping)	95% (EL) at 20 mA	162, 163
	UV-B LED (MOCVD)	PhCs p-GaN ($a = 500$ nm $r/a = 0.3$) [see the above two structures]	Emitting at 299 nm (electrical pumping)	2.9× (EL)	162, 171
	UV-A p-n PD/LED (MOCVD)	PhCs p-GaN 110 nm ($a = 300$ nm $r/a = 0.25$ $h \sim 100$ nm) QW InGaN 2 nm	LED emission at 433 nm	22× at 388 nm for 20 deg incidence and 255 deg in-plane angle	168
	—	AlN modified waveguide 35 nm ($a = 170$ nm $r/a = 0.27$ $h = 75$ nm) GaN QDs	Resonance tunable by a and r/a down to 290 nm	Fundamental mode PL resonance at 388 and 373 nm	165
3-D PhCs	— (MOCVD)	PhCs u-GaN 200 nm ($a = 250$ nm $r/a = 0.28$ $h \sim 500$ nm) DBR 25 pairs AlGaN: 45/42 nm	DBR reflectivity 85% stop-band width 15 nm at 375 nm	5× (PL) compared to DBR without PhCs	166, 167

Works by Weber et al. show feasibility of efficient wire grid polarizers (WGPs) in UV-B and UV-C regimes.[176,177,179,180] They have reported different material grating structures, e.g., Ir,[177] Si,[180] and Al[176,179,180] gratings down to 250 nm and W[179] grating down to 193-nm wavelength, as seen in Fig. 28(b) with given examples in SEM images of Ir structures on polymer gratings [Fig. 28(c)]. Reference 178 shows insights into WGP design using material complex RI analysis and optical simulations presents TiO_2 as a better alternative [Fig. 28(d)] to W and Ir polarizers for UV-C range. The TiO_2-based WGP showed a superior ER of 384 (25.8 dB) and transmittance of 10% at 193 nm as shown in Fig. 28(e). Another work investigates Cr_2O_3 SWGs as WGPs further in depth for UV-C with a grating period equal to ~90 nm and measured ER of 138 (21.4 dB).[181] The performance was compared with Al_2O_3, Ta_2O_5, TiO_2, and Al gratings at 193 nm. The Cr_2O_3 grating showed the highest absorption thus suppressing the TE mode the most while having practically the same transmission as the other materials. Reference 182 by numerical simulation considered AlGaN UV-A LED enhancement and fabricated a structure with a simple Si SWG on top of the LED that resulted in ER of ~16 and increase in TM polarized EL intensity by ~20%. The same author also reported in Ref. 183 a reverse ER, i.e., s/p ratio of ~4 at 360-nm wavelength, but by etching the top contact to form a grating structure.
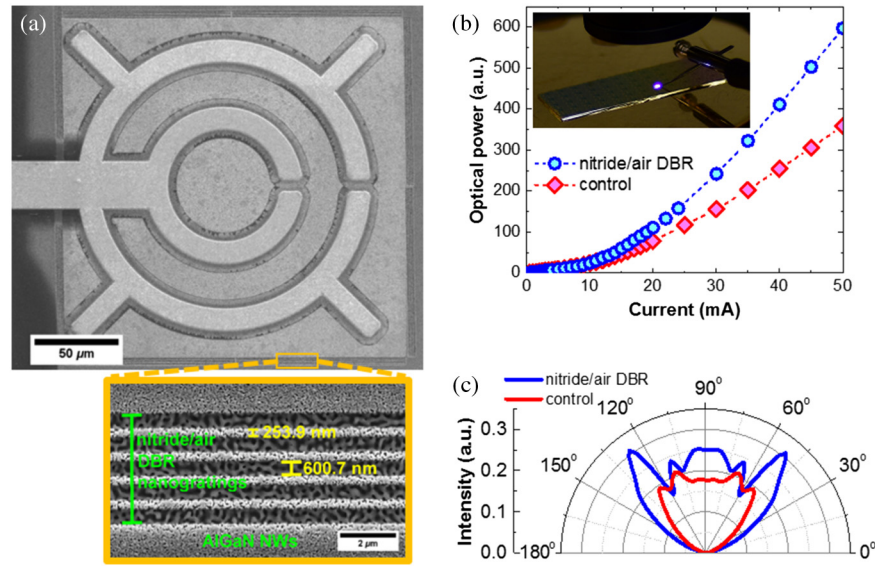
Fig. 27 (a) The top view SEM of the AlGaN NWs LED; the outset: the DBR NGs patterned at all edges of the device showing the dimension measurements of the NGs. (b) The device L–I curve characteristics comparison between the LED with and without DBR NGs (the inset: device with NGs under electrical current injection). (c) Comparison of the calculated polar pattern for both devices. Reproduced with permission from Ref. 172.
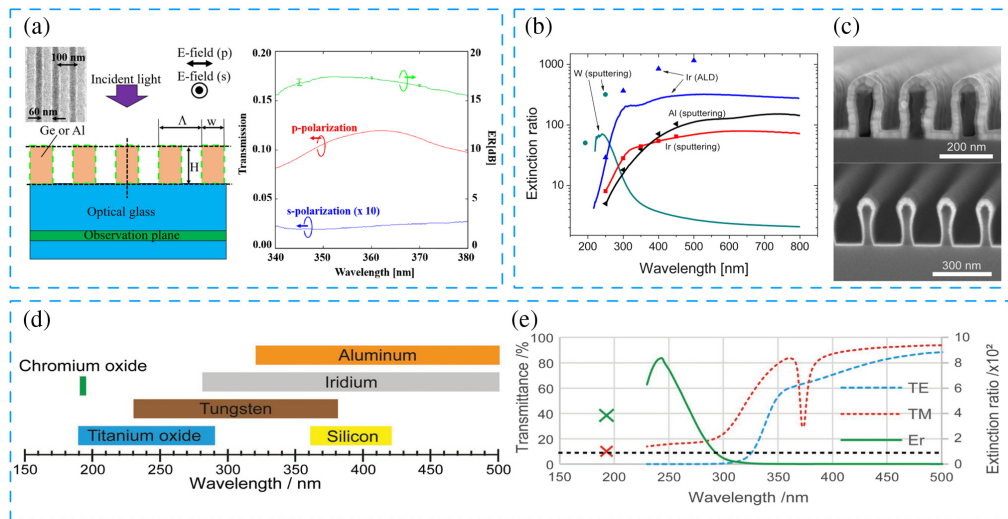
Fig. 28 (a) Schematic of the SWG with top-view SEM image of the fabricated Ge-SWG and the measured transmission and ER of the Ge-SWG. Reproduced with permission from Ref. 175. (b) Measured values of the ER of WGPs. Reproduced with permission from Ref. 176. (c) SEM images of the fabrication process for the WGPs with the overcoated polymer gratings by ALD (top) and by sputter deposition (bottom). Reproduced with permission from Ref. 177. (d) Comparison of application wavelength ranges of several WGPs from various metals and oxides. (e) Measured transmittances and ER of the fabricated titanium dioxide WGP. Reproduced with permission from Ref. 178.

4.5.2 Other devices and applications

Recent work demonstrates homogenous NG fabrication by exciting SP polaritons (SPPs) with 266-nm UV fs pulses thus allowing a formation of gratings with a wavelength-dependent period smaller than half of the excitation wavelength, showcasing another possibility of fabricating
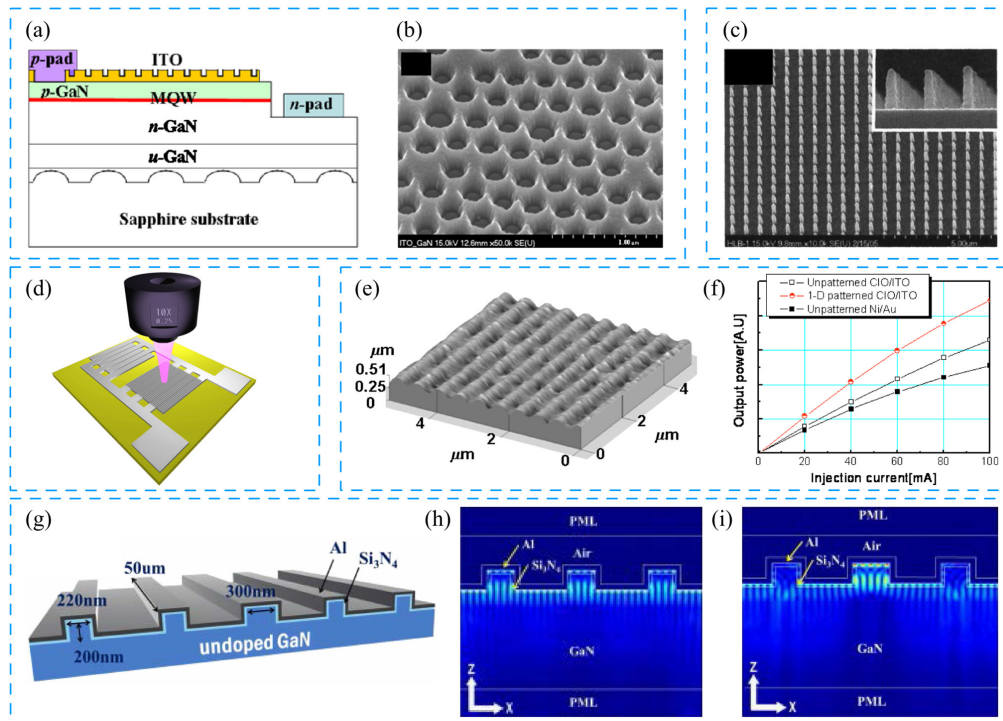
Fig. 29 (a) Schematic of an LED structure with a patterned ITO contact layer. (b) 45-deg tilt SEM image of the hole patterned p-GaN layer. Reproduced with permission from Ref. 186. (c) SEM image of 2-D patterned photoresist, the inset shows enlarged cross-section image. Reproduced with permission from Ref. 187. (d) Drawing of nanostructured MSM PD. Reproduced with permission from Ref. 188. (e) AFM image of 1-D patterned ITO. (f) The L–I characteristics of LEDs fabricated with unpatterned CIO/ITO, 1-D patterned CIO/ITO, and conventional Ni/Au contacts. Reproduced with permission from Ref. 189. (g) Schematic of the metal-coated GaN grating structure with defect cavity. (h–i) Simulated electric-field intensity in the metal-coated GaN grating (h) without and (i) with the defect cavity. Reproduced with permission from Ref. 185.

SWGs.[184] This team managed to achieve gratings with around 50- to 60-nm period lengths. Another work[185] uses SPPs phenomenon to reduce PL threshold by 75% for lasing in GaN by introducing a defect as a cavity in patterned GaN NG structure with a coated 50-nm Al metal layer [Figs. 29(g)–29(i)]. Although a simpler approach to improving LEE of UV-LEDs is contact patterning in a regular structure like a grating demonstrated in Refs. 189 and 190 [Figs. 29(e)–29(f)]. Other grating patterns, e.g., hexagonal hole pattern and square pattern gratings, were used by Kim et al.[186] and Leem et al.,[187] respectively, as seen in Figs. 29(a)–29(c).

Large-area soft UV-curing NIL fabrication of NRs for PL enhancement up to 2.5 times was demonstrated in Ref. 191 that can benefit optoelectronic applications.[192] Yet other unmentioned devices are UV PDs as demonstrated in Ref. 188 [Fig. 29(d)], where an Al metal grating with a slit width of 100 nm was employed to increase the photocurrent by 8 times at 322-nm illumination and at the same time achieving faster response and decay time of the PD.

The nanograting structures in this section are summarized in Table 10. The table compares typical device structure, working wavelength, and a general enhancement factor.

4.6 Microdisks and Nanopillars

Another approach that has been suggested for the development of III-nitride-based UV emitting devices is the use of microdisks and nanopillars. Similar to the previously described NGs and PhCs, microdisks and nanopillars provide a resonant cavity for the light to be confined and amplified. Moreover, both the microdisks and nanopillars act as a micro- and nanoscale

Table 10 Summary of III-nitrides UV-photonic devices with NGs approaches.

Technique	Device	Device structure (top-down)	Device characteristic	Enhancement	Ref.
Lateral DBR	UV-A NW LED (MBE)	Etched DBR around LED ($d \approx 850$ $h \sim 380$ $w \sim 250$) nm MQW AlGaN: 1/3.5 nm	Emitting at ~343 nm (electrical pumping)	~59% to 69% (EQE) FWHM ~15 → 12 nm	172
SWG polarizer	UV-A LED (MOCVD)	Si SWG ($d = 205$ $h = 90$ $w = 100$) nm QW AlGaN/GaN	Emitting at 370 nm (electrical pumping) AR = 0.9	~20% (TM EL) ER ~ 12 dB (16×) at 370 nm	182
	UV-A LED (MOCVD)	Patterned p-GaN 100 nm ($d = 200$ $h = 150$ $w = 140$) nm MQW AlInGaN/AlGaN	Emitting at 365 nm (electrical pumping) AR = 1.07	ER^{-1} (s/p) ~6 dB (4×) at 360 nm	183
	—	a-Si grating ($d = 140$ $h = 80$ $w = 42$) nm Fused silica substrate	AR = 1.90	ER = 19.5 dB (90×) w/T = 42% at 365 nm	180
	—	Ge grating ($d = 100$ $h = 100$ $w = 60$) nm Optical glass	AR = 1.67	ER = 17.4 dB (55×) w/T = 12% at 360 nm	175
	—	Ir grating ($d = 100$ $h = 150$ $w = 30$) nm Fused silica substrate	AR = 5	ER = 19.4 dB (87×) w/T = 45% at 250 nm	177, 176
	—	W grating ($d = 100$ $h = 150$ $w = 30$) nm Fused silica substrate	AR = 5	ER = 22 dB (158×) w/T = 40% at 193 nm	179, 176
	—	Two Cr_2O_3 gratings ($d \sim 90$ $h \sim 120$ $w \sim 36$) nm Quartz substrate	AR ~ 3.3	ER = 21.4 dB (138×) w/T = 18.6% at 193 nm	181
	—	TiO_2 grating ($d = 104.5$ $h = 150$ $w = 26$) nm Fused silica substrate	AR = 5.77	ER = 25.8 dB (384×) w/T = 10% at 193 nm	178
SW feature	UV-B MSM PD (MOCVD)	Al metal grating ($d = 314$ $h = 35$ $w \approx 105$) nm with 100 nm slit; u-GaN 1 μm	Dark current <1 pA up to 7 V bias V(breakdown) ~15 V	8× (photocurrent) at 322 nm	188
Patterned top contact	NUV-LED (MOCVD)	CIO/ITO grating ($d \sim 500$ $h = 100$) nm MQW InGaN/GaN	Emitting at 398 nm (electrical pumping)	33% (EL) w/1-D and 48% w/2-D nanopattern	190
	UV-A LED (MOCVD)	CIO/ITO grating ($d \sim 500$ $h = 100$ $w \sim 250$) nm MQW InGaN/GaN	Emitting at 385 nm (electrical pumping)	40% (EL) with 1-D nanopattern	189
GaN nanorods	—	GaN Sapphire	PL at ~450 nm	~2.5× (PL) compared to GaN films structure	191
Metal-coated GaN defect grating	— (MOCVD)	50 nm Al metal layer, grating ($d = 840$ $w = 220$ $h = 200$) nm, u-GaN 2 μm	l(cavity) = 300 nm RT PL lasing at 365 nm	Q = 480 and reduced threshold power density by 75%	185

light source, thus becoming a promising approach for applications in UV micro- and nanophotonics. In 2003, Jiang and Lin[193] reviewed III-nitride microemitters, then in 2014, Néel et al.[165] briefly reviewed AlN microdisks, and in 2015, Zhang et al.[194] reviewed III-nitride microdisk lasers over the UV and visible spectrum. Here, we provide a historical context of a broad set of microdisks and nanopillars structures focusing exclusively on III-nitride UV emitters fabricated by a top-down approach.

4.6.1 Microdisks

A semiconductor microdisk laser is a circular resonator cavity formed by top-down fabrication of an active material, i.e., semiconductor material or structure, where both physical and chemical etching are used to pattern the structures and release them into a mushroom-like configuration. The microdisk made from the active material is sustained on a pillar made from the substrate
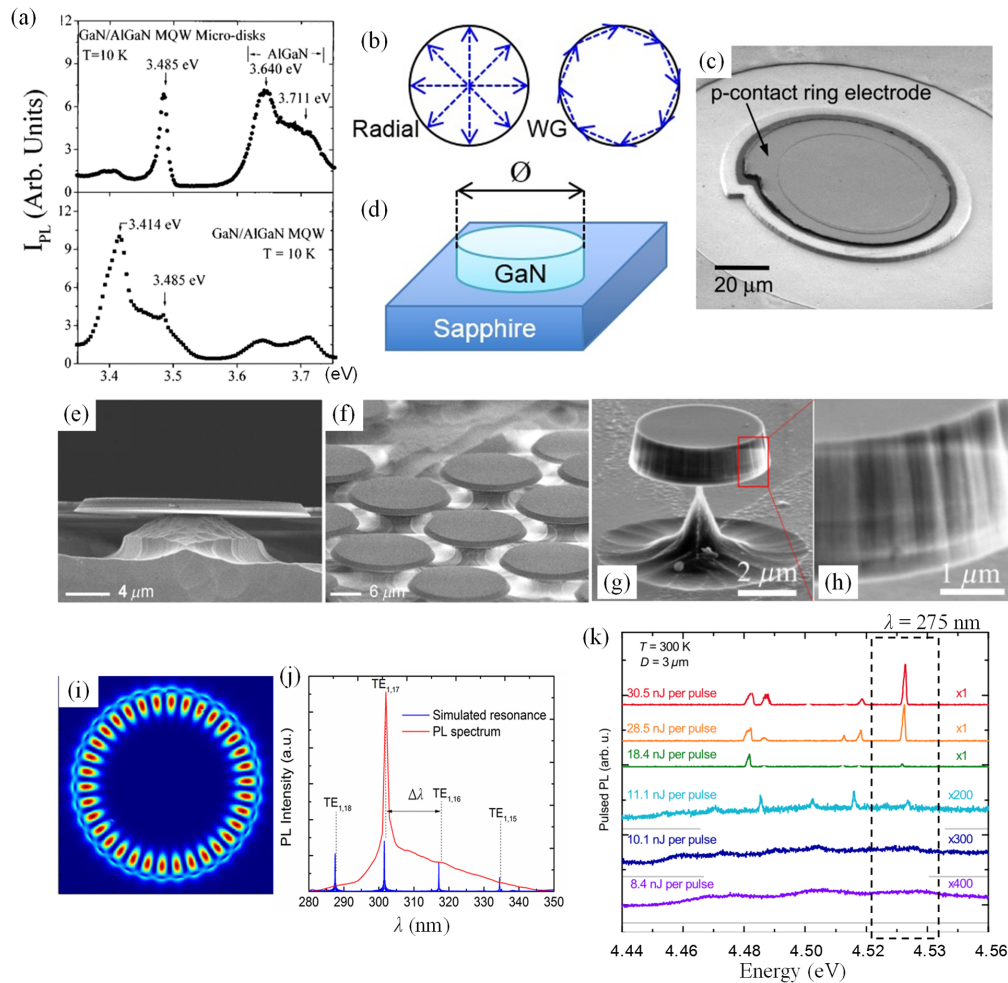
Fig. 30 The development of UV-emitting microdisks from 1997 to 2018. (a) PL spectra of GaN/AlGaN material before (bottom) and after (top) microdisk fabrication. Reproduced with permission from Ref. 195. (b) Schematic of radial and WG resonant modes in a microdisk. (c) SEM image of the electrically driven directional UV-A microdisk laser. Reproduced with permission from Ref. 196. (d) Schematic of a GaN microdisk in full contact with a sapphire substrate. (e) Lateral and (f) perspective view of freestanding InGaN/GaN-based microdisks on Si substrate. Reproduced with permission from Ref. 197. (g) GaN microdisk on Si post with detail (h) of edge NGs. Reproduced with permission from Ref. 198. (i) FDTD-simulated electric field intensity of a $\lambda = 301$ nm WG mode as well as the mode matching with the corresponding PL emission (j). Reproduced with permission from Ref. 199. (k) PL emission of a 3-μm microdisk at different pulse-injection intensities showing lasing at $\lambda \sim 275$ nm. Reproduced with permission from Ref. 200.

material [Figs. 30(e)–30(g)]. Microdisks can also be realized in full contact with the substrate [Figs. 30(c) and 30(d)]. Here, we present and discuss the experimental demonstrations and historical progress toward UV microlasers based on microdisk structures.

The first top-down attempt to realize microdisks of GaN/AlGaN MQW was the work of Mair et al.[195] Employing pulsed optical pumping under LT condition (10 K), they were able to compare the PL (continuous and time-dependent) of the GaN/AlGaN material before and after microdisk fabrication [Fig. 30(a)]. This study showed that the recombination lifetime and the quantum efficiency (QE) of the GaN/AlGaN intrinsic transitions, were improved by a factor of 10 after the formation of the microdisks. Additionally, the contribution of the impurity transition of misfit dislocations was drastically reduced. These findings confirmed the influence of microdisks structure on the light emitting properties of GaN-based materials and set from that moment a path for the further investigation of such structures. Using the same material system, the same workgroup was able to observe, for the first time, the formation of UV-A radial modes at room temperature and whispering-gallery (WG) modes at 10 K.[201] The first UV-A microdisk pulsed-laser was achieved by Chang et al.[202] demonstrating the first lasing WG features using a GaN microdisk as well as a decrease in the stimulated emission threshold by 10 times as compared with a GaN squared-shaped structure.

The development of the UV microdisk lasers increased in complexity, including studies on the optical pumping geometry,[203] directional lasing emissions,[196,204,205] electrical injections,[196] foreign substrates,[197–200,206–211] different crystal planes,[208–210] quantum structures,[200,206–211] and on new material systems, such as GaN/AlN and AlN/AlGaN.[199,200,208–211] During this technological progress, smaller lasing thresholds and single-mode lasing were achieved, room temperature operation became the standard, and a UV-C lasing emission [center wavelength (λ_c) = 275 nm] became a reality.[200,211] Nonetheless, this progress comes with trade-off between different device parameters i.e., the first UV-C microdisk laser required a high pumping energy of 17,000 kW/cm^2, whereas the most recent UV-A single mode microdisk laser emitting at 379.25-nm wavelength needs only 225 kW/cm^2. In Table 11, we illustrate comprehensive historical progress of these III-nitrides-based microdisks UV emitters.

In addition to efforts mentioned above, Kneissl et al.[196] demonstrated electrical injection of a spiral-shaped microdisk [Fig. 30(c)] on an InGaAlN laser heterostructure, obtaining a room-temperature directional radial/WG-multimode lasing at 399 nm. So far, this is the only work of an electrically pumped microdisk laser with an emission wavelength in the UV spectral range below 400 nm. Choi et al.[197] demonstrated the first freestanding InGaN/GaN microdisks on Si by selectively dry-etching the substrate [Figs. 30(e) and 30(f)]. This enabled a bottom GaN/air interface instead of GaN/Si interface, creating strain relaxation and improved material properties. Such a microdisk showed WG lasing emission at ~365 nm at a 4.3-K temperature and laid the demonstration of III-nitrides on Si platform. Next, Zhang et al.[199] demonstrated a material system (AlN/AlGaN-on-Si) obtaining a single-mode lasing in the UV-B spectral range, being the only report of microdisks in such material system till now. Additionally, they study the structure by FDTD simulation of the WG resonant modes [Figs. 30(i) and 30(j)], obtaining mode matching between the experimental and the simulated results. Mexis et al.[207] and Bürger et al.[209] also demonstrated a mature computational approach to study the microdisk UV lasers.

One of the most recent report on microdisk lasers by Zhu et al.[198] illustrates a concept of spontaneous formation of a sidewall grating [Figs. 30(g) and 30(h)], which enables the single-mode lasing at 379 nm of a GaN microdisk on Si substrate. Ultimately, it is important to highlight the work of Sellés et al.,[200,211] holding the record for the shortest wavelength III-nitrides microdisk laser of 275 nm [Fig. 30(k)]. This was achieved by integrating ultra-thin GaN/AlN MQW (0.7/5 nm) on Si. As both GaN and AlN are binary compounds, the quality of the material is not compromised as compared with alloyed materials, e.g., ternary compounds, e.g., AlGaN and InGaN.

4.6.2 Nanopillars and nanowires

Similarly to microdisks, nanopillars and NWs are structures with the potential to function as a lasing element in the UV spectral range. As seen in Table 12, the lasing of such structures has been achieved in a variety of pillar/wire dimensions and configurations.

Table 11 Historical progress in III-nitrides-based microdisk for UV photonics.

Material system	Wavelength, λ (nm)		Diam. (∅) (μm)	Temp.	Q-factor	Remark	Lasing threshold	Year	Ref.
GaN/AlGaN	334, 341, 356	UV-A	~9	10 K	—	10× improved QE	—	1997	195
GaN/AlGaN InGaN/GaN	360 379, 382, 391	UV-A	9	RT 10 K	>GaAs	Observation of WG and radial modes	—	1998	201
GaN	375	UV-A	250, 50	RT	—	10× lower lasing threshold, WG modes	200 kW/cm²	1999	202
GaN	364, 375	UV-A	500	—	—	Spatially selective optical pumping	60 kW/cm²	1999	203
GaN	~379	UV-A	~100, ε = 0.2	—	—	First directional SE, quadrupole disk (elliptical), bow-tie modes	5000 kW/cm²	1999 2000	204 205
InGaN/GaN/AlGaN	398.5	UV-A	~100 (ro = 50, ε = 0.15)	RT	—	Elec. injection, spiral microdisk, directional laser, WG, and radial modes	~ ×10⁵ kA/cm²	2004	196
InGaN/GaN	~365	UV-A	20	4.3 K	80	WG modes, lasing III–N on Si substrate	—	2006	197
GaN/AlN/AlGaN	377 379	UV-A	4.7	—	400 320	Bottom DBR (R = 85%), WG modes	0.03 kW/cm², 0.043 kW/cm²	2010	137
GaN/AlGaN	~394 346, 355, 364	UV-A	6 2, 5	4 K RT	2000 <1450	GaN quantum dots, well defined WG modes, III–N on Si substrate	<0.06 kW/cm²	2010 2011	206 207
c-GaN/c-AlN GaN	349, 354 347, 349 340 311, 318	UV-A UV-B	2.5 2.6 4 2.5	11 K 7 K 7 K ~10 K	400 600, 440 1400 5000	Cubic/zinc-blende quantum dots, III–N on 3C-SiC/Si substrate, WG modes	— — 20 to 30 kW/cm²	2013	208 209 210
GaN/AlGaN	275	UV-C	3	RT	—	First UVC microlaser at RT. IQE 80% (pulsed pumping), Si substrate	17,000 kW/cm²	2016	200

Table 11 (*Continued*).

| Material system	Wavelength, λ (nm)		Diam. ($\varnothing$) (μm)	Temp.	Q-factor	Remark	Lasing threshold	Year	Ref.
GaN/AlGaN	275	UV-C	3	RT	4000	Si substrate, CW versus pulsed pumping, WG modes	15 mJ/cm^2	2016	211
AlN/AlGaN	~300	UV-B	1	RT	~300	Single mode laser, Si substrate	24.2 mJ/cm^2	2017	199
GaN	379.25	UV-A	4.9	RT	~1270	Single mode laser, sidewall roughness as grating, Si substrate	225 kW/cm^2	2018	198
AlN/AlGaN	~250	UV-C	7	RT	500 to 1000	Shortest wavelength reported, WG modes, Si substrate, no lasing	—	2018	212

Table 12 III-nitrides-based top-dow-etched nanopillars and nanowires for UV nanophotonics.

Material system	Wavelength (nm)		Diameter, $\varnothing$ (μm)	Length, L (μm)	Temp.	Remark	Lasing threshold	Year	Ref.
AlInGaN/ AlGaN	344	UV-A	0.50	1.00	RT	III–N bottom DBR, SiO_2/HfO_2 top DBR, $Q = 160$	520 kW/cm^2	2010	213
InGaN/ GaN	373	UV-A	0.98	0.75	RT	Al-coated, single WG mode lasing, $Q = 150$	420 kW/cm^2	2012	214
GaN	371	UV-A	0.14	4.70	RT	Freestanding NW on SiN film substrate, FP single mode lasing	231 kW/cm^2	2012	215
GaN	370	UV-A	0.68 0.72	7.60 8.00	—	Single mode lasing by Vernier effect coupled cavity	874 kW/cm^2	2012	216
GaN	369	UV-A	0.35	5.30	—	Single mode lasing by Au/SiN film substrate mode losses	276 kW/cm^2	2012	217
GaN	363, 364, 365	UV-A	0.30	1.20	RT	Al/SiN-coated, WG-SP and cavity modes, $Q \sim 120$	5.2 mJ/cm^2	2013	218
GaN	369	UV-A	~0.20	5.00	—	Single mode by external SiN 90 nm DFG	~300 kW/cm^2	2014	219

A team composed of Li, Xu, Wright et al. utilizing a combination of dry-etching and anisotropic wet etching processes fabricated a set of GaN NWs [Figs. 31(c) and 31(d)].[215–217,219] These NWs were then isolated and used in several configurations to demonstrate UV-A lasing. First, a single NW ($\varnothing = 0.14$ μm, $L = 4.7$ μm) was investigated under optical pumping at room temperature. After the pumping threshold, a single-mode lasing at 371-nm wavelength was emitted from the longitudinal facets produced by the Fabry–Perot (FP) oscillations along the wire. Moreover, by setting two discrete GaN NWs one besides the other, a coupled cavity was created with single-mode lasing at $\lambda_c = 370$ nm [Figs. 31(a), 31(b), and 31(e)]. The lasing emission from such a coupled cavity is associated with the Vernier effect, i.e., suppression of resonant modes due to destructive interference.[220]

Due to the nature of this coupling effect, the lasing threshold was increased to 874 kW/cm^2; this is about three times higher than the lasing threshold of a single NW. Similarly, a single mode lasing in a discrete GaN NW ($\varnothing = 0.35$ μm, $L = 5.3$ μm) was achieved by a method of mode-selection based on the UV ohmic loss of the GaN-NW/Au interface. By modeling and calculating the propagation loss of different resonant modes within the NW cavity in contact with the metal, a specific mode (the one with less exposure to the NW/metal interface) is found to experience a loss significantly lower than any other optical mode and to be low enough to be overcome by the modal gain. It was quantified that using this method, the lasing threshold increases only by 13%, reporting a threshold value of 276 kW/cm^2. Ultimately, a GaN NW ($\varnothing = 0.2$ μm, $L = 5.0$ μm) of the same nature was characterized by optical pumping while lying on a SiN NGs. It was observed that when the NW cavity is perpendicular to the grating pitch, the substrate grating works as a distributed feedback grating (DFG) enabling the single-mode lasing of the NW at a threshold power density of ~300 kW/cm^2. It is important to highlight that the diameter and length of the GaN NWs are critical parameters toward single mode emission.

The reports by Li et al.[214] and Hsu et al.[218] demonstrated the use of Al thin-film coating on nanopillars [Figs. 31(f) and 31(g)], with the goal of providing UV optical confinement in the cavity
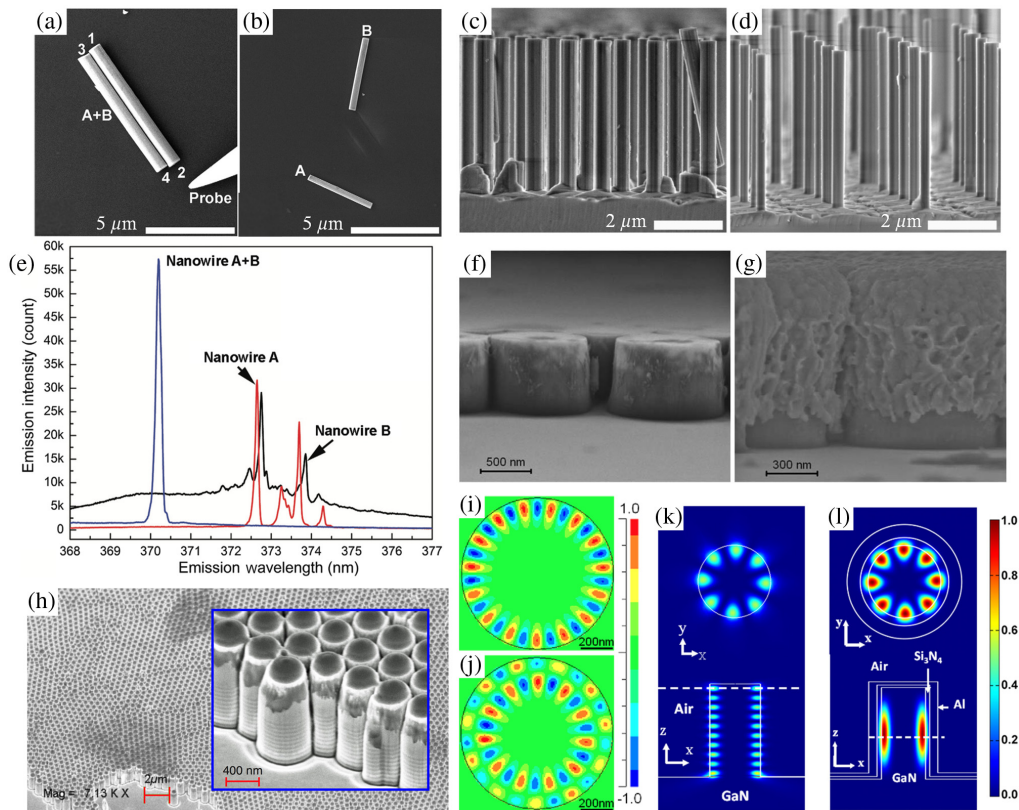
Fig. 31 Development of nanopillars and NWs as UV-light lasing structures. (a) GaN NW pair (1, 2, 3, and 4 indicate the facets) formed by NW A and NW B as seen in (b), with their corresponding lasing spectra on (e). Reproduced with permission from Ref. 216. (c) and (d) are dry-etched GaN NWs after 6 and 9 h of additional wet etching. Reproduced with permission from Ref. 215. (f) An array of InGaN/GaN nanopillars before and after (g) Al metal coating. Reproduced with permission from Ref. 214. (h) SEM image of vertical-emitting UV lasing nanopillars with the bottom and upper DBR, and the inset shows a zoom-in SEM image. Reproduced with permission from Ref. 213. (i) and (j) The FDTD-simulated electric field of the WG modes in a micropillar, showing the different radius dependence for light at 365 and 373 nm, respectively. Reproduced with permission from Ref. 214. (k) and (l) The calculated electric field distribution of a nanopillar without and with a metal mirror (Al/SiN) coating. Reproduced with permission from Ref. 218.

due to the high UV reflectivity of Al film. In Ref. 214, a WG-based single mode lasing at 373-nm wavelength is achieved at an optical pumping power density of 420 kW/cm^2. The WG nature of the lasing mode is verified through the peripheral far-field emission measurements around the set of nanopillars, relying on the fact that the single-mode WG lasing must be directional. Additionally, FDTD simulations were performed to understand the origin of the resonant peak wavelength. The emission spectra showed two resonant wavelengths for the nanopillars ($\lambda_{c1} = 365$ nm, $\lambda_{c2} = 373$ nm). The emission of the peak at 365 nm belongs to the first-order WG, which is exposed to the walls of the nanopillar being prone to losses [Fig. 31(i)]; whereas, the mode corresponding to $\lambda_{c2} = 373$ nm is a higher order WG mode and therefore it remains within the nanopillar avoiding the losses encountered by the first-order mode [Fig. 31(j)]. Hsu et al.[218] studied numerically and experimentally the role of the metal coating in maintaining the WG modes confined within the cavity. As a result of this approach, a two-fold cavity confinement enhancement is achieved as compared with the nanopillars without the metal coating [Figs. 31(k) and 31(l)]. Additionally, they demonstrated that nanopillars with sidewall angles nearer to 90 deg are preferred to improve the cavity quality. Chen et al.[213] suggested another approach by utilizing a AlInGaN-based MQW active region existing between a bottom AlGaN-based DBR and a top HfO$_2$/SiO$_2$-based DBR to create an enhanced vertical-cavity [Fig. 31(h)].

4.6.3 *Other unique micro- and nanostructures*

Additionally, to what has been discussed earlier, we have found a set of unique structures that can significantly impact the development of UV photonics. Zeng et al.[221] demonstrated the first InGaN/GaN-based microring resonator in UV-A regime. Due to the shape of these structures, radial modes are not allowed, and only WG resonant modes can be produced. This fact represents an advantage of the ring-structures when developing WG resonators. Following the microring, Wang et al.[222] demonstrated a GaN nanoring [Fig. 32(a)] enhanced by a coating of thin Al (50 nm). In this report, experimental and computational characterizations agree that the device presented hybrid WG-SP lasing modes ($\lambda_c \sim 365$ nm) created from the combination of the ring-shaped semiconductor and the evanescent fields on the semiconductor/metal interface. Although this effect is not desired for single-mode lasing devices, the nature of the plasmonic resonances opens up the possibility of using this kind of nanorings for sensing at the nanoscale.[227] The same research group fabricated a GaN nanostripe, coated with 20-nm SiO_2 and 60 nm Al [Fig. 32(b)].[223] Here, they observed lasing at $\lambda_c = 370$ nm under a relatively low optical power density threshold of 0.042 kW/cm², at room temperature. Due to the waveguide-like shape of the nanostripe, and because of the highly reflective internal walls (Al), lateral confinement exists, and an FP cavity is formed in the transversal plane.

An innovative approach is presented by Wang et al. demonstrating high Q (>6000) WG-mode lasing at room temperature in a GaN micropyramid ($\lambda_c = 367.2$ nm, lasing threshold = 400 to 500 kW/cm²).[225] These GaN pyramids are created by KOH wet etching of GaN, previously transferred onto a Ni-Ag-Pt-Au/Cu substrate. This nonconventional method allows the formation of high-quality GaN micropyramids standing on a metallic reflector [Fig. 32(d)]. Because of this configuration, the microcavity is capable of sustain "quasi-WG" lasing modes fed by the pyramid faces and the bottom mirror. Another unique microstructure was reported by Zhang et al.[224] including a very comprehensive study of the material properties, the optical cavity, the power injection, as well as the carrier dynamics. Mushroom-like structures (hemispherical microcavities) [Fig. 32(c)] were achieved in an InGaN/GaN-on-Si system showing WG lasing modes with the strongest lasing peak at $\lambda_c = 381$ nm. One benefit of such hemispherical structure is the elimination of parallel facets (like those in microdisks), ideally
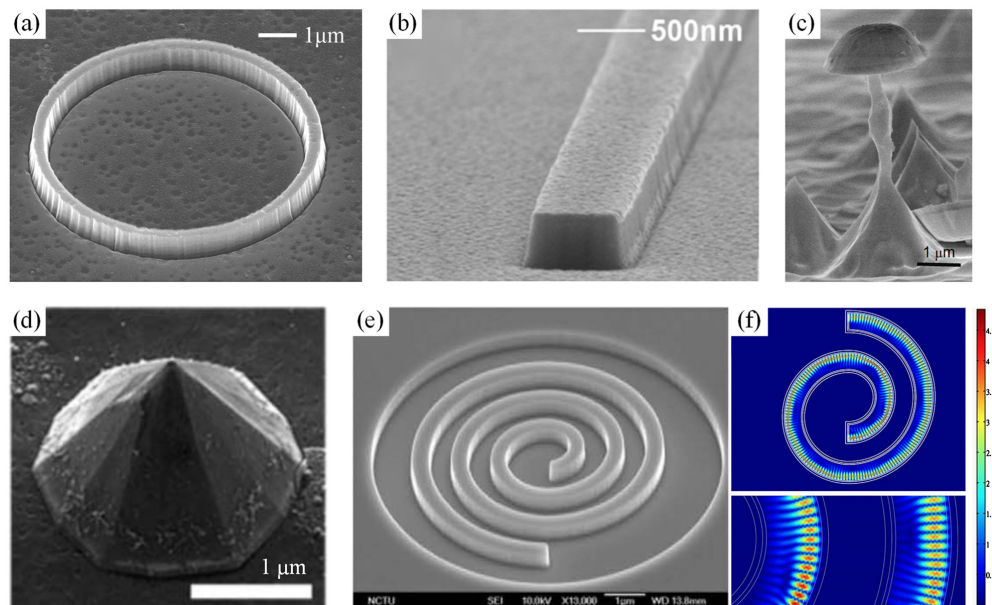
Fig. 32 Set of unique III-nitrides-based UV-lasing micro and nanostructures. (a) Metal-coated nanoring. Reproduced with permission from Ref. 222. (b) Metal-coated nanostripe. Reproduced with permission from Ref. 223. (c) Hemispherical microcavity on Si post. Reproduced with permission from Ref. 224. (d) Micropyramid on a metal substrate. Reproduced with permission from Ref. 225. (e) Metal-coated nanospiral with calculated electric field distribution (f). Reproduced with permission from Ref. 226.

removing any possibility of observing FP oscillations, creating pure WG/ radial modes. The last structure discussed is the nanospiral created by Liao et al. [Fig. 32(e)].[226] This structure is made of GaN coated with 30-nm SiN and 50-nm Al thin film. Circularly polarized UV-A lasing at $\lambda_c = 363.5$ nm was demonstrated at a low lasing threshold of 0.017 and 0.016 kW/cm^2, respectively, for left and right circular polarizations. Similar to the previous structures coated with Al, the metal significantly enhances the transversal cavity and light confinement [Fig. 32(f)]; however, in this spiral, the role of the longitudinal traveling modes along the waveguide-like structure is critical to creating polarization rotation. This polarization rotation could be generated by the minor changes of curvature along the GaN-Al interface, impinging a small phase change to the lateral confined modes. Moreover, these observations open opportunities for further research and development of nanosources of circularly polarized UV light. To the present day, this nanoscale circularly polarized UV laser, represent by itself a breakthrough in UV nanophotonics.

4.7 Surface Plasmons

SPs are the collective oscillations of free electrons at a metal–dielectric or metal–semiconductor interface, where the real part of the dielectric function changes its sign.[228] Plasmonics attributes optical technology of coupling SPs to electromagnetic waves. This merged photonic-electronic phenomenon excites propagating SPPs on planar surfaces or localized SPs (LSPs) on nanoparticles. Both of the SPPs and LPSs manifest themselves as evanescent electromagnetic waves with a penetration depth of only a few tens of nanometers in metal, at optical frequencies. The dispersion properties of SPPs and LSPs are unique as they significantly enhance the incident electromagnetic field near the metallic structures.[228,229]

SPs can boost the EQE of UV light emitters through two ways, enhancing its LEE and IQE.[230–233] In the first way, generated photons captured within the device are intentionally directed toward a metallic layer to excite SPPs on its surface.[230] The condition of this process is that the plasmonic resonance wavelength of the metal matches the wavelength of the generated light. If the metal surface is rough enough to scatter SPPs as light out of the device, the LEE of the UV emitter can soar because of extracting the SP-induced magnified light out of the emitter. The second way dramatically increases the emitter IQE through the exciton-SP coupling.[231,232] This way is contingent on placing a QW near a metallic plasmonic surface such that electron-hole pairs are located within the near field of the metallic surface. In this scenario, some electron-hole pairs recombine and directly transfer their energy to the electrons oscillations on the metal surface to produce SPs instead of photons. This new recombination path, along with the typical electron-hole recombination which generates photons, decreases the spontaneous emission lifetime, and thus enhances the emitter IQE. Here, we discuss the SPs approaches for UV-photonic devices, which include approaches of thin films, a patterned layer, metamaterial, and nanostructures.

4.7.1 Thin plasmonic film

Gao et al. followed the first way mentioned above to enhance the device performance using AlGaN-based UV-LED [Fig. 33(a)].[230] In this structure, a 5-nm-thick Al layer is deposited above the MQW structure. When electron-hole pairs recombine in AlGaN alloys, they generate photons with a dominant polarization parallel to the crystal axis ($E\|c$). Consequently, as shown in Fig. 33(a), only weak light signal of polarization $E \perp c$ can be extracted through the escaping cone. The remaining light signals (entire $E\|c$ and part of $E \perp c$ polarization) are captured within the LED and propagate parallel to the Al layer. The $E\|c$ polarization one is a TM wave for the Al layer and can excite SPPs on its surface at 294-nm wavelength. Figures 33(b) and 33(c) show the atomic force microscopy (AFM) images for the top surfaces of the UV-LED and Al layer, respectively. Figure 33(d) compares the PL of the UV-LED without Al, after depositing the Al, and after oxidizing the Al. SP-enhancement of 217% is acquired for the PL at 294-nm wavelength.

Lin et al.[231] presented an example for SP-enhanced IQE of UV emitter. A schematic of the AlGaN/GaN QW structure is shown in the inset of Fig. 33(a). The QW is fabricated using MBE and coated with Ag, Au, or Al to excite SPPs on their surfaces. The top AlGaN layer is thin enough to raise the spontaneous emission decay rate of the carriers through direct transfer of the
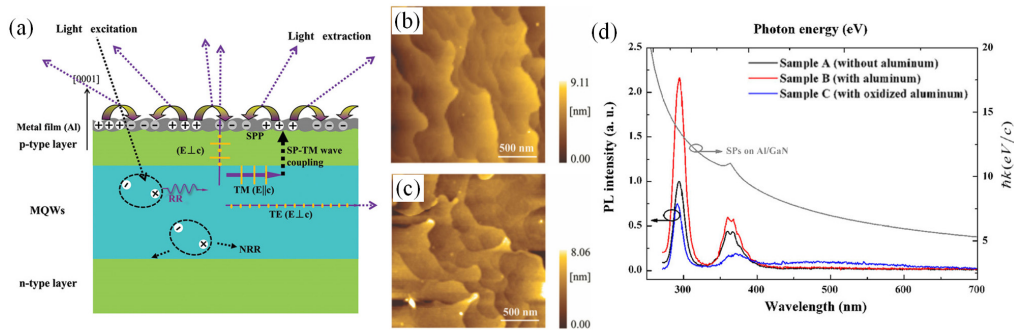
Fig. 33 (a) Schematic of the SP-enhanced AlGaN-based UV-LED. AFM images for the top surfaces of the (b) UV-LED and (c) Al layer. (d) PL spectra of the structures. Reproduced with permission from Ref. 230.
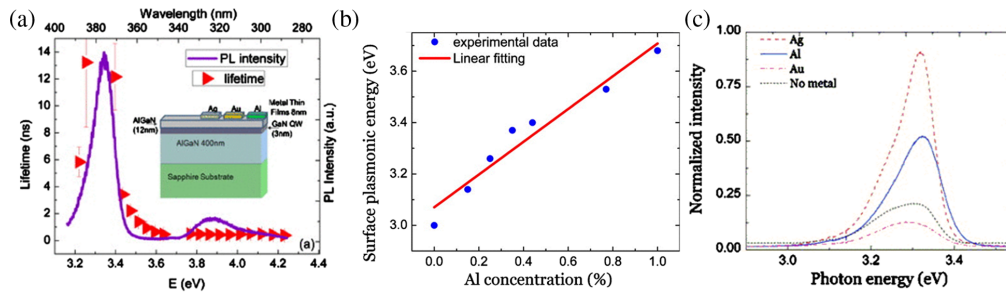
Fig. 34 (a) PL spectrum and carrier lifetime with a schematic of AlGaN/GaN QW shown in the inset. (b) Change of the SP energy of the Ag layer with Al content of the AlGaN barrier layer. (c) Comparing the PL of the metal-free AlGaN/GaN QW and with other metals. Reproduced with permission from Ref. 231.

electron-hole energies to the electrons oscillations on the metals surfaces. Before metal deposition onto the device, the PL intensity and lifetime of the carriers were measured at 10 K [Fig. 34(a)]. Interestingly, this research group discovers the ability to tune the plasmonic resonance wavelength of Ag from the visible to UV region by tuning the Al content of the AlGaN barrier [Fig. 34(b)]. When the Al content within the barrier layer is ∼23%, the Ag plasmonic resonance matches the emission wavelength of the GaN QW. In Fig. 34(c), the SP-enhancement of the PL emission from the GaN QW is compared for three different metals. A threefold increase in the UV-light emission is obtained when using Ag as a plasmonic layer.

4.7.2 Patterned plasmonic layer

Cho et al.[232] reported an SP-enhanced IQE of AlGaN-based UV-LED using a patterned plasmonic layer. The LED structure is schematically shown in Fig. 35(a). To provide an exciton-SP
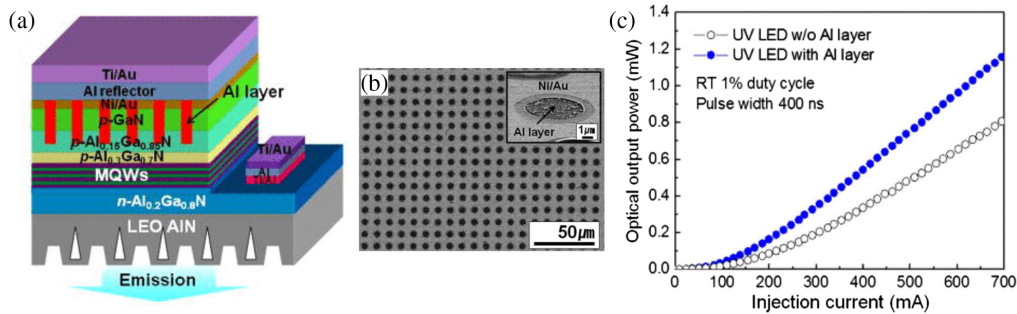
Fig. 35 (a) Schematic of the SP-enhanced UV-LED. (b) Top-view SEM image after Al deposition. (c) The output power as a function of the injection current for the LEDs with and without Al layer. Reproduced with permission from Ref. 232.

coupling, the top most p-AlGaN and p-GaN layers are patterned with vertical holes via photo-lithography and dry-etching. Afterward, Al pillars are deposited inside the holes to be in the very close vicinity to the MQW, as shown in Fig. 35(a). Figure 35(b) shows the top-view SEM image after Al deposition. Then, Al and Ti/Au layer were deposited on top of the device to work as reflectors, and thus light is extracted from the backside, as shown in Fig. 35(a). The output power of the SP-enhanced LED is 45% higher than that of the control LED [Fig. 35(c)]. This enhancement is attributed to the increase in the spontaneous emission decay rate by the exciton-SP coupling.

4.7.3 *Hyperbolic metamaterial*

An alternative approach is introduced by Shen et al.[233] to use resonant SPs modes excited within hyperbolic metamaterial (HMM) to enhance simultaneously the IQE and LEE of AlGaN-based UV-LED. In comparison with the typical SPs structures, HMM is made of multiple metal–dielectric interfaces. Excitons from MQW close to the HMM can excite its resonant SPs modes, which increase their spontaneous emission decay rate and the IQE. A significant PL enhancement by 520% is achieved for HMM-based LED in comparison with the control LED.

4.7.4 *Plasmonic nanostructures*

Son et al. investigated the influence of plasmonic nanostructures on the performance of AlGaN/GaN LED.[234] The plasmonic nanostructure used in these LEDs consists of Al nanorings, which are assembled directly above the MQW as shown in Fig. 36(a) to allow direct exciton-SP coupling. The fabrication steps of the Al nanorings are summarized in Fig. 36(b). The diameter of the nanorings can be tuned through the diameter of the silica nanospheres until their plasmonic resonance wavelength matches the emission wavelength of the LED. Figure 36(c) shows the AFM of the LED, where the Al nanorings were fabricated using 300-nm diameter silica nanospheres. The PL spectra [Fig. 36(d)] show various enhancements due to the IQE improvement from the exciton-SP coupling. Recently, Huang et al.[235] used LSPs excitation from Al nanoparticles to improve the LEE of a UV-LED. Using the oblique angle deposition method, Al nanoparticles were deposited at the surface of the LED. At 60-deg deposition angle, maximum PL enhancement (329%) is recorded at 282-nm emission wavelength. This enhancement occurs because when the photons excite LSPs on the surfaces of the Al nanoparticles, these LSPs recombine and generate photons with stronger intensities. For the non-LED device, Shetty et al.[236] investigated the ability of plasmonic nanostructures to improve the performance of
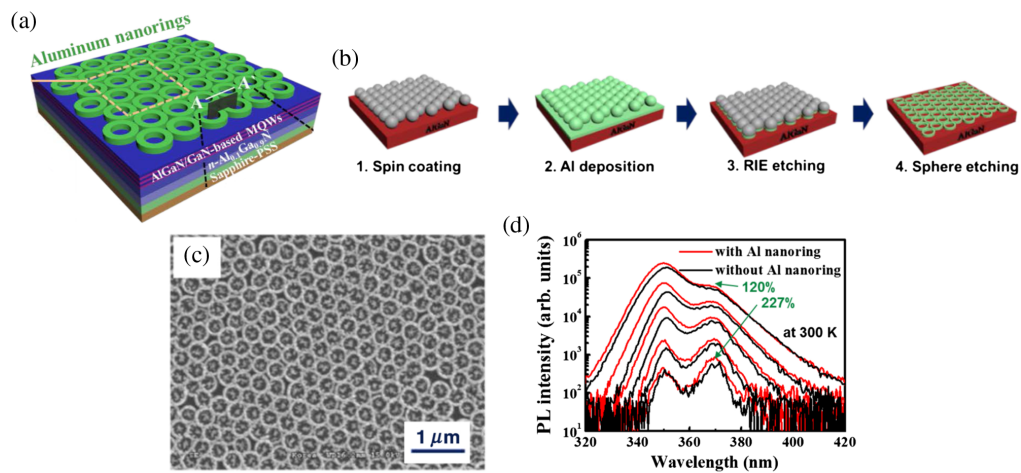
Fig. 36 (a) Schematic of the AlGaN/GaN MQW with Al nanorings. (b) Steps of Al nanorings deposition above the MQW. (c) AFM image for the nanorings above the MQW when using 300-nm silica nanospheres. (d) PL enhancement when measured at 300-K temperature. Reproduced with permission from Ref. 234.

Table 13 Summary of SP-enhanced UV-photonic devices.

Technique	Device type	Device structure	Device characteristics	Enhancement	Ref.
Thin plasmonic film	UVC–LED	Sapphire/AlGaN/GaN	Peak emission wavelength—294 nm	217% (PL)	230
	UVA–LED	Sapphire/AlGaN/GaN/AlGaN	Peak emission wavelength—372 nm	200% (PL)	231
Patterned plasmonic layer	UVA–LED	Si/AlN/n-AlGaN/AlGaN-MQW/p-AlGaN/p-GaN	Peak emission wavelength—346 nm I_{th}—~100 mA P_o—~1.2 mW at $I = 700$ mA	45% (PL)	232
HMM	UVB–LED	Sapphire/AlGaN/HMM/Al	Peak emission wavelength—318 nm	520% (EQE)	233
Plasmonic nanostructures	UVC–LED	Sapphire/AlN/Al$_{0.1}$Ga$_{0.9}$N/n-Al$_{0.1}$Ga$_{0.9}$N/MQW	Peak emission wavelength—266 nm Pump power 0.03 to 8 mW	227% (PL)	234
	UVB–LED	Sapphire/AlN/n-AlGaN/MQW/p-AlGaN/p-GaN	Peak emission wavelength—282 nm	329% (PL)	235
	UVA–UVB–PD	Metal-GaN-metal	Absorption wavelength—300 to 400 nm	Photocurrent	236

UV-PD. Incident UV light on the PD excites LSPs on the surface of Al nanostructures. The magnified fields near the metallic structures are then scattered to increase the PD photocurrent.

In Table 13, we summarize the different trials of enhancing UV-photonic devices using SPs. The table provides a comparison regarding the fabrication technique, device type, structure, characteristics, and the enhancement percentage.

5 Conclusions and Outlook

The continuously increasing development in UV-photonic devices has mainly resulted from the intensive research on nanophotonics and the advanced nanofabrication approaches applied to realize nanostructures. In this review, we have given a comprehensive description of nanophotonics implementations using nanostructured interfaces and nanofabrication approaches for the group III-nitride semiconductors to realize efficient UV photonic devices.

The NWs-based technology has recently been pursued due to the unique properties of NWs, e.g., high crystalline quality with low defect density and large surface-to-volume ratio. We have reviewed the most significant ways to grow high-quality NWs for UV applications. Lithography-based SAG, VLS growth, and the catalyst-free self-assisted growth schemes have been presented. The key element to improve the performance of UV-photonic devices is to reduce the TDDs and to solve the cracking issue of AlN and AlGaN films, which stems from the tensile strain beyond the critical layer thickness. Therefore, to enhance the material quality of epilayers grown on nonnative substrates, different ELOG schemes have been suggested and successfully employed to enhance the performance of UV devices. We show that research on GaN-based QDs and QDisks is very promising to develop highly efficient UV-photonic devices. Such devices are already outperforming their counterparts regarding material quality, IQE, LEE, responsivity,

sensitivity, and the tunability of the wavelength. However, the optical output power of such devices still needs to be improved.

The performance of UV-photonic devices can be also enhanced by utilizing surface roughening technologies, e.g., surface texturing and surface patterning. These technologies have shown a high impact on the LEE and device characteristics due to their abilities in increasing the extraction of photons, controlling the lateral waveguiding emission, and in improving the transparent p-contact layer. Further advances in lithography techniques will facilitate the roughening fabrication process and ensure high-resolution structure/surface features. We have also reviewed different shapes of PSSs, e.g., stripe-shaped, volcano-shaped, and groove-shaped, fabricated by the combination of a lithography method and either an additive technique (depositing a thin film on the substrate surface) or a subtractive technique (etching the substrate surface). We have shown that the utilization of PSSs is very effective to enhance the performance of the light-emitting UV devices in terms of decreasing the TDDs and increasing the LEE.

LEE, IQE, and EQE of the UV-photonic devices can also be improved using PhCs structures. In the case of DBRs which is a 1-D PhCs, we have reviewed the recent development of dielectric, epitaxial nitrides, and nitride/porous DBRs. Achieving a truly crack-free, broad stopband, and electrically conducting DBRs for the UV spectral range remains the main challenge. Several achievements on the usage of 2-D and 3-D PhCs on UV-LEDs have been shown. Furthermore, several types of NGs were reviewed, e.g., SWGs in the form of WGPs and 1-D/2-D grating patterns, and a DBR grating. Continuous advancement in the field of direct laser writing, for example, will ease and speed up true 3-D structure prototyping and testing, allowing for greater precision and smaller nanofeatures to be fabricated.

For the case of micro- and nanostructures, such as microdisk, nanopillars, and NWs, we have reviewed the reported structures and devices based on III-nitrides operating in the UV spectral range. We expect that the continuously improving quality of III-nitride materials, as well as cross-conceptual approaches, will further enhance the performance of UV lasing devices for future applications. We have discussed different plasmonic-based approaches used to improve the performance of UV devices. We have shown that Al-based plasmonic structures have been primarily used to enhance the EQE of UV emitters significantly. One major hurdle of using SP-enhanced UV devices is Al oxidation, which inhibits their feasibility. Therefore, it is necessary to discover other metallic materials that have plasmonic resonance within the UV range and do not oxidize in air. Further, we recommend trying to incorporate plasmonic structures, such as Al nanoparticles, within the active region, which would significantly increase IQE of UV emitters.

Acknowledgments

References

1. P. Mukish and P. Boulay, "UV LEDs—technology, manufacturing and application trends," 2016, https://www.i-micronews.com/led-report/product/uv-leds-technology-manufacturing-and-application-trends.html.
2. M. Kneissl and J. Rass, *III-Nitride Ultraviolet Emitters*, Vol. **227**, Springer Series in Materials Science, Springer, Cham, Switzerland (2016).
3. J. Y. Tsao et al., "Ultrawide-bandgap semiconductors: research opportunities and challenges," *Adv. Electron. Mater.* **4**(1), 1600501 (2018).
4. L. Sang, M. Liao, and M. Sumiya, "A comprehensive review of semiconductor ultraviolet photodetectors: from thin film to one-dimensional nanostructures," *Sensors* **13**(8), 10482–10518 (2013).
5. S. C. Jain et al., "III-nitrides: growth, characterization, and properties," *J. Appl. Phys.* **87**(3), 965–1006 (2000).

6. M. A. Khan et al., "III-nitride UV devices," *Jpn. J. Appl. Phys.* **44**(10), 7191–7206 (2005).
7. M. Kneissl et al., "Advances in group III-nitride based deep UV light-emitting diode technology," *Semicond. Sci. Technol.* **26**(1), 014036 (2011).
8. Y. Taniyasu and M. Kasu, "Polarization property of deep-ultraviolet light emission from C-plane AlN/GaN short-period superlattices," *Appl. Phys. Lett.* **99**(25), 251112 (2011).
9. Y. Tang et al., "Ultrahigh-speed GaN high-electron-mobility transistors with f_T/f_{max} of 454/444 GHz," *IEEE Electron Device Lett.* **36**(6), 549–551 (2015).
10. H. X. Jiang and J. Y. Lin, "Hexagonal boron nitride for deep ultraviolet photonic devices," *Semicond. Sci. Technol.* **29**(8), 084003 (2014).
11. X. Li et al., "BAlN thin layers for deep UV applications," *Phys. Status Solidi A* **212**(4), 745–750 (2015).
12. H. X. Jiang and J. Y. Lin, "Review-hexagonal boron nitride epilayers: growth, optical properties and device applications," *ECS J. Solid State Sci. Technol.* **6**(2), Q3012–Q3021 (2017).
13. N. Izyumskaya et al., "Recent development of boron nitride towards electronic applications," *Adv. Electron. Mater.* **3**(5), 1600485 (2017).
14. H. Hirayama et al., "Recent progress and future prospects of AlGaN-based high-efficiency deep-ultraviolet light-emitting diodes," *Jpn. J. Appl. Phys.* **53**(10), 100209 (2014).
15. D. Li et al., "AlGaN photonics: recent advances in materials and ultraviolet devices," *Adv. Opt. Photonics* **10**(1), 43–110 (2018).
16. J.-S. Park et al., "Review-group III-nitride-based ultraviolet light-emitting diodes: ways of increasing external quantum efficiency," *ECS J. Solid State Sci. Technol.* **6**(4), Q42–Q52 (2017).
17. S. Zhao et al., "III-nitride nanowire optoelectronics," *Prog. Quantum Electron.* **44**, 14–68 (2015).
18. N. Tansu et al., "Temperature analysis and characteristics of highly strained InGaAs-GaAsP-GaAs ($\lambda > 1.17 \, \mu$m) quantum-well lasers," *IEEE J. Quantum Electron.* **38**(6), 640–651 (2002).
19. A. Khan, K. Balakrishnan, and T. Katona, "Ultraviolet light-emitting diodes based on group three nitrides," *Nat. Photonics* **2**(2), 77–84 (2008).
20. J. Li et al., "Optical and electrical properties of Mg-doped p-type $Al_xGa_{1-x}N$," *Appl. Phys. Lett.* **80**(7), 1210–1212 (2002).
21. B. Mandl et al., "Au-free epitaxial growth of InAs nanowires," *Nano Lett.* **6**(8), 1817–1821 (2006).
22. S. D. Hersee, X. Sun, and X. Wang, "The controlled growth of GaN nanowires," *Nano Lett.* **6**(8), 1808–1811 (2006).
23. S. H. Oh et al., "Point defect configurations of supersaturated Au atoms inside Si nanowires," *Nano Lett.* **8**(4), 1016–1019 (2008).
24. K. Kishino and S. Ishizawa, "Selective-area growth of GaN nanocolumns on Si(111) substrates for application to nanocolumn emitters with systematic analysis of dislocation filtering effect of nanocolumns," *Nanotechnology* **26**(22), 225602 (2015).
25. R. Calarco et al., "Nucleation and growth of GaN nanowires on Si(111) performed by molecular beam epitaxy," *Nano Lett.* **7**(8), 2248–2251 (2007).
26. P. Kumar et al., "Superstructure of self-aligned hexagonal GaN nanorods formed on nitrided Si(111) surface," *Appl. Phys. Lett.* **101**(13), 131605 (2012).
27. K. Hestroffer et al., "In situ study of self-assembled GaN nanowires nucleation on Si(111) by plasma-assisted molecular beam epitaxy," *Appl. Phys. Lett.* **100**(21), 212107 (2012).
28. M. Tangi et al., "Role of quantum-confined stark effect on bias dependent photoluminescence of N-polar GaN/InGaN multi-quantum disk amber light emitting diodes," *J. Appl. Phys.* **123**(10), 105702 (2018).
29. M. Tangi et al., "Electron mobility of self-assembled and dislocation free InN nanorods grown on GaN nano wall network template," *J. Appl. Phys.* **119**(20), 205701 (2016).
30. M. Tangi et al., "Bandgap measurements and the peculiar splitting of E_2^H phonon modes of $In_xAl_{1-x}N$ nanowires grown by plasma assisted molecular beam epitaxy," *J. Appl. Phys.* **120**(4), 045701 (2016).

31. E. Calleja et al., "Growth, morphology, and structural properties of group-III-nitride nano-columns and nanodisks," *Phys. Status Solidi B* **244**(8), 2816–2837 (2007).

32. T. Gotschke et al., "Influence of the adatom diffusion on selective growth of GaN nanowire regular arrays," *Appl. Phys. Lett.* **98**(10), 103102 (2011).

33. K. Choi, M. Arita, and Y. Arakawa, "Selective-area growth of thin GaN nanowires by MOCVD," *J. Cryst. Growth* **357**(1), 58–61 (2012).

34. Y.-T. Lin, T.-W. Yeh, and P. D. Dapkus, "Mechanism of selective area growth of GaN nanorods by pulsed mode metalorganic chemical vapor deposition," *Nanotechnology* **23**(46), 465601 (2012).

35. Y. T. Lin et al., "Catalyst-free GaN nanorods synthesized by selective area growth," *Adv. Funct. Mater.* **24**(21), 3162–3171 (2014).

36. B. H. Le et al., "Controlled coalescence of AlGaN nanowire arrays: an architecture for nearly dislocation-free planar ultraviolet photonic device applications," *Adv. Mater.* **28**, 8446–8454 (2016).

37. D. Saxena et al., "Optically pumped room-temperature GaAs nanowire lasers," *Nat. Photonics* **7**(12), 963–968 (2013).

38. G. T. Wang et al., "Highly aligned, template-free growth and characterization of vertical GaN nanowires on sapphire by metal-organic chemical vapour deposition," *Nanotechnology* **17**(23), 5773–5780 (2006).

39. T. Kuykendall et al., "Metalorganic chemical vapor deposition route to GaN nanowires with triangular cross sections," *Nano Lett.* **3**(8), 1063–1066 (2003).

40. A. K. Sivadasan et al., "Optical properties of monodispersed AlGaN nanowires in the single-prong growth mechanism," *Cryst. Growth Des.* **15**(3), 1311–1318 (2015).

41. K. Hestroffer et al., "Polarity of GaN nanowires grown by plasma-assisted molecular beam epitaxy on Si(111)," *Phys. Rev. B* **84**(24), 245302 (2011).

42. B. Janjua et al., "Self-planarized quantum-disks-in-nanowires ultraviolet-B emitters utilizing pendeo-epitaxy," *Nanoscale* **9**(23), 7805–7813 (2017).

43. B. Janjua et al., "Ultraviolet-A LED based on quantum-disks-in-AlGaN-nanowires—optimization and device reliability," *IEEE Photonics J.* **10**(2), 2200711 (2018).

44. K. H. Li et al., "Ultralow-threshold electrically injected AlGaN nanowire ultraviolet lasers on Si operating at low temperature," *Nat. Nanotechnol.* **10**(2), 140–144 (2015).

45. M. Djavid and Z. Mi, "Enhancing the light extraction efficiency of AlGaN deep ultraviolet light emitting diodes by using nanowire structures," *Appl. Phys. Lett.* **108**(5), 051102 (2016).

46. R. Lin et al., "Tapering-induced enhancement of light extraction efficiency of nanowire deep ultraviolet LED by theoretical simulations," *Photonics Res.* **6**(5), 457–462 (2018).

47. S. M. Islam et al., "Deep-UV emission at 219 nm from ultrathin MBE GaN/AlN quantum heterostructures," *Appl. Phys. Lett.* **111**(9), 091104 (2017).

48. J. Ristić et al., "GaN/AlGaN nanocavities with AlN/GaN Bragg reflectors grown in AlGaN nanocolumns by plasma assisted MBE," *Phys. Status Solidi A* **202**(3), 367–371 (2005).

49. J. Verma et al., "Tunnel-injection GaN quantum dot ultraviolet light-emitting diodes," *Appl. Phys. Lett.* **102**(4), 041103 (2013).

50. J. Verma et al., "Tunnel-injection quantum dot deep-ultraviolet light-emitting diodes with polarization-induced doping in III-nitride heterostructures," *Appl. Phys. Lett.* **104**(2), 021105 (2014).

51. A. T. M. G. Sarwar et al., "Ultrathin GaN quantum disk nanowire LEDs with sub-250 nm electroluminescence," *Nanoscale* **8**(15), 8024–8032 (2016).

52. S. M. Islam et al., "Sub-230 nm deep-UV emission from GaN quantum disks in AlN grown by a modified Stranski-Krastanov mode," *Jpn. J. Appl. Phys.* **55**(5), 05FF06 (2016).

53. S. Tanaka, S. Iwai, and Y. Aoyagi, "Self-assembling GaN quantum dots on $Al_xGa_{1-x}N$ surfaces using a surfactant," *Appl. Phys. Lett.* **69**(26), 4096–4098 (1996).

54. W. Seifert et al., "In-situ growth of quantum dot structures by the Stranski–Kranstanow growth mode," *Prog. Cryst. Growth Ch.* **33**(4), 423–471 (1996).

55. N. Gogneau et al., "Structure of GaN quantum dots grown under 'modified Stranski–Krastanow' conditions on AlN," *J. Appl. Phys.* **94**(4), 2254–2261 (2003).

56. J. Ristić et al., "Characterization of GaN quantum discs embedded in $Al_xGa_{1-x}N$ nanocolumns grown by molecular beam epitaxy," *Phys. Rev. B* **68**(12), 125305 (2003).

57. J. Ristić et al., "Carrier-confinement effects in nanocolumnar GaN/Al$_x$Ga$_{1-x}$N quantum disks grown by molecular-beam epitaxy," *Phys. Rev. B* **72**(8), 085330 (2005).

58. S. Tanaka et al., "A UV light-emitting diode incorporating GaN quantum dots," *Jpn. J. Appl. Phys.* **42**(8A), L885–L887 (2003).

59. Y. Taniyasu, M. Kasu, and T. Makimoto, "An aluminium nitride light-emitting diode with a wavelength of 210 nanometres," *Nature* **441**(7091), 325–328 (2006).

60. H. Sekiguchi, K. Kishino, and A. Kikuchi, "GaN/AlGaN nanocolumn ultraviolet light-emitting diodes grown on n-(111) Si by RF-plasma-assisted molecular beam epitaxy," *Electron. Lett.* **44**(2), 151–152 (2008).

61. L. Rigutti et al., "Ultraviolet photodetector based on GaN/AlN quantum disks in a single nanowire," *Nano Lett.* **10**(8), 2939–2943 (2010).

62. D. Priante et al., "Highly uniform ultraviolet-A quantum-confined AlGaN nanowire LEDs on metal/silicon with a TaN interlayer," *Opt. Mater. Express* **7**(12), 4214–4224 (2017).

63. M. Spies et al., "Bias-controlled spectral response in GaN/AlN single-nanowire ultraviolet photodetectors," *Nano Lett.* **17**(7), 4231–4239 (2017).

64. J. Renard et al., "Suppression of nonradiative processes in long-lived polar GaN/AlN quantum dots," *Appl. Phys. Lett.* **95**(13), 131903 (2009).

65. S. Zhao et al., "Sub-milliwatt AlGaN nanowire tunnel junction deep ultraviolet light emitting diodes on silicon operating at 242 nm," *Appl. Phys. Lett.* **109**(20), 201106 (2016).

66. K. Balakrishnan et al., "Influence of high temperature in the growth of low dislocation content AlN bridge layers on patterned 6H-SiC substrates by metalorganic vapor phase epitaxy," *Jpn. J. Appl. Phys.* **46**(12–16), L307–L310 (2007).

67. Z. Chen et al., "Pulsed lateral epitaxial overgrowth of aluminum nitride on sapphire substrates," *Appl. Phys. Lett.* **89**(8), 081905 (2006).

68. V. Adivarahan et al., "Robust 290 nm emission light emitting diodes over pulsed laterally overgrown AlN," *Jpn. J. Appl. Phys.* **46**(36–40), L877–L879 (2007).

69. R. Jain et al., "Migration enhanced lateral epitaxial overgrowth of AlN and AlGaN for high reliability deep ultraviolet light emitting diodes," *Appl. Phys. Lett.* **93**(5), 051113 (2008).

70. B. S. Cheng et al., "Light output enhancement of UV light-emitting diodes with embedded distributed Bragg reflector," *IEEE Photonics Technol. Lett.* **23**(10), 642–644 (2011).

71. C.-Y. Huang et al., "MQWs InGaN/GaN LED with embedded micro-mirror array in the epitaxial-lateral-overgrowth gallium nitride for light extraction enhancement," *Opt. Express* **18**(10), 10674–10684 (2010).

72. M. Tangi, A. De, and S. M. Shivaprasad, "Role of dislocations and carrier concentration in limiting the electron mobility of InN films grown by plasma assisted molecular beam epitaxy," *J. Appl. Phys.* **123**(1), 015701 (2018).

73. M. Conroy et al., "Epitaxial lateral overgrowth of AlN on self-assembled patterned nanorods," *J. Mater. Chem. C* **3**(2), 431–437 (2015).

74. D. Lee et al., "Improved performance of AlGaN-based deep ultraviolet light-emitting diodes with nano-patterned AlN/sapphire substrates," *Appl. Phys. Lett.* **110**(19), 191103 (2017).

75. V. Kueller et al., "Modulated epitaxial lateral overgrowth of AlN for efficient UV LEDs," *IEEE Photonics Technol. Lett.* **24**(18), 1603–1605 (2012).

76. H. Yoshida et al., "A 342-nm ultraviolet AlGaN multiple-quantum-well laser diode," *Nat. Photonics* **2**(9), 551–554 (2008).

77. A. Usui et al., "Thick GaN epitaxial growth with low dislocation density by hydride vapor phase epitaxy," *Jpn. J. Appl. Phys.* **36**(7B), L899–L902 (1997).

78. P. Gupta et al., "Layered transition metal dichalcogenides: promising near-lattice-matched substrates for GaN growth," *Sci. Rep.* **6**(1), 23708 (2016).

79. M. Tangi et al., "Determination of band offsets at GaN/single-layer MoS$_2$ heterojunction," *Appl. Phys. Lett.* **109**(3), 032104 (2016).

80. P. Mishra et al., "Impact of N-plasma and Ga-irradiation on MoS$_2$ layer in molecular beam epitaxy," *Appl. Phys. Lett.* **110**(1), 012101 (2017).

81. M. Tangi et al., "Band alignment at GaN/single-layer WSe$_2$ interface," *ACS Appl. Mater. Interfaces* **9**(10), 9110–9117 (2017).

82. Y. Sun et al., "Nucleation mechanism of GaN growth on wet etched pattern sapphire substrates," *CrystEngComm* **16**(24), 5458–5465 (2014).

83. J. B. Kim et al., "Light extraction enhancement of GaN-based light-emitting diodes using volcano-shaped patterned sapphire substrates," *Jpn. J. Appl. Phys.* **49**(4R), 042102 (2010).

84. Z. Liu et al., "Fabrication of GaN hexagonal cones by inductively coupled plasma reactive ion etching," *J. Vac. Sci. Technol. B* **34**(4), 041226 (2016).

85. C. C. Pan et al., "Light output improvement of InGaN ultraviolet light-emitting diodes by using wet-etched stripe-patterned sapphire substrates," *J. Appl. Phys.* **102**(8), 084503 (2007).

86. P. Dong et al., "282-nm AlGaN-based deep ultraviolet light-emitting diodes with improved performance on nano-patterned sapphire substrates," *Appl. Phys. Lett.* **102**(24), 241113 (2013).

87. M. Khizar et al., "Nitride deep-ultraviolet light-emitting diodes with microlens array," *Appl. Phys. Lett.* **86**(17), 173504 (2005).

88. M. Kim et al., "AlGaN-based deep ultraviolet light-emitting diodes fabricated on patterned sapphire substrates," *Appl. Phys. Express* **4**(9), 092102 (2011).

89. X. Chen et al., "Deep-ultraviolet stimulated emission from AlGaN/AlN multiple-quantum-wells on nano-patterned AlN/sapphire templates with reduced threshold power density," *J. Alloys Compd.* **723**, 192–196 (2017).

90. S. I. Inoue, N. Tamari, and M. Taniguchi, "150 mW deep-ultraviolet light-emitting diodes with large-area AlN nanophotonic light-extraction structure emitting at 265 nm," *Appl. Phys. Lett.* **110**(14), 141106 (2017).

91. S. I. Inoue et al., "Light extraction enhancement of 265 nm deep-ultraviolet light-emitting diodes with over 90 mW output power via an AlN hybrid nanostructure," *Appl. Phys. Lett.* **106**(13), 131104 (2015).

92. J. Kim et al., "Deep-ultraviolet AlGaN/AlN core-shell multiple quantum wells on AlN nanorods via lithography-free method," *Sci. Rep.* **8**(1), 935 (2018).

93. Y. J. Lee et al., "Improvement in light-output efficiency of near-ultraviolet InGaN-GaN LEDs fabricated on stripe patterned sapphire substrate," in *Pacific Rim Conf. on Lasers and Electro-Optics (CLEO-PR)*, CWAB3-P53 (2005).

94. S. Zhou et al., "Comparative study of GaN-based ultraviolet LEDs grown on different-sized patterned sapphire substrates with sputtered AlN nucleation layer," *Jpn. J. Appl. Phys.* **56**(11), 111001 (2017).

95. D. Alden et al., "Fabrication and structural properties of AlN submicron periodic lateral polar structures and waveguides for UV-C applications," *Appl. Phys. Lett.* **108**(26), 261106 (2016).

96. H. J. Kang et al., "Improving light-emitting diode performance through sapphire substrate double-side patterning," *Opt. Eng.* **52**(2), 023002 (2013).

97. X.-F. Li et al., "Fabrication of patterned sapphire substrate and effect of light emission pattern on package efficiency," *Opt. Mater. Express* **5**(8), 1784–1791 (2015).

98. Y. Guo et al., "Light extraction enhancement of AlGaN-based ultraviolet light-emitting diodes by substrate sidewall roughening," *Appl. Phys. Lett.* **111**(1), 011102 (2017).

99. Y. Zhang et al., "Near milliwatt power AlGaN-based ultraviolet light emitting diodes based on lateral epitaxial overgrowth of AlN on Si(111)," *Appl. Phys. Lett.* **102**(1), 011106 (2013).

100. B. T. Tran and H. Hirayama, "Growth and fabrication of high external quantum efficiency AlGaN-based deep ultraviolet light-emitting diode grown on pattern Si substrate," *Sci. Rep.* **7**(1), 12176 (2017).

101. İ. Demir et al., "Direct growth of thick AlN layers on nanopatterned Si substrates by cantilever epitaxy," *Phys. Status Solidi A* **214**(4), 1600363 (2017).

102. C. E. Lee et al., "Output power enhancement of vertical-injection ultraviolet light-emitting diodes by GaN-free and surface roughness structures," *Electrochem. Solid-State Lett.* **12**(2), H44–H46 (2009).

103. Y. C. Chiang et al., "Enhanced performance of nitride-based ultraviolet vertical-injection light-emitting diodes by non-insulation current blocking layer and textured surface," *Nanoscale Res. Lett.* **9**(1), 699 (2014).

104. Y. C. Chiang, C. C. Lin, and H. C. Kuo, "Novel thin-GaN LED structure adopted micro abraded surface to compare with conventional vertical LEDs in ultraviolet light," *Nanoscale Res. Lett.* **10**(1), 182 (2015).

105. L. Zhou et al., "Vertical injection thin-film AlGaN/AlGaN multiple-quantum-well deep ultraviolet light-emitting diodes," *Appl. Phys. Lett.* **89**(24), 241113 (2006).

106. B. J. Kim et al., "Enhancement of light extraction efficiency of ultraviolet light emitting diodes by patterning of SiO_2 nanosphere arrays," *Thin Solid Films* **517**(8), 2742–2744 (2009).

107. X. Liu et al., "Molecular beam epitaxial growth and characterization of AlN nanowall deep UV light emitting diodes," *Appl. Phys. Lett.* **111**(10), 101103 (2017).

108. W. Guo et al., "Enhancing light coupling and emission efficiencies of AlGaN thin film and AlGaN/GaN multiple quantum wells with periodicity-wavelength matched nanostructure array," *Nanoscale* **9**(40), 15477–15483 (2017).

109. Y. Peng et al., "Light efficiency enhancement of deep ultraviolet light-emitting diodes packaged by nanostructured silica glass," *J. Disp. Technol.* **12**(10), 1106–1111 (2016).

110. J. W. Lee et al., "Arrays of truncated cone AlGaN deep-ultraviolet light-emitting diodes facilitating efficient outcoupling of in-plane emission," *ACS Photonics* **3**(11), 2030–2034 (2016).

111. T. Takano et al., "Deep-ultraviolet light-emitting diodes with external quantum efficiency higher than 20% at 275 nm achieved by improving light-extraction efficiency," *Appl. Phys. Express* **10**(3), 031002 (2017).

112. G. B. Fayisa et al., "Enhanced light extraction efficiency of micro-ring array AlGaN deep ultraviolet light-emitting diodes," *Jpn. J. Appl. Phys.* **56**(9), 092101 (2017).

113. Y. Peng et al., "Enhanced light extraction from DUV-LEDs by AlN-doped fluoropolymer encapsulation," *IEEE Photonics Technol. Lett.* **29**(14), 1151–1154 (2017).

114. S. Nagai et al., "Development of highly durable deep-ultraviolet AlGaN-based LED multi-chip array with hemispherical encapsulated structures using a selected resin through a detailed feasibility study," *Jpn. J. Appl. Phys.* **55**(8), 082101 (2016).

115. S. Wu et al., "Micro-pixel design milliwatt power 254 nm emission light emitting diodes," *Jpn. J. Appl. Phys.* **43**(8A), L1035–L1037 (2004).

116. N. Lobo et al., "Enhancement of light extraction in ultraviolet light-emitting diodes using nanopixel contact design with Al reflector," *Appl. Phys. Lett.* **96**(8), 081109 (2010).

117. S. M. Mitani, P. K. Choudhury, and M. S. Alias, "On the characterization of a new type of oxide-confined 850 nm GaAs-based vertical-cavity surface-emitting laser," *Optik* **119**(8), 373–378 (2008).

118. M. S. Alias et al., "Improved efficiency of GaAs-based VCSEL by utilizing fan-pad metallization and trench patterning," *Laser Phys.* **19**(11), 2096–2101 (2009).

119. M. S. Alias, S. Shaari, and S. M. Mitani, "Optimization of electro-optical characteristics of GaAs-based oxide confinement VCSEL," *Laser Phys.* **20**(4), 806–810 (2010).

120. A. N. Al-Omari et al., "Improved performance of top-emitting oxide-confined polyimide-planarized 980 nm VCSELs with copper-plated heat sinks," *J. Phys. D Appl. Phys.* **45**(50), 505101 (2012).

121. D. Priante et al., "The recombination mechanisms leading to amplified spontaneous emission at the true-green wavelength in $CH_3NH_3PbBr_3$ perovskites," *Appl. Phys. Lett.* **106**(8), 081902 (2015).

122. M. S. Alias et al., "Continuous-wave optically pumped green perovskite vertical-cavity surface-emitter," *Opt. Lett.* **42**(18), 3618–3621 (2017).

123. B. Murali et al., "Temperature-induced lattice relaxation of perovskite crystal enhances optoelectronic properties and solar cell performance," *J. Phys. Chem. Lett.* **8**(1), 137–143 (2017).

124. M. S. Alias and S. Shaari, "Analysis of single-mode condition and high-order modes discrimination in photonic crystal VCSEL," *Appl. Phys. B* **103**(4), 889–896 (2011).

125. M. S. Alias et al., "Single transverse mode control of VCSEL by photonic crystal and trench patterning," *Photonics Nanostruct.* **8**(1), 38–46 (2010).

126. M. S. Alias et al., "Highly confined and continuous single-mode operation of self-align photonic crystal oxide VCSEL," *Appl. Phys. B* **100**(3), 453–459 (2010).

127. M. S. Alias and S. Shaari, "Loss analysis of high order modes in photonic crystal vertical-cavity surface-emitting lasers," *J. Light. Technol.* **28**(10), 1556–1563 (2010).

128. P. O. Leisher et al., "High modulation bandwidth implant-confined photonic crystal vertical-cavity surface-emitting lasers," *IEEE Photonics Technol. Lett.* **19**(19), 1541–1543 (2007).

129. J. Y. Zhang et al., "Blue-violet lasing of optically pumped GaN-based vertical cavity surface-emitting laser with dielectric distributed Bragg reflectors," *J. Light. Technol.* **27**(1), 55–59 (2009).

130. T. Someya et al., "Lasing emission from an $In_{0.1}Ga_{0.9}N$ vertical cavity surface emitting laser," *Jpn. J. Appl. Phys.* **37**(12A), L1424–L1426 (1998).

131. Y. S. Liu et al., "Optically pumped vertical-cavity surface-emitting laser at 374.5 nm with an electrically conducting n-DBR," *Appl. Phys. Express* **9**(11), 111002 (2016).

132. T. Moudakir et al., "Design, fabrication, and characterization of near-milliwatt-power RCLEDs emitting at 390 nm," *IEEE Photonics J.* **5**(6), 8400709 (2013).

133. Z. Xie et al., "AlGaN-based 330 nm resonant-cavity-enhanced p–i–n junction ultraviolet photodetectors using AlN/AlGaN distributed Bragg reflectors," *Phys. Status Solidi C* **7**(7–8), 1821–1824 (2010).

134. Y. Ma et al., "Enhanced light output of near-ultraviolet LEDs with Ta_2O_5/SiO_2 hybrid DBR reflector," *IEEE Photonics Technol. Lett.* **29**(18), 1564–1567 (2017).

135. G. J. Wang et al., "GaN/AlGaN ultraviolet light-emitting diode with an embedded porous-AlGaN distributed Bragg reflector," *Appl. Phys. Express* **10**(12), 122102 (2017).

136. T. Wang et al., "Highly improved performance of a 350 nm ultraviolet light-emitting diode containing $Al_xGa_{1-x}N/Al_yGa_{1-y}N$ distributed Bragg reflectors," *J. Cryst. Growth* **267**(3–4), 583–587 (2004).

137. C. C. Chen et al., "Ultraviolet GaN-based microdisk laser with AlN/AlGaN distributed Bragg reflector," *Appl. Phys. Lett.* **96**(15), 151115 (2010).

138. M. Liu et al., "Comparative experimental and simulation studies of high-power AlGaN-based 353 nm ultraviolet flip-chip and top-emitting LEDs," *Jpn. J. Appl. Phys.* **57**(3), 031001 (2018).

139. T. T. Kao et al., "Sub-250 nm low-threshold deep-ultraviolet AlGaN-based heterostructure laser employing HfO_2/SiO_2 dielectric mirrors," *Appl. Phys. Lett.* **103**(21), 211103 (2013).

140. T. Someya et al., "Room temperature lasing at blue wavelengths in gallium nitride microcavities," *Science* **285**(5435), 1905–1906 (1999).

141. A. Alyamani et al., "GaN hybrid microcavities in the strong coupling regime grown by metal-organic chemical vapor deposition on sapphire substrates," *J. Appl. Phys.* **101**(9), 093110 (2007).

142. M. L. Grilli et al., "Al_2O_3/SiO_2 and HfO_2/SiO_2 dichroic mirrors for UV solid-state lasers," *Thin Solid Films* **517**(5), 1731–1735 (2009).

143. P. Torchio et al., "High-reflectivity HfO_2/SiO_2 ultraviolet mirrors," *Appl. Opt.* **41**(16), 3256–3261 (2002).

144. M. S. Alias et al., "High reflectivity YDH/SiO_2 distributed Bragg reflector for UV-C wavelength regime," *IEEE Photonics J.* **10**(2), 2200508 (2018).

145. M. S. Alias et al., "Optical constants of $CH_3NH_3PbBr_3$ perovskite thin films measured by spectroscopic ellipsometry," *Opt. Express* **24**(15), 16586–16594 (2016).

146. G. S. Huang et al., "Crack-free GaN/AlN distributed Bragg reflectors incorporated with GaN/AlN superlattices grown by metalorganic chemical vapor deposition," *Appl. Phys. Lett.* **88**(6), 061904 (2006).

147. D. Wang et al., "Crack-free ultraviolet AlGaN/GaN distributed Bragg reflectors grown by MOVPE on 6H-SiC(0 0 0 1)," *Superlattices Microstruct.* **70**, 54–60 (2014).

148. T. Someya and Y. Arakawa, "Highly reflective $GaN/Al_{0.34}Ga_{0.6}N$ quarter-wave reflectors grown by metal organic chemical vapor deposition," *Appl. Phys. Lett.* **73**(25), 3653–3655 (1998).

149. T. Moudakir et al., "Suppression of crack generation in AlGaN/GaN distributed Bragg reflectors grown by MOVPE," *J. Cryst. Growth* **370**, 12–15 (2013).

150. K. E. Waldrip et al., "Stress engineering during metalorganic chemical vapor deposition of AlGaN/GaN distributed Bragg reflectors," *Appl. Phys. Lett.* **78**(21), 3205–3207 (2001).

151. Y. S. Liu et al., "Strain management of AlGaN-based distributed Bragg reflectors with GaN interlayer grown by metalorganic chemical vapor deposition," *Appl. Phys. Lett.* **109**(8), 081103 (2016).

152. A. Bhattacharyya et al., "High reflectivity and crack-free AlGaN/AlN ultraviolet distributed Bragg reflectors," *J. Vac. Sci. Technol. B* **20**(3), 1229–1233 (2002).

153. A. Franke et al., "High reflectivity III-nitride UV-C distributed Bragg reflectors for vertical cavity emitting lasers," *J. Appl. Phys.* **120**(13), 135703 (2016).

154. A. Franke et al., "Strain engineered high reflectivity DBRs in the deep UV," *Proc. SPIE* **9748**, 97481G (2016).

155. M. Abid et al., "Distributed Bragg reflectors based on diluted boron-based BAlN alloys for deep ultraviolet optoelectronic applications," *Appl. Phys. Lett.* **100**(5), 051101 (2012).

156. C. Berger et al., "In-situ growth monitoring of AlInN/AlGaN distributed Bragg reflectors for the UV-spectral range," *J. Cryst. Growth* **370**, 87–91 (2013).

157. C. Berger et al., "Growth of AlInN/AlGaN distributed Bragg reflectors for high quality microcavities," *Phys. Status Solidi C* **9**(5), 1253–1258 (2012).

158. E. Feltin et al., "Crack-free highly reflective AlInN/AlGaN Bragg mirrors for UV applications," *Appl. Phys. Lett.* **88**(5), 051108 (2006).

159. L. Zhang et al., "Solar-blind ultraviolet AlInN/AlGaN distributed Bragg reflectors," *Appl. Phys. Lett.* **102**(24), 242112 (2013).

160. J. Chang et al., "High-quality crystal growth and characteristics of AlGaN-based solar-blind distributed Bragg reflectors with a tri-layer period structure," *Sci. Rep.* **6**(1), 29571 (2016).

161. Y. Kashima et al., "High external quantum efficiency (10%) AlGaN-based deep-ultraviolet light-emitting diodes achieved by using highly reflective photonic crystal on p-AlGaN contact layer," *Appl. Phys. Express* **11**(1), 012101 (2018).

162. J. B. Shakya, "III-nitride blue and UV photonic-crystal light-emitting diodes," *Proc. SPIE* **5530**, 241–250 (2004).

163. T. N. Oder et al., "III-nitride blue and ultraviolet photonic crystal light emitting diodes," *Appl. Phys. Lett.* **84**(4), 466–468 (2004).

164. J. Shakya, J. Y. Lin, and H. X. Jiang, "Time-resolved electroluminescence studies of III-nitride ultraviolet photonic-crystal light-emitting diodes," *Appl. Phys. Lett.* **85**(11), 2104–2106 (2004).

165. D. Néel et al., "Aluminum nitride photonic crystals and microdiscs for ultra-violet nanophotonics," *Adv. Nat. Sci. Nanosci.* **5**(2), 023001 (2014).

166. C. C. Chen et al., "Tunable light emission from GaN-based photonic crystal with ultraviolet AlN/AlGaN distributed Bragg reflector," *Jpn. J. Appl. Phys.* **50**(45), 04DG09 (2011).

167. C. C. Chen et al., "Light emission enhancement of GaN-based photonic crystal with ultraviolet AlN/AlGaN distributed Bragg reflector," *J. Lightwave Technol.* **28**(22), 3189–3192 (2010).

168. J. Zhang et al., "Fabrication and photovoltaic measurements of surface nanostructure of AlGaInN-based photodetector," *Jpn. J. Appl. Phys.* **48**(11R), 111001 (2009).

169. X.-L. Hu et al., "III-nitride ultraviolet, blue and green LEDs with SiO_2 photonic crystals fabricated by UV-nanoimprint lithography," *Mater. Sci. Semicond. Process.* **79**, 61–65 (2018).

170. J. Shakya et al., "Enhanced light extraction in III-nitride ultraviolet photonic crystal light-emitting diodes," *Appl. Phys. Lett.* **85**(1), 142–144 (2004).

171. Z. Y. Fan, J. Y. Lin, and H. X. Jiang, "III-nitride deep ultraviolet micro- and nano-photonics," *Proc. SPIE* **6127**, 61271C (2006).

172. M. S. Alias et al., "Enhancing the light-extraction efficiency of an AlGaN nanowire ultraviolet light-emitting diode by using nitride/air distributed Bragg reflector nanogratings," *IEEE Photonics J.* **9**(5), 4900508 (2017).

173. M. S. Alias et al., "Enhanced etching, surface damage recovery, and submicron patterning of hybrid perovskites using a chemically gas-assisted focused-ion beam for subwavelength grating photonic applications," *J. Phys. Chem. Lett.* **7**(1), 137–142 (2016).

174. M. S. Alias et al., "Focused-ion beam patterning of organolead trihalide perovskite for subwavelength grating nanophotonic applications," *J. Vac. Sci. Technol. B* **33**(5), 051207 (2015).

175. Y. Takashima et al., "Ultraviolet polarizer with a Ge subwavelength grating," *Appl. Opt.* **56**(29), 8224–8229 (2017).

176. T. Weber et al., "High aspect ratio deep UV wire grid polarizer fabricated by double patterning," *Microelectron. Eng.* **98**, 433–435 (2012).

177. T. Weber et al., "Iridium wire grid polarizer fabricated using atomic layer deposition," *Nanoscale Res. Lett.* **6**, 558 (2011).

178. T. Siefke et al., "Materials pushing the application limits of wire grid polarizers further into the deep ultraviolet spectral range," *Adv. Opt. Mater.* **4**(11), 1780–1786 (2016).

179. T. Weber et al., "Tungsten wire grid polarizer for applications in the DUV spectral range," *Appl. Opt.* **51**(16), 3224–3227 (2012).

180. T. Weber et al., "Silicon wire grid polarizer for ultraviolet applications," *Appl. Opt.* **53**(34), 8140–8144 (2014).

181. K. Asano et al., "Fabrication and characterization of a deep ultraviolet wire grid polarizer with a chromium-oxide subwavelength grating," *Appl. Opt.* **53**(13), 2942–2948 (2014).

182. Y. Takashima et al., "Highly polarized emission from a GaN-based ultraviolet light-emitting diode using a Si-subwavelength grating on a SiO_2 underlayer," *Opt. Commun.* **369**, 38–43 (2016).

183. Y. Takashima et al., "Polarized emission characteristics of UV-LED with subwavelength grating," *Jpn. J. Appl. Phys.* **53**(7), 072101 (2014).

184. G. Miyaji and K. Miyazaki, "Fabrication of 50-nm period gratings on GaN in air through plasmonic near-field ablation induced by ultraviolet femtosecond laser pulses," *Opt. Express* **24**(5), 4648–4653 (2016).

185. K. J. Chen et al., "Lasing characteristics of a metal-coated GaN shallow grating structure at room temperature," *IEEE J. Sel. Top. Quantum Electron.* **21**(1), 4600105 (2015).

186. T. S. Kim et al., "Increase of light extraction from GaN based light emitting diodes incorporating patterned structure by colloidal lithography," *Appl. Phys. Lett.* **91**(17), 171114 (2007).

187. D.-S. Leem et al., "Light-output enhancement of GaN-based light-emitting diodes by using hole-patterned transparent indium tin oxide electrodes," *J. Appl. Phys.* **98**(7), 076107 (2005).

188. S. Butun, N. A. Cinel, and E. Ozbay, "Nanoantenna coupled UV subwavelength photodetectors based on GaN," *Opt. Express* **20**(3), 2649–2656 (2012).

189. H. G. Hong et al., "Enhancement of the light output of GaN-based ultraviolet light-emitting diodes by a one-dimensional nanopatterning process," *Appl. Phys. Lett.* **88**(10), 103505 (2006).

190. H.-G. Hong et al., "Enhanced light output of GaN-based near-UV light-emitting diodes by using nanopatterned indium tin oxide electrodes," *Semicond. Sci. Technol.* **21**(5), 594–597 (2006).

191. Z. Zhuang et al., "Large-scale fabrication and luminescence properties of GaN nanostructures by a soft UV-curing nanoimprint lithography," *Nanotechnology* **24**(40), 405303 (2013).

192. K.-J. Byeon and H. Lee, "Recent progress in direct patterning technologies based on nanoimprint lithography," *Eur. Phys. J. Appl. Phys.* **59**(1), 10001 (2012).

193. H. X. Jiang and J. Y. Lin, "Advances in III-nitride microstructures and micro-size emitters," *J. Korean Phys. Soc.* **42**(9), S757–S764 (2003).

194. Y. Zhang et al., "Advances in III-nitride semiconductor microdisk lasers," *Phys. Status Solidi A* **212**(5), 960–973 (2015).

195. R. A. Mair et al., "Optical properties of GaN/AlGaN multiple quantum well microdisks," *Appl. Phys. Lett.* **71**(20), 2898–2900 (1997).

196. M. Kneissl et al., "Current-injection spiral-shaped microcavity disk laser diodes with unidirectional emission," *Appl. Phys. Lett.* **84**(14), 2485–2487 (2004).

197. H. W. Choi et al., "Lasing in GaN microdisks pivoted on Si," *Appl. Phys. Lett.* **89**(21), 211101 (2006).

198. G. Zhu et al., "Single-mode ultraviolet whispering gallery mode lasing from a floating GaN microdisk," *Opt. Lett.* **43**(4), 647–650 (2018).

199. Y. Zhang et al., "Optically-pumped single-mode deep-ultraviolet microdisk lasers with AlGaN-based multiple quantum wells on Si substrate," *IEEE Photonics J.* **9**(5), 2400508 (2017).

200. J. Selles et al., "Deep-UV nitride-on-silicon microdisk lasers," *Sci. Rep.* **6**(1), 21650 (2016).

201. R. A. Mair et al., "Optical modes within III-nitride multiple quantum well microdisk cavities," *Appl. Phys. Lett.* **72**(13), 1530–1532 (1998).

202. S. Chang et al., "Stimulated emission and lasing in whispering-gallery modes of GaN microdisk cavities," *Appl. Phys. Lett.* **75**(2), 166–168 (1999).

203. S. Chang et al., "GaN near-UV microdisk lasers: efficient pumping configuration and low lasing threshold," in *Conf. on Lasers and Electro-Optics (CLEO)*, CTuU6 (1999).

204. N. B. Rex et al., "Directional stimulated emission from deformed GaN micropillar cavities," in *12th Annual Meeting IEEE Lasers and Electro-Optics Society (LEOS)*, WT2 (1999).

205. N. B. Rex et al., "Directional laser emission from chaotic modes in quadrupole-deformed GaN microdisks," in *Conf. on Lasers and Electro-Optics (CLEO)*, CTuA57 (2000).

206. S. Sergent et al., "GaN quantum dots in (Al, Ga)N-based microdisks," *J. Phys. Conf. Ser.* **210**(1), 012005 (2010).

207. M. Mexis et al., "High quality factor nitride-based optical cavities: microdisks with embedded GaN/Al(Ga)N quantum dots," *Opt. Lett.* **36**(12), 2203–2205 (2011).

208. M. Bürger et al., "Cubic GaN quantum dots embedded in zinc-blende AlN microdisks," *J. Cryst. Growth* **378**, 287–290 (2013).

209. M. Bürger et al., "Whispering gallery modes in zinc-blende AlN microdisks containing non-polar GaN quantum dots," *Appl. Phys. Lett.* **102**(8), 081105 (2013).

210. M. Bürger et al., "Lasing properties of non-polar GaN quantum dots in cubic aluminum nitride microdisk cavities," *Appl. Phys. Lett.* **103**(2), 021107 (2013).

211. J. Sellés et al., "III-nitride-on-silicon microdisk lasers from the blue to the deep ultra-violet," *Appl. Phys. Lett.* **109**(23), 231101 (2016).

212. Y. Zhang et al., "UV-C whispering-gallery modes in AlN microdisks with AlGaN-based multiple quantum wells on Si substrate," *J. Nanophotonics* **12**(4), 043502 (2018).

213. R. Chen et al., "Optically pumped ultraviolet lasing from nitride nanopillars at room temperature," *Appl. Phys. Lett.* **96**(24), 241101 (2010).

214. K. H. Li, Z. Ma, and H. W. Choi, "Single-mode whispering gallery lasing from metal-clad GaN nanopillars," *Opt. Lett.* **37**(3), 374–376 (2012).

215. Q. Li et al., "Single-mode GaN nanowire lasers," *Opt. Express* **20**(16), 17873–17879 (2012).

216. H. Xu et al., "Single-mode lasing of GaN nanowire-pairs," *Appl. Phys. Lett.* **101**(11), 113106 (2012).

217. H. Xu et al., "Gold substrate-induced single-mode lasing of GaN nanowires," *Appl. Phys. Lett.* **101**(22), 221114 (2012).

218. Y. C. Hsu et al., "Room temperature ultraviolet GaN metal-coated nanorod laser," *Appl. Phys. Lett.* **103**(19), 191102 (2013).

219. J. B. Wright et al., "Distributed feedback gallium nitride nanowire lasers," *Appl. Phys. Lett.* **104**(4), 041107 (2014).

220. G. Griffel, "Vernier effect in asymmetrical ring resonator arrays," *IEEE Photonics Technol. Lett.* **12**(12), 1642–1644 (2000).

221. K. C. Zeng et al., "Optical resonance modes in InGaN/GaN multiple-quantum-well microring cavities," *Appl. Phys. Lett.* **75**(17), 2563–2565 (1999).

222. Y. G. Wang et al., "Room temperature lasing with high group index in metal-coated GaN nanoring," *Appl. Phys. Lett.* **99**(25), 251111 (2011).

223. Y. G. Wang et al., "Lasing in metal-coated GaN nanostripe at room temperature," *Appl. Phys. Lett.* **98**(13), 131110 (2011).

224. Y. Zhang et al., "GaN hemispherical micro-cavities," *Appl. Phys. Lett.* **108**(3), 031110 (2016).

225. L. C. Wang et al., "Optically pumped lasing with a Q-factor exceeding 6000 from wet-etched GaN micro-pyramids," *Opt. Lett.* **42**(15), 2976–2979 (2017).

226. W. C. Liao et al., "Optimized spiral metal-gallium-nitride nanowire cavity for ultrahigh circular dichroism ultraviolet lasing at room temperature," *Sci. Rep.* **6**(1), 26578 (2016).

227. M. Honda et al., "UV plasmonic device for sensing ethanol and acetone," *Appl. Phys. Express* **11**(1), 012001 (2018).

228. K. Appusamy, "Development of materials for ultraviolet plasmonics," ProQuest Dissertations and Theses Global, 1839275333, University of Utah, Ann Arbor (2016).

229. P. Törmö and W. L. Barnes, "Strong coupling between surface plasmon polaritons and emitters: a review," *Rep. Prog. Phys.* **78**(1), 013901 (2015).

230. N. Gao et al., "Surface-plasmon-enhanced deep-UV light emitting diodes based on AlGaN multi-quantum wells," *Sci. Rep.* **2**(1), 816 (2012).

231. J. Lin et al., "Surface plasmon enhanced UV emission in AlGaN/GaN quantum well," *Appl. Phys. Lett.* **97**(22), 221104 (2010).

232. C.-Y. Cho et al., "Surface plasmon enhanced light emission from AlGaN-based ultraviolet light-emitting diodes grown on Si(111)," *Appl. Phys. Lett.* **102**(21), 211110 (2013).

233. K. C. Shen et al., "Giant enhancement of emission efficiency and light directivity by using hyperbolic metacavity on deep-ultraviolet AlGaN emitter," *Nano Energy* **45**, 353–358 (2018).

234. K. R. Son et al., "Enhanced light emission from AlGaN/GaN multiple quantum wells using the localized surface plasmon effect by aluminum nanoring patterns," *Photonics Res.* **6**(1), 30–36 (2018).

235. K. Huang et al., "Top- and bottom-emission-enhanced electroluminescence of deep-UV light-emitting diodes induced by localised surface plasmons," *Sci. Rep.* **4**(1), 4380 (2014).

236. A. Shetty et al., "Plasmonic enhancement of photocurrent in GaN based UV photodetectors," in *IEEE 2nd Int. Conf. on Emerging Electronics: Materials to Devices (ICEE)* (2014).

Mohd Sharizal Bin Alias is a research scientist at Photonics Laboratory, KAUST. He received his PhD (Microengineering and Nanoelectronics) degree from the National University of Malaysia in 2010, and his MSc (Physics) and BSc (Physics) degrees from the University of Malaya in 2005 and 2000, respectively. His research focuses on the usage of nanophotonics to enhance light manipulation for photonic devices. His other research interests include semiconductor lasers and micro-/nano-fabrication process. He is a senior member of IEEE.

Malleswararao Tangi is a postdoctoral research fellow at Photonics Laboratory, KAUST. He received his PhD in physics from Jawaharlal Nehru Center for advanced scientific research (JNCASR), India and masters in physics from University of Hyderabad, India. His work involves the molecular beam epitaxy growth of III–N materials, 2-D/3-D heterojunctions, and optoelectronic devices.

Jorge A. Holguin-Lerma received his college degree in electromedical engineering from Universidad La Salle Chihuahua, Mexico (2013), and his MS degree in materials science and engineering from King Abdullah University of Science and Technology (KAUST), Saudi Arabia (2016). Currently, he is PhD student in Photonics and Optoelectronics (EE) at KAUST. He is interested in the fields of nanophotonics and optoelectronic devices. He has participated in the industry in the area of device characterization as a components engineer at Honeywell ACS.

Edgars Stegenburgs is a PhD student at Photonics Laboratory, KAUST. He received his MSc degree (electrical engineering) from KAUST in 2016 and his BSc (physics) degree from the University of Latvia in 2014. Previously, he was working in the Laser Centre of the University of Latvia. His research focuses on manipulation of light in photonics and optoelectronics. Other research interests include light-matter interaction, numerical analysis, and solid-state lighting applications. He is a member of IEEE, OSA, and SPIE.

Abdullah A. Alatawi is a PhD student at Photonics Laboratory, KAUST. He is working on different lab projects related to semiconductor devices fabrication and characterization. He received his master of science in optical nanotechnology engineering from Kassel University in Germany. He received his BSc degree in aerospace engineering from King Fahad University of Petroleum and Minerals and then he joined space institute at King Abdullaziz City for Science and Technology. He is a member of IEEE.

Islam Ashry is a postdoctoral research fellow at Photonics Laboratory, KAUST. He received his BS and MS degrees from the University of Alexandria, Egypt, in 2003 and 2007, respectively, and the PhD degree from Virginia Tech, VA, USA, in December 2012. His research interests include optical sensors, fluorescence dynamics, nanopatterning, plasmon sensing, nonlinear optics, fiber optics, optical communications, optical networks, and polymeric thin films. He is a member of IEEE.

Ram Chandra Subedi is a second-year PhD student in Photonics Laboratory at KAUST in CEMSE division. He received his MS (physics) degree from University of Georgia, USA in 2016. Also, he holds MSc (physics) and BSc (physics with Statistics minor) degrees from Tribhuvan University, Nepal in 2011 and 2007, respectively. Deep UV optoelectronic devices based on III-nitride is the main focus of his research.

Davide Priante received his BS degree in material science and engineering from Padua University, Italy, (2013) and his master's degree in electrical engineering from King Abdullah University of Science and Technology (KAUST) (2015). Currently, he is pursuing his PhD in Photonics Lab under the supervision of Prof. Ooi with a research focus on III-nitride wide-bandgap optoelectronic semiconductor devices. He is a member of OSA and SPIE.

Mohammad Khaled Shakfa is currently a postdoctoral research fellow in the Photonics Lab. at KAUST. Before joining KAUST, from 2015 to 2016, he conducted postdoctoral research in the workgroup of Experimental Semiconductor Physics at the Phillips Univ. of Marburg. In 2015, he received his PhD in optoelectronics from the Technical Univ. of Braunschweig. He earned his BS degree in physical sciences (2005) and his postgraduate diploma degree in Solid-State Physics (2006) from Al-Baath Univ. The research activities of Dr. Shakfa have focused on optics and optical spectroscopy.

Tien Khee Ng (senior member of IEEE, member of SPIE, and senior member of OSA) received his PhD (2005) and MEng (2001) degrees in electrical and electronic engineering from Nanyang Technological University, Singapore. Currently, he is a senior research scientist with Ooi-group at KAUST, Saudi Arabia, and the co-principal-investigator responsible for Molecular Beam Epitaxy thrust for the KACST Technology Innovation Center for Solid-State Lighting at KAUST.

Boon S. Ooi is a professor of electrical engineering at KAUST. He received his PhD in electronics and electrical engineering from the University of Glasgow. His research is concerned with the study of semiconductor lasers, LEDs, and photonic-integrated circuits for applications in energy efficient lighting and visible light communications. He is an associate editor of *Optics Express* and *Journal of Nanophotonics*. He is a fellow of OSA, SPIE, and IOP.